

UNIVERSITY OF OKLAHOMA
GRADUATE COLLEGE

REMOVING FOOTPRINT FROM LEGACY SEISMIC DATA VOLUMES

A THESIS
SUBMITTED TO THE GRADUATE FACULTY
in partial fulfillment of the requirements for the
Degree of
MASTER OF SCIENCE

By

OSWALDO ERNESTO DAVOGUSTTO CATALDO
Norman, Oklahoma
2011

REMOVING FOOTPRINT FROM LEGACY DATA VOLUMES

A THESIS APPROVED FOR THE
CONOCOPHILLIPS SCHOOL OF GEOLOGY AND GEOPHYSICS

BY

Dr. Kurt J. Marfurt, Chair

Dr. J. Timothy Kwiatkowski

Dr. Carl Sondergeld

© Copyright by OSWALDO ERNESTO DAVOGUSTTO CATALDO 2011
All Rights Reserved.

Ad maiorem Dei gloriam

To Andrea, Maria T. Giovanni and Oswaldo

ACKNOWLEDGEMENTS

This study would not have been possible without the help of many different people who supported and encouraged me to pursue my goals. First and foremost thanks to God for always showing me the righteous path. I would like to express my deepest gratitude to my mother and father for always teaching me not to take anything for granted and their unconditional and infinite support. I would like to thank my brother for being my best most important friend.

To Dr. Roger Adams Young for teaching me to always look for excellence. To Dr. Kurt J. Marfurt for your patience and dedication. You are by far the most intelligent and polite person I have ever met. I thank you for teaching me geophysics and teaching me for life. Thanks to Dr. Carl Sondergeld, from you I learned also to excel and to understand the importance of knowledge. To Dr. J. Tim Kwiatkowski, you are the cornerstone of my everyday learning and without you this project would have never happened.

I wish to extend my gratitude to Chesapeake, Marathon Oil Company and Schlumberger for providing data and software for this project

And last, to my wife Andrea for your unconditional love and patience.

Thank you very much.

TABLE OF CONTENTS

ACKNOWLEDGEMENTS.....	iv
TABLE OF CONTENTS.....	v
LIST OF FIGURES	vii
LIST OF TABLES.....	xxi
ABSTRACT.....	xxii
CHAPTER I.....	1
Introduction.....	1
Motivation	1
Causes of Acquisition Footprint.....	1
Previous work and summary of solution techniques.....	3
CHAPTER II.....	10
Impact of acquisition footprint on seismic interpretation	10
CHAPTER III	25
Theory	25
Mean Filtering	25
Median Filter	25
α -Trimmed Mean Filter	26
k_x - k_y Filter.....	26
Principal Component Filter	27
CHAPTER IV	33
Evaluation of alternative filtering workflows	33
Filtering along horizon slices	33
Structure Oriented Filtering (SOF).....	35
Edge preservation techniques	36
Sensitivity to smoothing algorithm.....	36
Sensitivity to horizontal window size.....	37
CHAPTER V	60
Alternative workflow examples	60
CONCLUSIONS.....	71
REFERENCES	73

APPENDIX.....	74
APPENDIX 1. REVIEW OF REFLECTOR DIP AND AZIMUTH ESTIMATOR	74

LIST OF FIGURES

- Figure 1: Representative velocity analysis supergather for the Anadarko Basin data set. Red arrows indicate ground roll, converted waves, airwaves and other noise present in the gathers. Purple arrows indicate the residual velocity anomalies in the gather. Spatially (bin-to-bin) varying suppression of these features gives rise to footprint..... 5
- Figure 2: Constant velocity stacks computed for a window about the CMP shown in Figure 1. Red arrows indicate noise that has leaked through the stack array. Accurate velocity picking enhances reflections and filters noise by stacking (green boxes). Note that if an inaccurate velocity is chosen, considerable steeply dipping noise can leak trough the stack (red boxes). 6
- Figure 3: Representative velocity analysis supergather for the Anadarko Basin data set with NMO stretch mute. Red arrows indicate the ground roll, converted wave, airwaves and other noise present in the gathers. Muting the far offsets in the shallow section residual velocity anomalies will not affect the constant velocity stack but has smeared and introduced artifacts in the velocity semblance (white arrows)..... 7
- Figure 4: Constant velocity stacks computed for a window about the CMP shown in Figure 3. Red arrows indicate noise that has leaked through the stack array. Yellow arrows indicate steeply dipping noise introduced by muting and low fold in the gathers. Note the dip reversal between both types of noise. Compared to the constant velocity stacks on Figure 2, reflectors are broader band, such that the reflectors are better resolved in the mid and deep section. Accurate velocity picking enhances reflections and filters noise by stacking (green boxes). Note that if an inaccurate velocity is chosen, considerable steeply dipping noise can leak trough the stack (red boxes). 8
- Figure 5: Migration section of a pre-stack finite difference simulation of the acoustic wave equation. Green arrows indicate where the migration operator of each CDP has constructive interference thus placing the energy of the reflection at the right location in the reflection boundary. Yellow arrows show migration

artifacts that are due to the coarse surface sampling and the subsequent lack of destructive interference for steep dips (after Cabrales-Vargas, 2010). 9

Figure 6: Representative vertical slice through a seismic amplitude volume acquired over the Delaware Basin, NM. Green arrow indicates the interpreted horizon while the magenta dotted line indicates a time slice at 800 ms. The horizon was picked following a zero-crossing. Notice that reflections are contaminated by noise (red arrows). This noise pattern heals with increasing time. Orange and cyan arrows indicate features in the data that might be channels (Seismic data courtesy of Marathon Oil Co.). 12

Figure 7: 3D view of time slice at $t=0.8$ s and line A-A' shown previously in Figure 6. Red arrows indicate acquisition footprint noise. Note that the features indicated by orange arrows in Figure 6 are organized rather than random, mimicking the orthogonal shot line – receiver line acquisition. Cyan arrow indicates a channel like feature that corresponds to the features observed in Figure 8. 13

Figure 8: Time slice at $t=0.8$ s through Sobel filter similarity. Red arrows indicate acquisition footprint noise. Note that the features indicated by orange arrows in Figure 6 are organized rather than random, mimicking the orthogonal shot line – receiver line acquisition. Sobel filter similarity attribute helps to clarify that the feature indicated by the cyan arrow is a channel in Figure 6 and Figure 7. 13

Figure 9: Representative vertical slice through the seismic amplitude volume acquired over the Anadarko Basin, OK. Green arrow indicates interpreted Skinner horizon, yellow arrow indicates interpreted Novi horizon and blue arrow indicates interpreted Red Fork horizon. All horizons were interpreted using wavelet tracking with seeded points using a correlation coefficient of 0.95 in a 12 sample symmetric vertical window. Magenta arrows indicate areas where footprint affects the performance of the wavelet-tracking algorithm. Skinner horizon and Novi horizon exhibit a lateral change in amplitudes due to the footprint but the performance of the wavelet tracking is not

diminished. Red arrows indicate areas where the footprint pattern is particularly strongest. 14

Figure 10: Representative vertical slice through the Watonga seismic amplitude volume acquired over the Anadarko Basin, OK. Green arrow indicates interpreted Skinner horizon, yellow arrow indicates interpreted Novi horizon and blue arrow indicates interpreted Red-Fork horizon. Red Fork horizon was reinterpreted using wavelet tracking with seeded points using a correlation coefficient of 0.85 in a 12 sample symmetric vertical window. Although the Red Fork horizon has been successfully picked, it is quite irregular due to the cross cutting noise (orange arrows). Red arrows indicate areas where the footprint pattern is strongest. 15

Figure 11: Workflow for generating a smooth time-structure map honoring fault traces. Most interpretation packages follow a similar flow to generate time-structure maps. 15

Figure 12: 3D view of time-structure map interpreted from a seismic amplitude volume acquired offshore Louisiana. Cyan arrows indicate distinctive faults that are preserved after the interpolation smoothing. Red arrows indicate noise in vertical sections (data courtesy of Schlumberger). 16

Figure 13: 3D view of the dip magnitude derived from the time-structure map shown in Figure 12. Red arrows indicate N-S artifacts in the dip magnitude map caused by the acquisition footprint. 17

Figure 14: 3D view of dip azimuth derived from the time-structure map in shown Figure 12. Red arrows indicate zones where the footprint signature is strongest. The magenta-red color anomalies indicate dip azimuths of 90° corresponding to the N-S footprint. 18

Figure 15: 3D view of seismic amplitude extracted along the time-structure map shown in Figure 12. Red arrows indicate zones where the footprint signature is strongest. 19

Figure 16: Time slice at $t=0.8$ s through the (a) dip magnitude and (b) dip azimuth data volumes computed from the data shown in Figure 6. Dip magnitude and azimuth were calculated using a semblance-based search within a three trace

by three trace by 0.020 s analysis window. Red arrows indicate the acquisition footprint artifacts on the volumetric dip magnitude; green arrows indicate the platform edge. The footprint sometimes appears as circles (white arrows) and sometimes as a grid of NE, NW-trending (black arrows) and N-S trending (gray arrows) lineaments..... 20

Figure 17: Time slice at $t=0.8$ s through the dip magnitude volume computed from the data shown in Figure 6. Dip was calculated using a three trace by three trace by 0.020 s analysis window with (a) nine overlapping Kuwahara windows at the analysis point and (b) a single analysis window centered about the analysis point. Yellow and cyan arrows indicate lineaments exacerbated by using nine overlapping windows method in the dip magnitude calculation. Green arrows indicate lineaments that are smoothed by using a nine overlapping windows in the dip magnitude calculation. Red arrows indicate footprint noise that remains unchanged using either method..... 21

Figure 18: Time slice at $t=1.3$ s through the (a) most positive principal structural curvature and (b) most negative principal structural curvature data volumes computed from the data shown in Figure 12. (a) Green arrows indicate features that correlate to folds and faults seen on vertical slices through the seismic amplitude volume that are enhanced by the curvature attribute. Cyan and yellow arrows indicate lineaments attributed to the acquisition footprint. Most negative structural curvature seems to be more sensitive to the acquisition footprint than the most positive structural curvature for this particular data set..... 22

Figure 19: Phantom horizon slice 0.066 s below Skinner horizon trough (a) peak frequency modulated by peak magnitude and (b) peak wavelet phase modulated by peak magnitude using a 2D color map (Guo et al., 2008) data volumes computed from seismic amplitude volume acquired over the Anadarko Basin, OK (Figure 9). (a) Red arrows indicate acquisition footprint artifacts with a predominant frequency of 30 Hz. (b) White arrows indicate acquisition footprint artifacts seen on phase. 23

- Figure 20: Time slice at $t=1.68$ s through the model based acoustic impedance data volume computed from the data shown in Figure 9. White arrows indicate acquisition footprint artifacts. Artifacts appear as N-S trending impedance anomalies that mask impedance in the reservoir interval. 24
- Figure 21: Example of a 13-sample analysis window centered about an analysis point at (). This analysis window is applied to every sample in the 3D volume, typically aligned along the local reflector dip. The numbering is arbitrary (in this example clockwise, reading from the center). 29
- Figure 22: Effect of the mean, median, and α -trimmed mean filter on a test dataset. (a) Original data and its histogram. (b) Random noise with uniform distribution (c) Original data with added noise. (d) Mean filtered data; histogram has the same character as the original data but edges and subtle details are not preserved. (e) Median filtered data; edges are better preserved but still some subtle details are removed. (f) 20 % α -trimmed mean filtered data; edges as well as subtle detail are well preserved by this filter being a hybrid between the mean and the median filter. 30
- Figure 23: The first 11 of 441 eigenmaps computed from a covariance matrix generated by cross-correlating a suite of eleven 21 by 21 trace horizon slices extracted along horizon 1 shown in Figure 12. By construction, the first eigenmap (a) best represents the data variability in the eleven-sample window; the second eigenmap (b) best represents the remainder and so on. This result indicates that the coherent part of the signal will be well represented by the first four eigenmaps and the noise, either random or not, will remain on the later eigenmaps. 31
- Figure 24: (a) Principal component eigenvalues corresponding to the eigenmaps shown in Figure 23 note that 19.95% of the energy is represented by the first four eigenmaps. and (b) vertical waveform centered along the horizon slice (sample $k=0$) resulting by cross-correlating the first eleven eigenmaps with eleven 21 by 21 trace phantom horizon slices centered about the picked horizon at sample 0. When cross-correlated with the data the first waveform

	represents the seismic traces better than the other waveform in the 21x21 trace analysis window.	31
Figure 25:	21x21 inline by crossline patch of seismic amplitude extracted along horizon 1 shown in Figure 9 and its reconstruction to from the first eleven principal components. As shown in Figure 23 and Figure 24 the signal is well represented by the first four eigenmaps. The first principal component reconstruction best approximates the original data and even enhancing certain features in it.	32
Figure 26:	k_x - k_y filtering workflow for seismic amplitude data using seismic attribute pattern recognition described by Falconer and Marfurt, 2006.	38
Figure 27:	Application of footprint suppression workflow shown in Figure 26 to the seismic amplitude volume acquired over the Anadarko Basin, OK. (a) Time slice through seismic amplitude at $t=1.6$ s horizon shown in Figure 9. Red arrows indicate footprint anomalies on the data. (b) Corresponding time slice through most negative amplitude short wavelength curvature exacerbating short wavelength footprint anomalies and its derivative spectrum. (c) Time slice through smoothed most negative amplitude curvature at $t=1.6$ s after median filter to suppress any remaining signal of the geologic features and enhance vertical footprint features. (d) Time slice through most negative amplitude curvature at $t=1.6$ s in the k_x - k_y domain. White arrows indicate peak amplitude anomalies due to the footprint signal in the attribute. Black arrows indicate N-S and E-W anomalies that correlated to the survey edges as well as footprint. (e) Time slice through seismic amplitude at $t=1.6$ s in the k_x - k_y domain. Most of the smooth, relatively flat signal will cluster near the origin (yellow arrows) whereas lineaments such faults and channels will be scattered at larger values of k_x - k_y . White arrows indicate zones where noise clusters are present. Black arrows indicate anomalies due to the survey edges. (f) Notch filter pedestals. Counter intuitively in this step the signal is removed from the data in order to model the noise components. Noise (blue arrows) will then be adaptively subtracted from the data for a noise reduced seismic amplitude volume.	39

Figure 28: (a) Time slices at $t=1.6$ s through: original seismic amplitude data, k_x-k_y filtered seismic amplitude data and noise pattern for the dataset acquired in the Anadarko Basin, OK. Notice that most of the N-S and E-W lineaments present due to the footprint in the original data have been removed. Green arrows indicate geologic features that have been enhanced after the filtering. Yellow arrows indicate footprint pattern characterized by the k_x-k_y filter and removed from data. (b) Representative vertical section through the original seismic amplitude data, filtered seismic amplitude data and noise pattern for the dataset acquired in the Anadarko Basin, OK. Green arrows indicate areas where the signal-to-noise ratio has increased compared to the original data. Red arrows indicate areas where noise was removed but it is still present. Yellow arrow indicates geologic features removed by the filtering process represented by a k_x-k_y “noise” component. 40

Figure 29: Time slice at $t=1.6$ s through (a) original seismic amplitude data, (b) k_x-k_y filtered seismic amplitude data and (c) removed noise for the dataset acquired in the Anadarko Basin, OK. Distinctive geologic features can be observed in both the original and filtered data. Filtered data displays sharper and better defined channels and features than the original data. Unfortunately part of the signal present in the data was also removed, dimming certain features indicated by red arrows. Green arrows indicate footprint removed. Note the difference in amplitude scales. 41

Figure 30: Representative section through frequency spectrum calculated for (a) k_x-k_y filtered seismic amplitude data and (b) noise pattern for the dataset acquired in the Anadarko Basin, OK. Most of the signal in the filtered data is in the 20 to 70 Hz band. Magnitude through the vertical section shows a regular character. The noise spectrum appears to be contained in the 60 to 80 Hz with “bursts” in the lower frequencies. 42

Figure 31: A window of five noise-contaminated traces having the same underlying waveform, but with different amplitudes (1, 1, 1, 2, 2). The first eigenvector or principal component, are amplitudes that best represent this lateral variation within the vertical analysis window. By convention, the eigenvector

is normalized here by $\frac{1}{\|v\|}$ to have length 1.0, giving rise to the eigenvector $v^j = \dots$ 43

Figure 32: Phantom horizon slice 0.066 s below the Skinner horizon (Figure 9) through (a) original seismic amplitude data, (b) horizon based principal component filtered seismic amplitude data and (c) removed noise for the dataset acquired in the Anadarko Basin, OK. The filter was designed using the first three principal components of the data in a 21-trace by 21-trace running analysis window. Footprint is attenuated in the filtered data (green arrows) but still present. The lack of footprint removal from the principal component filter is due to the consistent character of its waveform through the data. Note on the noise slice that random patterns of footprint are removed but also an equal amount of signal (red arrows). 44

Figure 33: Fehmers and Höecker's (2003) structure-oriented filtering workflow where the degree of smoothing is a function of the strength of the measured discontinuities. Their original algorithm computed d_i , azimuth, and discontinuities using a gradient structure tensor (GST). In the actual implementation there is a gradational blending between "smooth" and "don't smooth". 45

Figure 34: Suite of images illustrating the interactive workflow used to define smoothing weights in structure-oriented filtering for a time slice at $t=0.76$ s through the Sobel filter similarity data volume computed from the offshore Louisiana data set (Figure 12). (a) Similarity values, S , and corresponding weights, W . By modifying the threshold values for S we increase or decrease the smoothing weights thereby changing the aggressiveness of the filter. (b) Note the enhancement of the footprint noise (red arrows). Green arrows indicate white areas where the filter will be more aggressive and remove incoherent noise. (c) Yellow arrows indicate geologic features that will be partially or totally smoothed due to their similarity values S and corresponding weights W compared to (a). Green arrows indicate features that will be preserved or areas where footprint will be removed. (d) This case is the optimal setting for the degree of smoothing. Green arrows indicate key areas where (d) shows an

	improvement over (c) both in preserving lineaments and removing footprint.	46
Figure 35:	Time slice at $t=0.76$ s though (a) seismic amplitude and (b) output from a variation of Fehmers and Höecker’s structure-oriented principal component algorithm for the offshore Louisiana data set. (a) Red arrows indicate footprint contamination. (b) The amplitude of the footprint was diminished by the filter but there are still remnants visible after first iteration (yellow arrows). Green arrows indicate areas where edges of geologic features are sharper.	47
Figure 36:	(a) An analysis window centered about an analysis point indicated by the red solid dot containing a total of 13 traces (red and green dots). (b) A suite of 13 overlapping windows centered about the green dots in (a), each of which also contains 13 traces, including the analysis point indicates by the red dot. The coherence along dip and azimuth is computed in each window and used in the flow described in Figure 36. Use of such laterally shifted windows helps avoid smoothing across faults, angular unconformities and other features of geologic interest when compared to (a).	48
Figure 37:	Structure oriented filtering workflow using a modification of the Kuwahara algorithm for dip estimates after Marfurt (2006).	49
Figure 38:	Time slice at $t=0.76$ s though (a) seismic amplitude and (b) principal component filtered seismic amplitude following the workflow in Figure 36 for the offshore Louisiana data set. (a) Red arrows indicate footprint contamination. The amplitude of the footprint was diminished and smeared by the filter but there are still remnants visible in (b) (yellow arrows). Green arrows indicate areas where edges of geologic features are sharper. Cyan arrows indicate features that became distinguishable after the filtering. Line AA’ is shown in Figure 38.	50
Figure 39:	Vertical section through line AA’ shown in Figure 37 for the offshore Louisiana dataset showing (a) original data, (b) filtered data and (c) noise respectively. The data was filtered using modified Fehmers and Höecker’s workflow (Figure 32) using a single analysis window containing 13 traces.	

Fehmers and Höecker’s technique shows effective for removing footprint modulation through the entire section (green arrows) but removes also a fair amount of signal (yellow arrows)..... 51

Figure 40: Vertical section through line AA’ shown in Figure 37 for the offshore Louisiana dataset showing (a) original data, (b) filtered data and (c) noise respectively. The data was filtered using modified Kuwahara window workflow (Figure 36) using a suite of 13 overlapping windows each of which contains 13 traces. The Kuwahara technique also does a good job in removing the footprint modulation through the entire section (green arrows) and also removes fault plane reflections (magenta arrows). An improvement in the reflector coherence due to Kuwahara’s overlapping window technique is observed. Examples in Figure 38 and Figure 39 used only one iteration and the same edge-preservation criteria and weights (Figure 33c)..... 52

Figure 41: (a) Five noise contaminated traces. Note traces 1 and 2 have a peak amplitude of about 2.0 while traces 3-5 have a peak amplitude of about 1.0. (b) Detail of center trace 3 showing the results of mean, median, and principal component filtering. The mean and median filters both overestimate the amplitude, while the PC-filter both diminishes random noise and approximates the underlying true signal amplitude. The PC filter does this by using 55 data values (5 traces by 11 time samples) in the filter design, while the mean and median filters are based only 5 data values (5 traces at a single time sample). 53

Figure 42: (a) Time slice at $t=0.76$ s though mean-filtered seismic amplitude using the workflow shown in Figure 36. (b) Difference between original data (Figure 34a) and (a). (c) Vertical section through mean filtered seismic amplitude for line A-A’ shown in (a). Red arrows indicate footprint contamination, yellow arrows indicate features that have enhancement after filtering but are still damaged by the footprint. Green arrows indicate features that have been improved after filtering. (b) Most of the removed amplitudes correspond to footprint modulation. Note that some signal has been removed also by the filtering process. (c) Green arrows indicate areas where filtering has

improved reflector continuity. Yellow arrows indicate areas that are still damaged by the footprint..... 54

Figure 43: (a) Time slice at $t=0.76$ s though median-filtered seismic amplitude using workflow shown in Figure 36. (b) Difference between original data (Figure 34a) and (a). (c) Vertical section through median-filtered seismic amplitude for line A-A' shown in (a). (a) Red arrows indicate footprint contamination, yellow arrows indicate features that have enhancement after filtering but still damaged by the footprint. (b) Most of the removed amplitudes correspond to footprint modulation. Note that more signal has been removed when compared to Figure 41b. (c) Median filter is not as effective as the mean filter in removing the footprint. Red arrows indicate areas where a strong footprint contamination is observed. 55

Figure 44: (a) Time slice at $t=0.76$ s though 20% α -trimmed mean filtered seismic amplitude using workflow shown in Figure 36. (b) Difference between original data (Figure 34a) and (a). (c) Vertical section through α -trimmed mean filtered seismic amplitude for line A-A' shown in (a). For this particular case the results of the α -trimmed mean filtered data are very similar to the median filter. 56

Figure 45: (a) Time slice at $t=0.76$ s though principal component filtered seismic amplitude using workflow shown in Figure 36. (b) Difference between original data (Figure 34a) and (a). (c) Vertical section through principal component filtered seismic amplitude for line A-A' shown in (a). (a) Yellow arrows indicate areas that where the footprint has not been removed completely. Green arrows indicate features that have been enhanced by filtering. (b) Compared to Figure 41 and Figure 42 principal component filtered better removes footprint modulation. Note that almost no signal was removed from the original data. (c) Green arrows indicate areas where reflector continuity has been greatly enhanced by filtering. Yellow arrows indicate areas where footprint still present. 57

Figure 46: Time slice at $t=0.76$ s though (a) principal component filtered seismic amplitude (Figure 36) using the first eigenmap, (b) principal component

filtered seismic amplitude (Figure 36) using the second eigenmap and (c) difference between (a) and (b). Lineaments edges are sharper and better defined in (b) with respect to (a). (c) Red arrows indicate subtle features and edges present in (b) that are removed in (a) by the filtering process. 58

Figure 47: Time slice at $t=0.76$ s though (a) principal component filtered seismic amplitude (Figure 36) using a horizontal analysis window radius of 25 m containing 5 traces, (b) principal component filtered seismic amplitude (Figure 36) using a horizontal analysis window radius of 50 m containing 13 traces and (c) difference between (a) and (b). (c) For this case principal component filtering with a larger horizontal window shows more effective in removing footprint noise (magenta arrows). Notice that large discontinuity features are not harmed by a larger window (green arrows) although small geologic features could be harmed when using a larger horizontal analysis window (yellow arrow) 59

Figure 48: Workflow implemented for removing footprint contamination of structural curvature attributes 61

Figure 49: Time slice at $t=0.8$ s through the (a) original seismic amplitude data, (b) k_x-k_y filtered seismic amplitude data, (c) difference between (a) and (b), (d) principal component filtered data from (b) and (e) difference between (b) and (d) for the dataset acquired in the Delaware Basin, NM using the workflow shown in Figure 48. (a) Magenta arrows indicate areas where the footprint contamination is strongest. (b) k_x-k_y filter was implemented using most positive structural curvature following the workflow in Figure 26. Green arrows indicate areas where the footprint was successfully removed after k_x-k_y filtering. (c) Some steeply dipping reflectors were attenuated by k_x-k_y filtering (yellow arrows). (d) Principal component filter was implemented using a 220 ft horizontal window containing 13 traces, a 0.01 s vertical window containing 5 samples and the first three principal components following the workflow in Figure 37. Green arrows indicate areas of improvement compared to the k_x-k_y filtered data. (d) Yellow arrows indicate

	subtle geologic features removed by the principal component filtering process.....	62
Figure 50:	Time slice at $t=0.8$ s through the (a) most positive structural principal curvature calculated from original seismic data, (b) most positive structural principal curvature calculated from k_x-k_y filtered seismic amplitude data, (c) and most positive structural principal curvature calculated from principal component filtered for the dataset acquired in the Delaware Basin. (a) Yellow arrows indicate areas where the footprint contamination is strongest. (b) Green arrows indicate areas where curvature attribute has improved after k_x-k_y filtering. (c) Green arrows indicate areas where the combination of k_x-k_y filtering and principal component structure-oriented filtering has improved subtle geologic features.....	63
Figure 51:	Workflow implemented for removing footprint contamination of frequency, phase and impedance inversion. Note there are two iterations of SOF following k_x-k_y filtering.....	64
Figure 52:	Phantom horizon slice 0.066 s below the Skinner horizon through (a) peak frequency modulated by peak magnitude using a 2D color map (Guou et al, 2008) computed from seismic amplitude volume acquired over the Anadarko Basin, OK. (b) Peak frequency modulated by peak amplitude using a 2D color map (Guo et al, 2008) computed from filtered seismic amplitude volume following workflow in Figure 51. Red arrows indicate acquisition footprint artifacts with a predominant frequency of 30 Hz. White arrows indicate enhanced features after the filtering process. Blue arrows indicate features that have become visible after filtering. Red arrows indicate areas still affected by acquisition footprint.....	65
Figure 53:	Phantom horizon slice 0.066 s below Skinner horizon trough (a) peak phase modulated by peak magnitude using a 2D color map (Guo et al, 2008) computed from seismic amplitude volume acquired over the Anadarko Basin, OK. (b) Peak frequency modulated by peak amplitude using a 2D color map (Guo et al, 2008) computed from filtered seismic amplitude volume following workflow in Figure 51. (a) White arrows indicate acquisition	

footprint artifacts. Black arrows indicate enhanced features after the filtering process. Grey arrows indicate features that have become visible after filtering. 66

Figure 54: Time slice at $t=1.68$ s trough (a) relative acoustic impedance computed from seismic amplitude volume acquired over the Anadarko Basin, OK and (b) relative acoustic impedance data volume computed from filtered seismic amplitude volume using workflow in Figure 51. (a) White arrows indicate acquisition footprint artifacts. Artifacts appear as N-S trending impedance anomalies that mask impedance in the reservoir interval. (b) Grey arrows indicate areas where filtering has improved the resolution of the relative acoustic impedance. White arrows indicate areas still affected by footprint. 67

Figure 55: Workflow implemented for removing footprint contamination of similarity attributes. Note the k_x-k_y following the SOF filtering and the two iterations of SOF following k_x-k_y filtering. 68

Figure 56: Time slice at $t=0.6$ s trough (a) original seismic amplitude and (b) filtered seismic amplitude following workflow shown in Figure 55 for seismic data acquired over Central Basin Platform, TX. Red arrows indicate footprint contamination. Green arrows indicate zones where filtering has enhanced the amplitude of geologic features. Yellow arrows indicate features that have been harmed as a consequence of filtering. 69

Figure 57: Time slice at $t=0.6$ s trough Sobel filter similarity computed from (a) original seismic amplitude and (b) filtered seismic amplitude following workflow shown in Figure 55 for seismic data acquired over Central Basin Platform, TX. (a) Red arrows indicate footprint contamination. (b) Green arrows indicate zones where filtering has enhanced the amplitude of geologic features. Red arrows indicate features that have been harmed as a consequence of filtering. Circled areas are subject to karsting at the San Andres level. 70

LIST OF TABLES

Table 1: Summary matrix of observed acquisition footprint examples and solution techniques.	72
--	----

ABSTRACT

Acquisition footprint often poses a major problem in 3D seismic data. Some of the causes for footprint are constraints on survey design, backscattered noise, lateral variations of fold, offset, and azimuth distributions, and spatial aliasing. Faced with extracting subtle features contained in seismic amplitudes, interpreters are often confronted with footprint that can mask important details critical to the identification of key reservoir architectural elements.

Ideally, footprint from acquisition is handled in the processing shop through more careful attention to trace balancing statics, noise reduction and velocity analysis. Such reprocessing is not feasible on many legacy data volumes where the pre-stack data cannot be found or no longer exists.

Seismic attributes provide an effective means of delineating subtle geological features of interest such as channels, small faults, and fractures. Footprint can mask geologic lineaments such as faults and fractures that would otherwise be enhanced by attributes like coherence or curvature. For this reason attributes can be used to both design and evaluate the effectiveness of alternative footprint suppression workflows.

In this work I review, apply and evaluate the three most popular footprint suppression workflows: structure-oriented filtering, k_x - k_y filtering, and limited data reconstruction using singular value decomposition.

Application to legacy land and shallow-water data shows that no one workflow works best. However, evaluation of attribute images computed from filtered volumes provides a quantitative means of determining which workflow, or cascaded workflow, works best for a specific data volume.

CHAPTER I

Introduction

Motivation

Acquisition footprint often poses a major problem in 3D seismic data. Some of the causes for footprint are constraints on survey design, backscattered noise, lateral variations of fold, offset, and azimuth distributions, and spatial aliasing. Faced with extracting subtle features contained in seismic amplitudes, interpreters are often confronted with footprint that can mask important details critical to the identification of key reservoir architectural elements.

Seismic attributes provide an effective means of delineating subtle geological features of interest such as channels, small faults, and fractures. Footprint can mask geologic lineaments such as faults and fractures that would otherwise be enhanced by attributes like coherence or curvature.

In this work I will review, apply and evaluate a suite of different filtering techniques to attenuate acquisition footprint on post-stack seismic data. I will quantify the effectiveness of these filters through attribute images.

Causes of Acquisition Footprint

Footprint cannot be attributed to a single cause, but rather to a combination of data acquisition and processing decisions. The acquisition design defines a particular distribution of bins and bin properties such as fold, azimuths, and offsets. While one would wish that these properties are constant for all the bins in a survey, this is never the case.

One of the major contributors of footprint in land data is aliased backscattered noise. Such noise can be associated with ground-roll and aliased shallow diffractors (Pramik personal communication, 2010). Bin to bin variation in the distributions of offsets and azimuths allow the backscattered noise to leak through the stack array, giving rise to a noise pattern that mimics the acquisition program (Figure 1-4). Azimuthal dependence occurs because source arrays, receiver groups and the stack array itself preferentially accept or reject the backscattered noise depending on azimuth (Chopra and Marfurt, 2008).

Since the signal-to-noise ratio is a function of fold, obstacles cause deviations from the desired, regular geometry giving rise to spatially variable footprint.

In addition to noise, coarse spatial sampling gives rise to spatial aliasing of signal. The signal is most commonly aliased by the migration operator's attempt to image steep dips. These steeply dipping swings are seen on almost all data volumes (Figure 5).

Hill et al. (1999) provide a thorough explanation of how footprint can arise in the processing shop. They start by defining the footprint as a weighted, linear summation of partial-offset fold of stacks. They then show that footprint is caused by a variety of offset dependent phenomena including source generated noise, residual NMO, amplitude versus offset (AVO) anomalies and preferential suppression of multiples and converted waves at different offsets. Random noise and stacking process may introduce a footprint that is driven by lateral offset variations between bins and amplitude correction pattern that will be superimposed on the data (Hill et al., 1999). For flat-layered geologies, the footprint pattern will be time-dependent because of time dependent stretch mutes and decreasing angles of illumination with depth (Hill et al., 1999). Footprint will vary with time if the

offset dependent cause of the footprint does not share the same dip as the primary reflectors. While footprint may have a very regular pattern on shallow time slices, this pattern will be distorted due to lateral velocity variations in the overburden and to an inaccurate migration velocity model (Hill et al., 1999).

Previous work and summary of solution techniques

Several techniques have been implemented to suppress acquisition footprint on post-stack seismic data. Fehmers and Hockers (2003) introduced a structure oriented filter that smoothes parallel to the seismic reflections, but preserves reflection terminations identified as low coherence anomalies. Luo et al. (2002) extended Kuwahara et al. (1976) algorithm to 3D seismic data as an alternative edge preserving smoothing algorithm (EPS). The method consists in computing the mean and standard deviation of amplitude that fall within the analysis point. The mean of the most homogeneous window, i.e. the window having the lowest standard deviation, replaces the amplitude at the analysis point. Marfurt (2006) describes a modification of Luo et al.'s (2002) technique; first he uses coherence rather than standard deviation to choose the most homogeneous window. Then instead of calculating the mean, the median or the α -trimmed mean and replacing the amplitude of the analysis point with one these values, he calculates the principal components of the analysis window, and uses the projected value of the first eigenvector on the windowed data as the filtered data.

Al-Bannagi et al. (2005), use principal component analysis of relatively large analysis windows applied in a 2D by 2D fashion to characterize the pattern of the footprint. Each N trace by T sample data matrix is decomposed into its principal components. Those

components interpreted to represent the noise are then excluded from the reconstruction of the wavefield.

Drummond et al. (2000) compute the k_x - k_y spectra of the seismic data on time slices to identify the aliased noise. These noise components are then attenuated by designing notch filters at the corresponding wavenumbers. For the aliased noise Drummond et al. (2000) suggest adaptive filtering time slice by time slice using image processing techniques in the k_x - k_y domain. Gülünay (1999) presents an extension to the f - k_x - k_y filtering algorithm for dipping data. The method assumes that footprint occurs as a discrete limited numbers of f - k_x - k_y components which are then muted. Soubaras (2002) also uses a k_x - k_y filter to remove spatially periodic noise present in the data designed by autocorrelating the offset distribution vector of the traces. If the vector offset distribution is periodic, its autocorrelation will also be periodic giving rise to localized anomalies in the k_x - k_y domain. Such k_x - k_y filters are commonly applied as part of the processing flow, where notches can be predicted from the prestack acquisition geometry.

Unfortunately, such acquisition patterns are missing for many legacy data volumes. Falconer and Marfurt (2006) compensate for this missing information on migrated data by characterizing the footprint pattern using attributes sensitive to footprint. The footprint-suppression filters are designed in the k_x - k_y domain on attribute time slices. Noise is estimated by applying these filters to the seismic amplitude time slice by time slice. The noise estimate is then adaptively subtracted from the original data.

In this tutorial paper, I evaluate alternative algorithms and workflows to suppress acquisition footprint on migrated, stacked data volumes. I begin by illustrating the impact of footprint on seismic amplitude, attribute and impedance volumes. Next, I review the

theory of each of the methods used to attenuate acquisition footprint. Then I present data-dependent workflows using these algorithms and evaluate their success by reexamining amplitude, attribute and impedance slices. I conclude by summarizing the limitations and advantages of the competing methods.

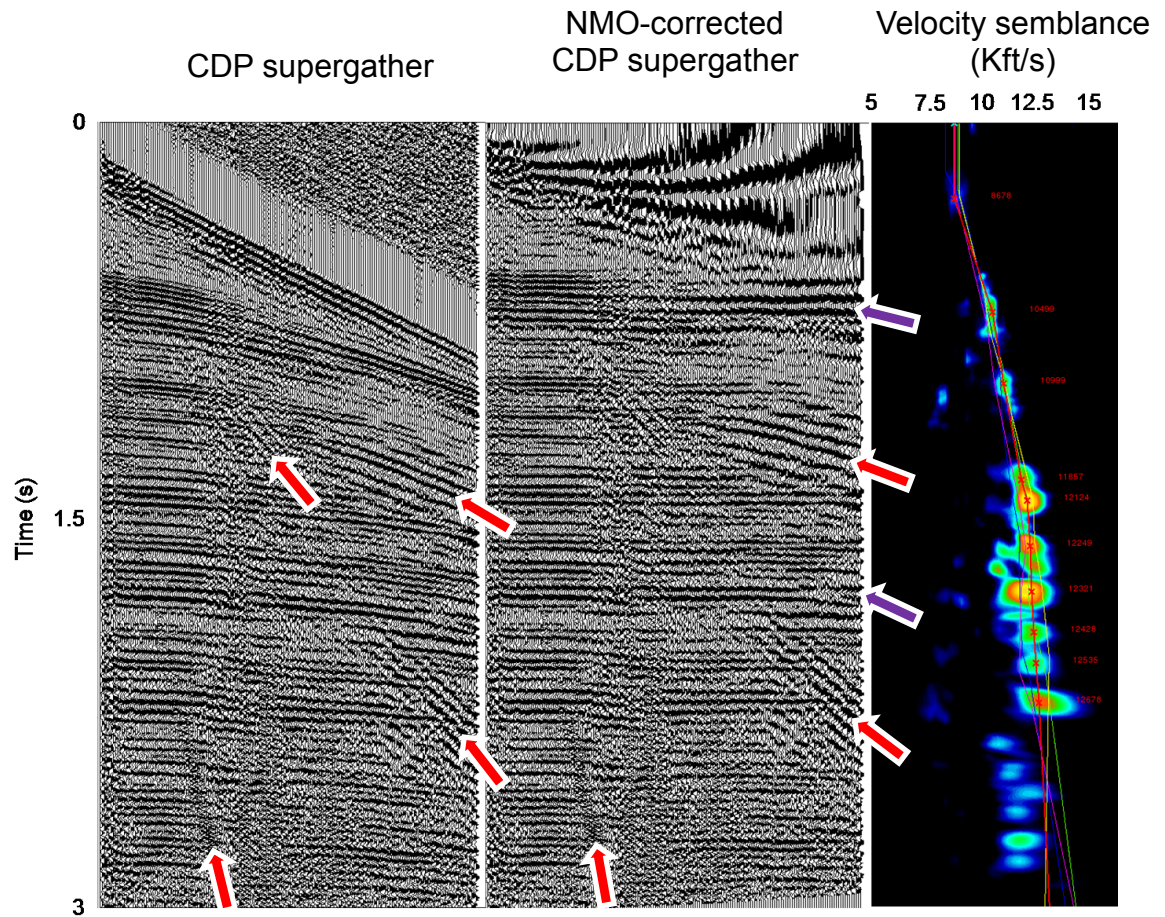


Figure 1: Representative velocity analysis supergather for the Anadarko Basin data set. Red arrows indicate ground roll, converted waves, airwaves and other noise present in the gathers. Purple arrows indicate the residual velocity anomalies in the gather. Spatially (bin-to-bin) varying suppression of these features gives rise to footprint.

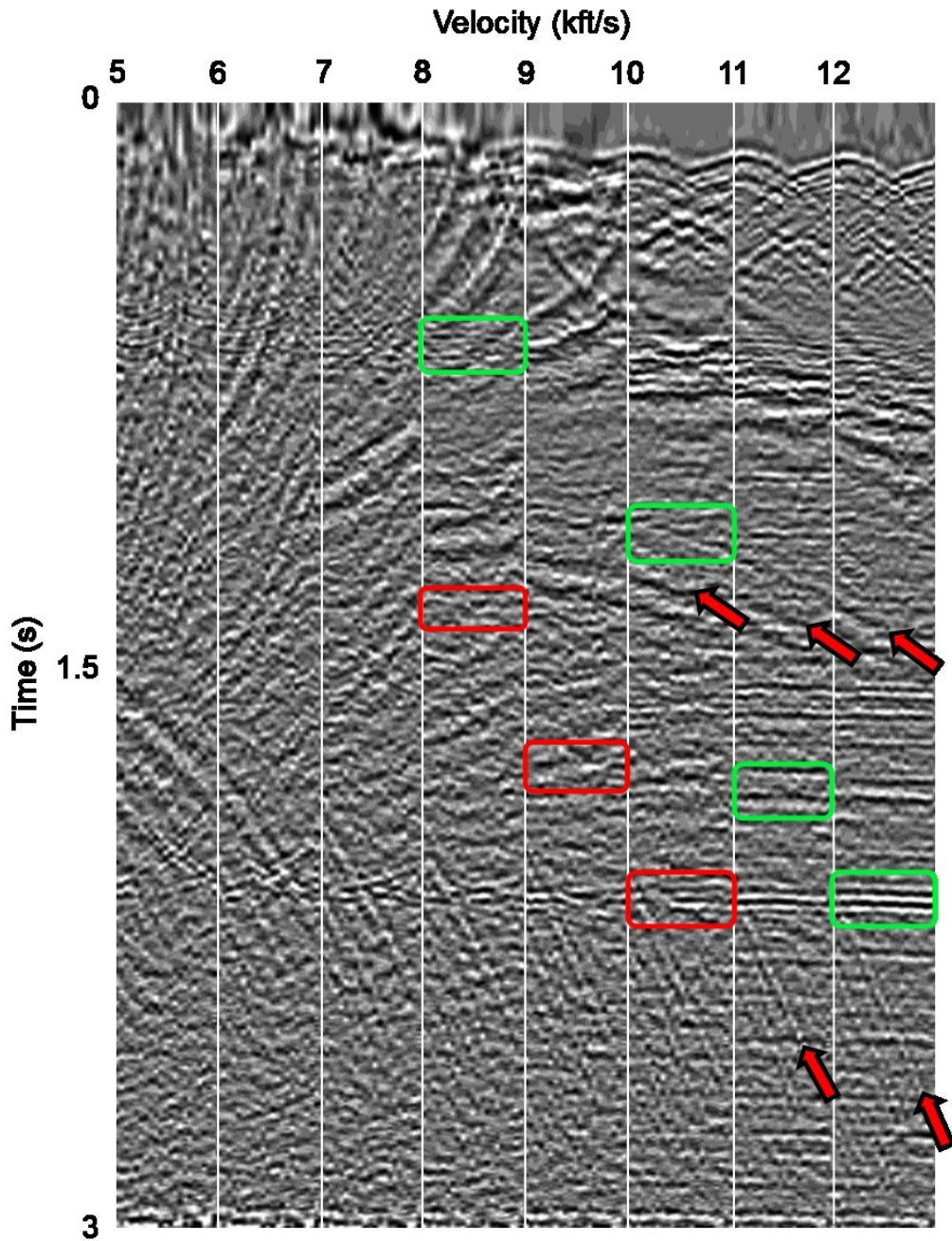


Figure 2: Constant velocity stacks computed for a window about the CMP shown in Figure 1. Red arrows indicate noise that has leaked through the stack array. Accurate velocity picking enhances reflections and filters noise by stacking (green boxes). Note that if an inaccurate velocity is chosen, considerable steeply dipping noise can leak trough the stack (red boxes).

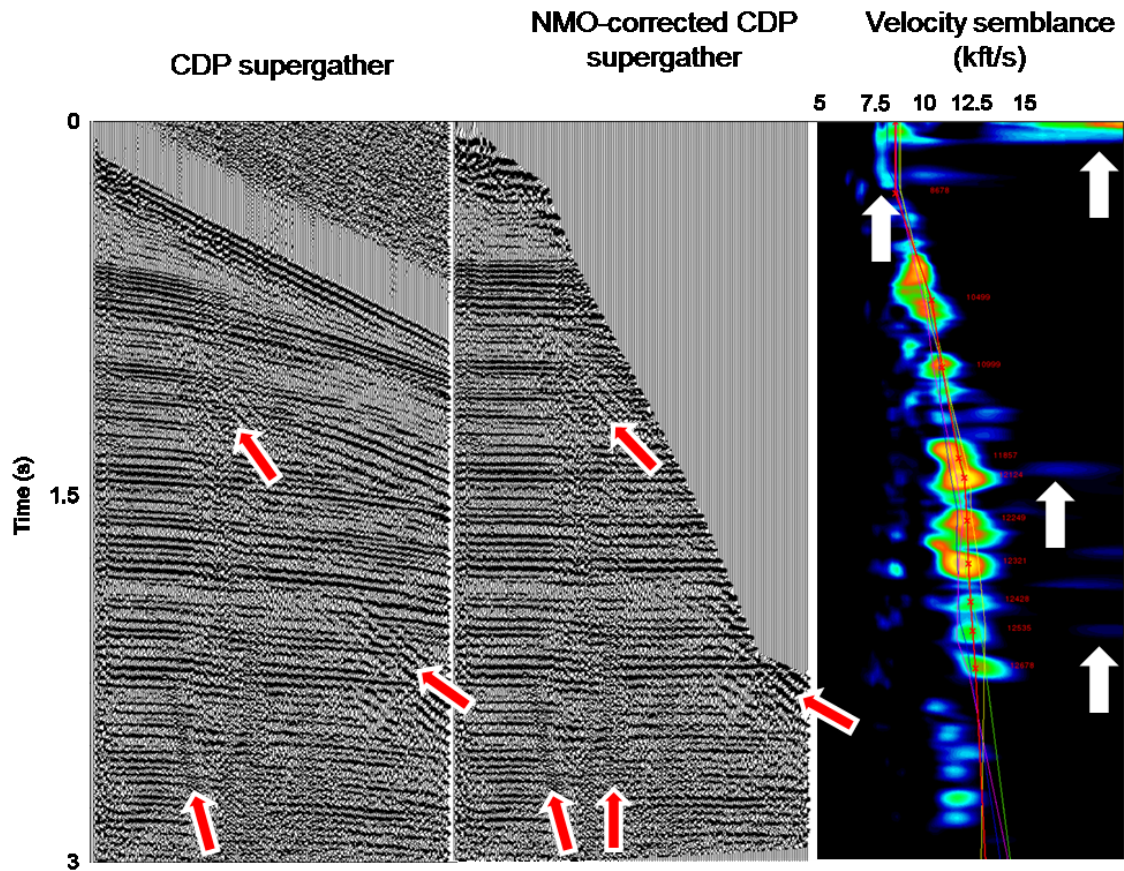


Figure 3: Representative velocity analysis supergather for the Anadarko Basin data set with NMO stretch mute. Red arrows indicate the ground roll, converted wave, airwaves and other noise present in the gathers. Muting the far offsets in the shallow section residual velocity anomalies will not affect the constant velocity stack but has smeared and introduced artifacts in the velocity semblance (white arrows).

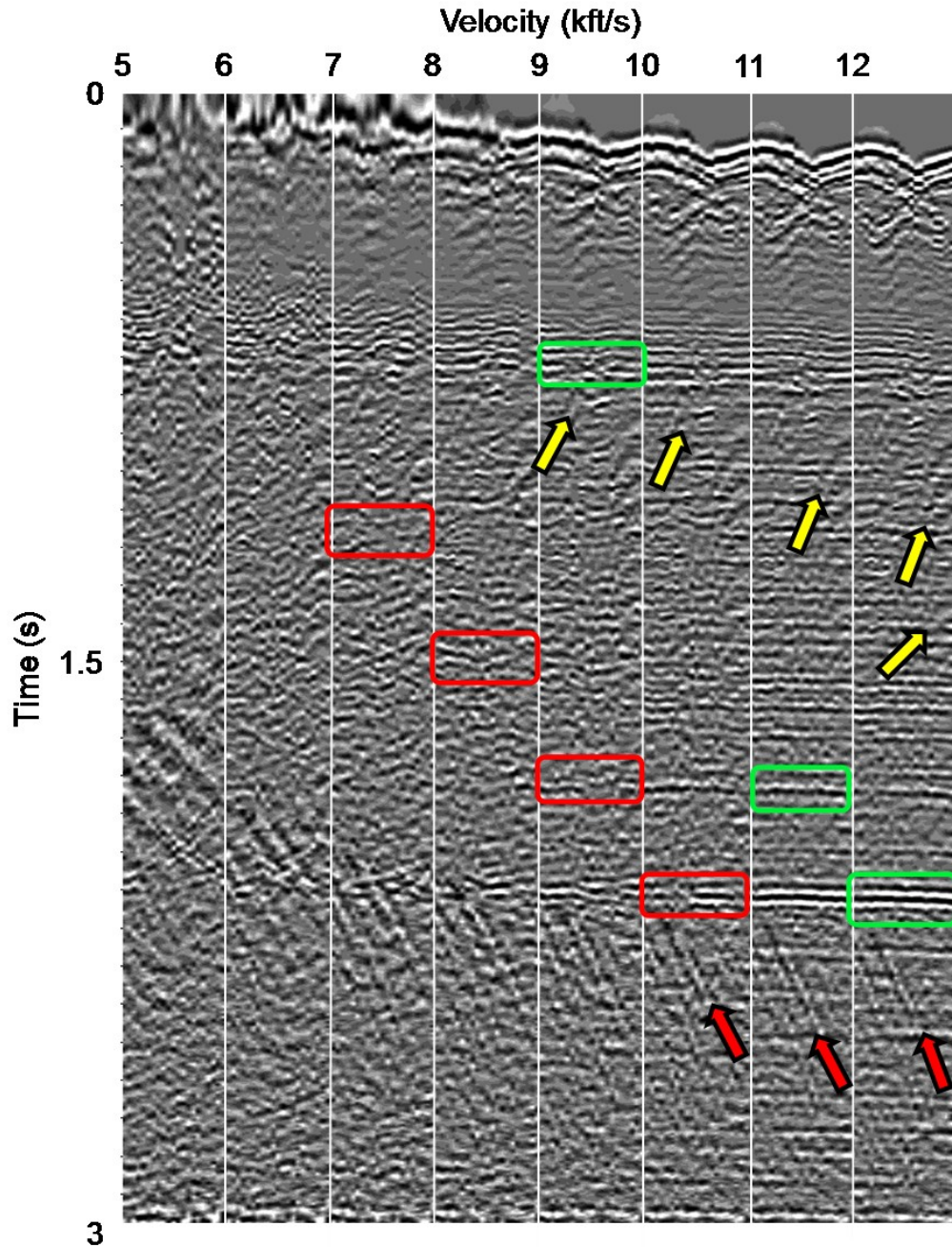


Figure 4: Constant velocity stacks computed for a window about the CMP shown in Figure 3. Red arrows indicate noise that has leaked through the stack array. Yellow arrows indicate steeply dipping noise introduced by muting and low fold in the gathers. Note the dip reversal between both types of noise. Compared to the constant velocity stacks on Figure 2, reflectors are broader band, such that the reflectors are better resolved in the mid and deep section. Accurate velocity picking enhances reflections and filters noise by stacking (green boxes). Note that if an inaccurate velocity is chosen, considerable steeply dipping noise can leak through the stack (red boxes).

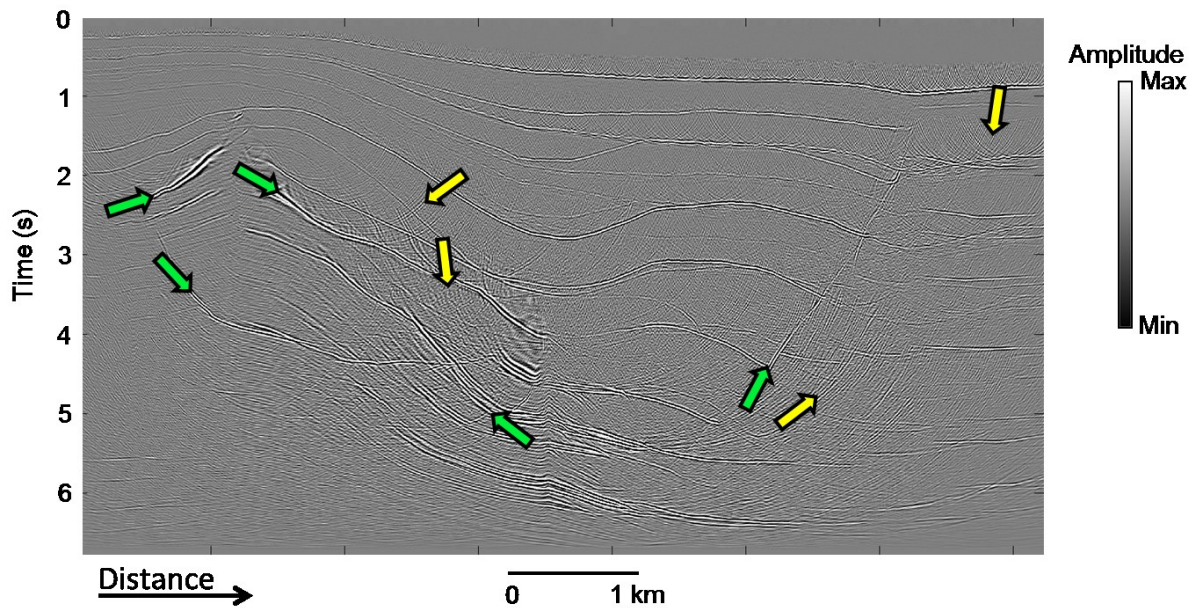


Figure 5: Migration section of a pre-stack finite difference simulation of the acoustic wave equation. Green arrows indicate where the migration operator of each CDP has constructive interference thus placing the energy of the reflection at the right location in the reflection boundary. Yellow arrows show migration artifacts that are due to the coarse surface sampling and the subsequent lack of destructive interference for steep dips (after Cabrales-Vargas, 2010).

CHAPTER II

Impact of acquisition footprint on seismic interpretation

Seismic attributes help the interpreter extract information from the seismic reflection data for qualitative or quantitative interpretation (Chopra and Marfurt, 2008). Unfortunately seismic attributes often enhance the acquisition footprint and appear as coherent, spatially-periodic artifacts overprint and often mask the geologic features of interest. In this section I will illustrate through real data examples how footprint can deteriorate the signal-to-noise ratio in seismic data and hamper the interpretation process.

Figure 6 shows a representative vertical slice through a legacy seismic amplitude volume acquired in the Delaware basin, NM. In the shallow section the footprint signature is strongest, healing with depth. More often than not this is the case for seismic reflection data where the strong, coherent noise disrupts the lower-fold shallow reflections almost making their interpretation difficult, if not impossible. Figure 7 shows a 3D view of a time slice and two vertical slices through the same seismic amplitude volume. Note the periodic pattern of amplitude anomalies seen on the time slice. Figure 8 shows a time slice at $t=0.8$ s through the corresponding Sobel filter similarity volume where subtle geologic features are overprinted by the strong acquisition footprint pattern.

Figure 9 is a representative vertical slice through the Watonga seismic amplitude volume acquired over the Anadarko Basin of Oklahoma. Although the data are contaminated with footprint, the interpretation of Skinner and Novi horizons was possible using wavelet based auto-trackers. Noisier areas contaminated by footprint needed to be reseeded and picked (Figure 10). Figure 11 shows a common workflow for time-structure map generation given noisy picks. Interpretation packages will honor faults and

discontinuities in generating time-structure maps by smoothing the picks only if there are no significant discontinuities in the analysis window. One popular smoothing process is to fit a B-spline curve to the raw picks. The algorithm removes the footprint signature while retaining the longer wavelength geologic features (Figure 12).

Figure 13 and Figure 14 show how attribute such as dip magnitude and dip azimuth computed from the time structure map exacerbate otherwise subtle footprint artifacts. Footprint has low and medium wavelength components that are not removed in this case by the surface interpolator but are preserved as if they were real features of the seismic data (Figure 15).

Although more robust than horizon-based dip magnitude and dip azimuth computations, volumetric dip magnitude and dip azimuth calculations will also be sensitive to acquisition footprint (Figure 16). Edge preserving methods, used for faults and fracture feature preservation in the data, can enhance the acquisition footprint by treating it as linear discontinuities (Figure 17). Subsequent attributes that use volumetric dip magnitude and azimuth calculations, such as similarity or curvature will inherit this footprint signature or in some cases further enhance it (Figure 18).

Footprint has also a negative impact on spectral components of seismic data. Acquisition footprint will affect the waveforms and will produce magnitude, frequency and phase anomalies (Figure 19). These anomalies will also degenerate the quality of impedance estimation thus percolating to the acoustic impedance inversion volumes (Figure 17).

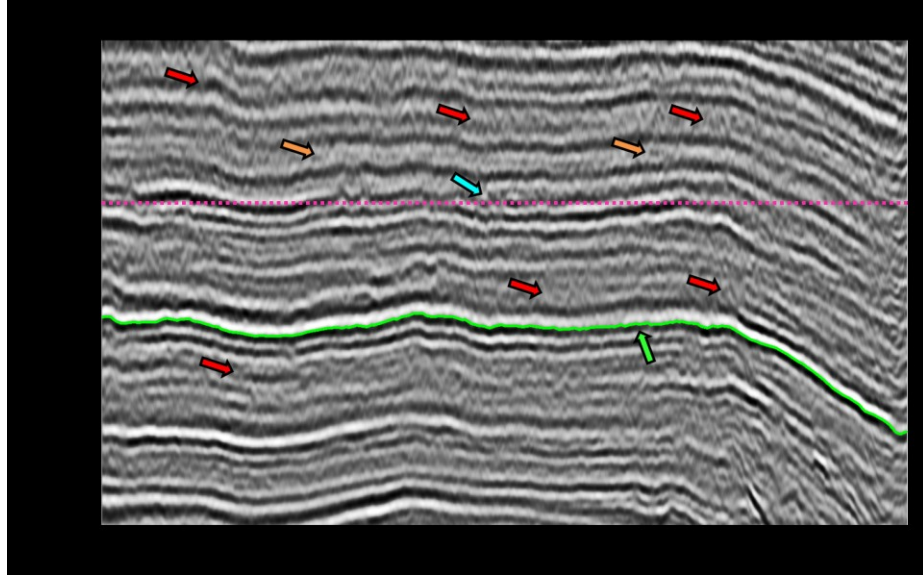


Figure 6: Representative vertical slice through a seismic amplitude volume acquired over the Delaware Basin, NM. Green arrow indicates the interpreted horizon while the magenta dotted line indicates a time slice at 800 ms. The horizon was picked following a zero-crossing. Notice that reflections are contaminated by noise (red arrows). This noise pattern heals with increasing time. Orange and cyan arrows indicate features in the data that might be channels (Seismic data courtesy of Marathon Oil Co.).

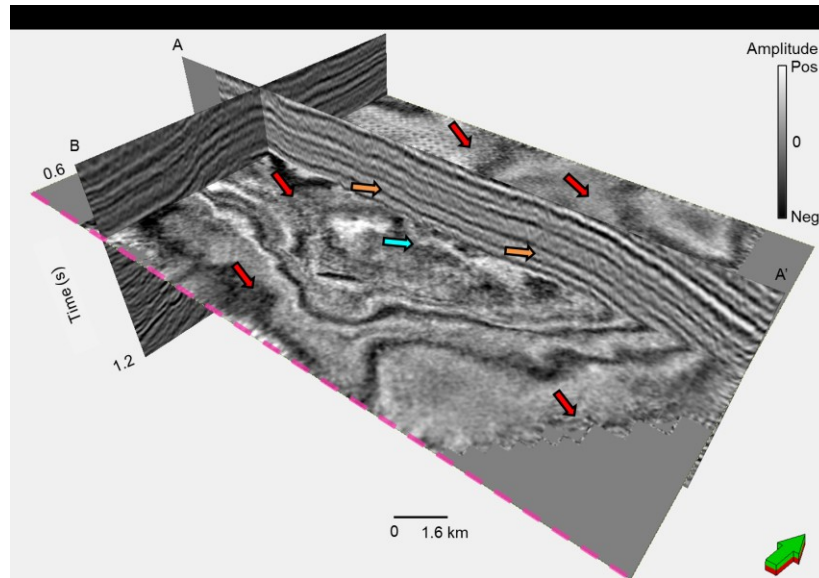


Figure 7: 3D view of time slice at $t=0.8$ s and line A-A' shown previously in Figure 6. Red arrows indicate acquisition footprint noise. Note that the features indicated by orange arrows in Figure 6 are organized rather than random, mimicking the orthogonal shot line – receiver line acquisition. Cyan arrow indicates a channel like feature that corresponds to the features observed in Figure 8.

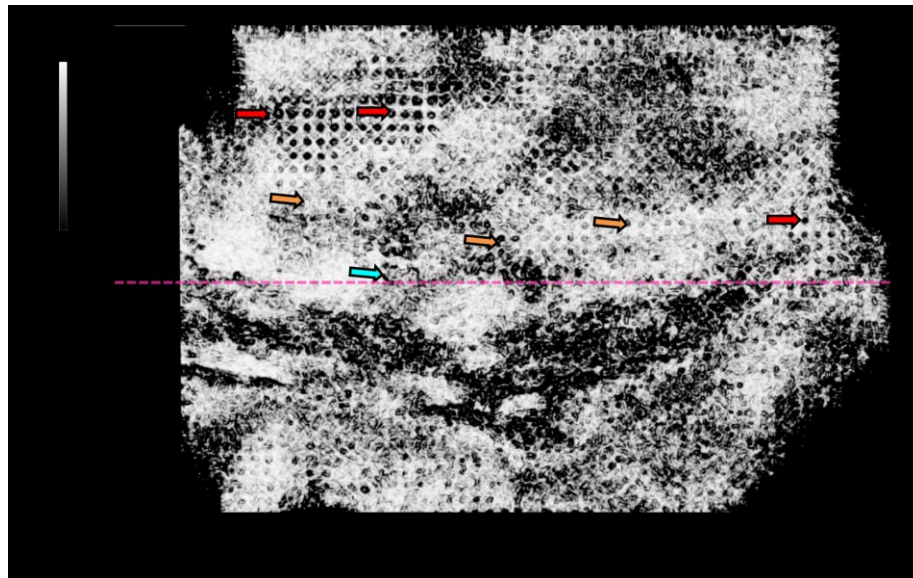


Figure 8: Time slice at $t=0.8$ s through Sobel filter similarity. Red arrows indicate acquisition footprint noise. Note that the features indicated by orange arrows in Figure 6 are organized rather than random, mimicking the orthogonal shot line – receiver line acquisition. Sobel filter similarity attribute helps to clarify that the feature indicated by the cyan arrow is a channel in Figure 6 and Figure 7.

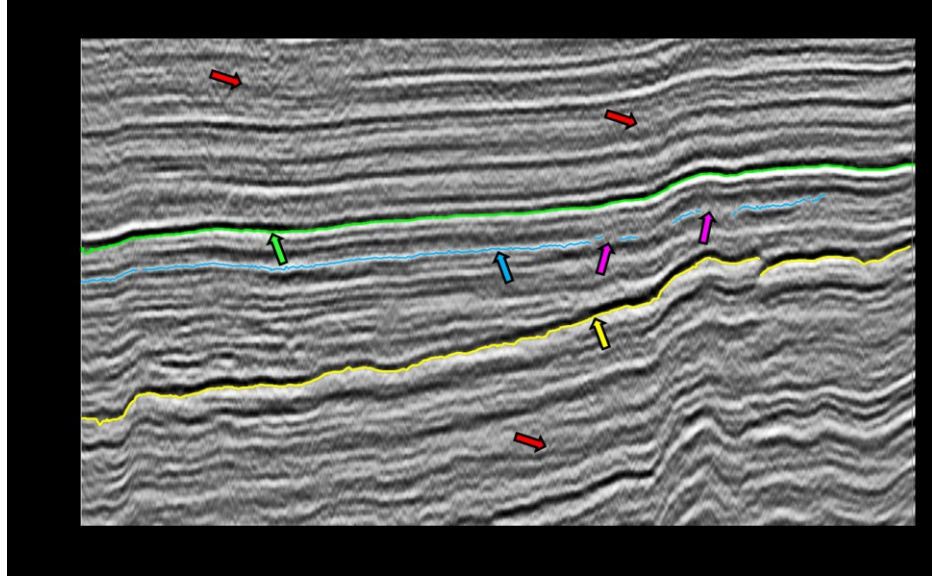


Figure 9: Representative vertical slice through the seismic amplitude volume acquired over the Anadarko Basin, OK. Green arrow indicates interpreted Skinner horizon, yellow arrow indicates interpreted Novi horizon and blue arrow indicates interpreted Red Fork horizon. All horizons were interpreted using wavelet tracking with seeded points using a correlation coefficient of 0.95 in a 12 sample symmetric vertical window. Magenta arrows indicate areas where footprint affects the performance of the wavelet-tracking algorithm. Skinner horizon and Novi horizon exhibit a lateral change in amplitudes due to the footprint but the performance of the wavelet tracking is not diminished. Red arrows indicate areas where the footprint pattern is particularly strongest.

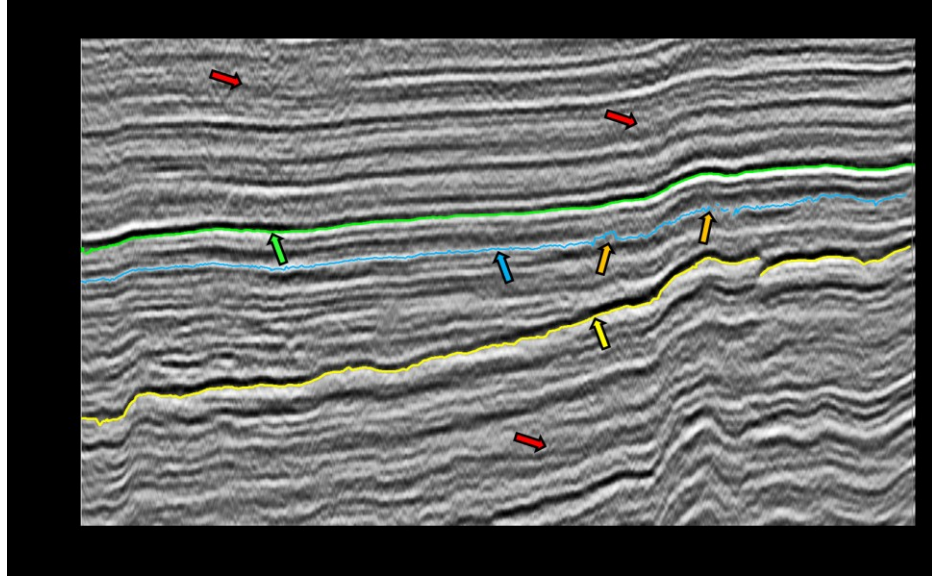


Figure 10: Representative vertical slice through the Watonga seismic amplitude volume acquired over the Anadarko Basin, OK. Green arrow indicates interpreted Skinner horizon, yellow arrow indicates interpreted Novi horizon and blue arrow indicates interpreted Red-Fork horizon. Red Fork horizon was reinterpreted using wavelet tracking with seeded points using a correlation coefficient of 0.85 in a 12 sample symmetric vertical window. Although the Red Fork horizon has been successfully picked, it is quite irregular due to the cross cutting noise (orange arrows). Red arrows indicate areas where the footprint pattern is strongest.

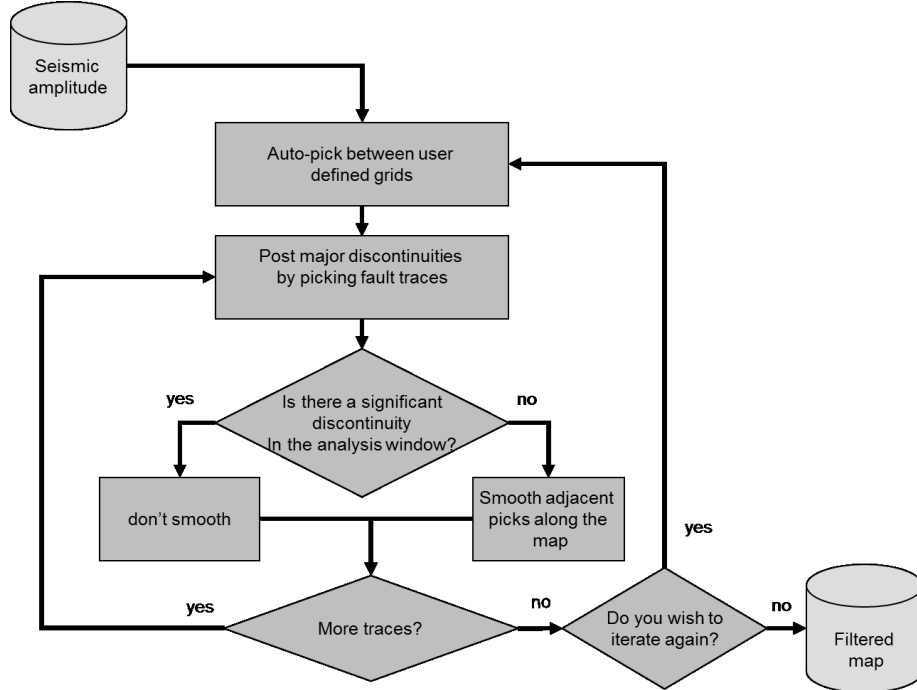


Figure 11: Workflow for generating a smooth time-structure map honoring fault traces. Most interpretation packages follow a similar flow to generate time-structure maps.

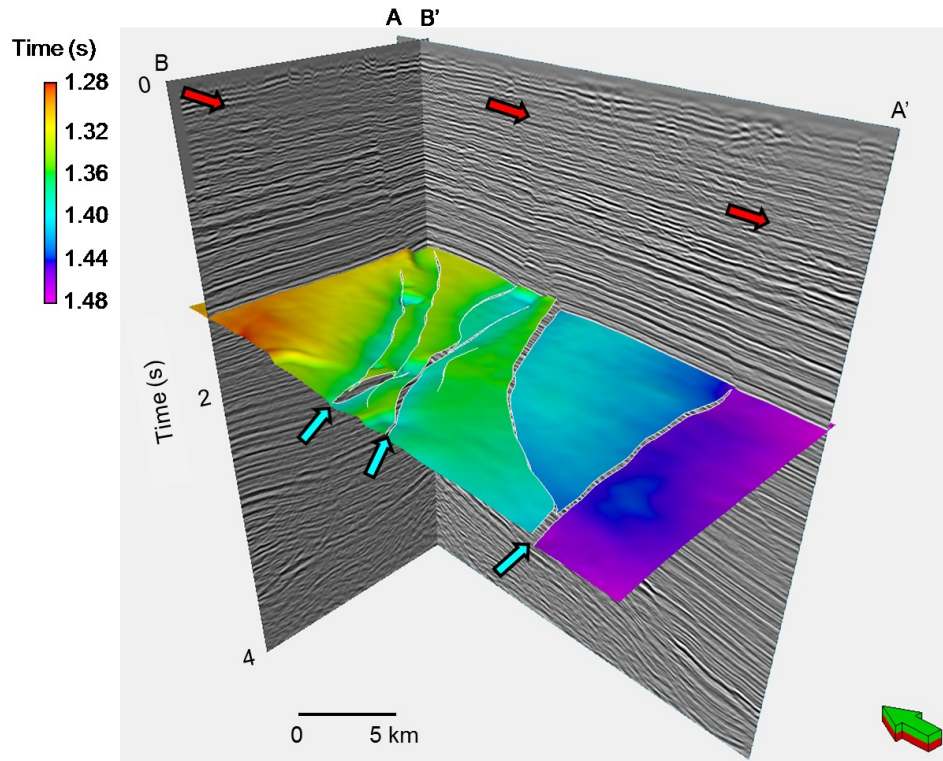


Figure 12: 3D view of time-structure map interpreted from a seismic amplitude volume acquired offshore Louisiana. Cyan arrows indicate distinctive faults that are preserved after the interpolation smoothing. Red arrows indicate noise in vertical sections (data courtesy of Schlumberger).

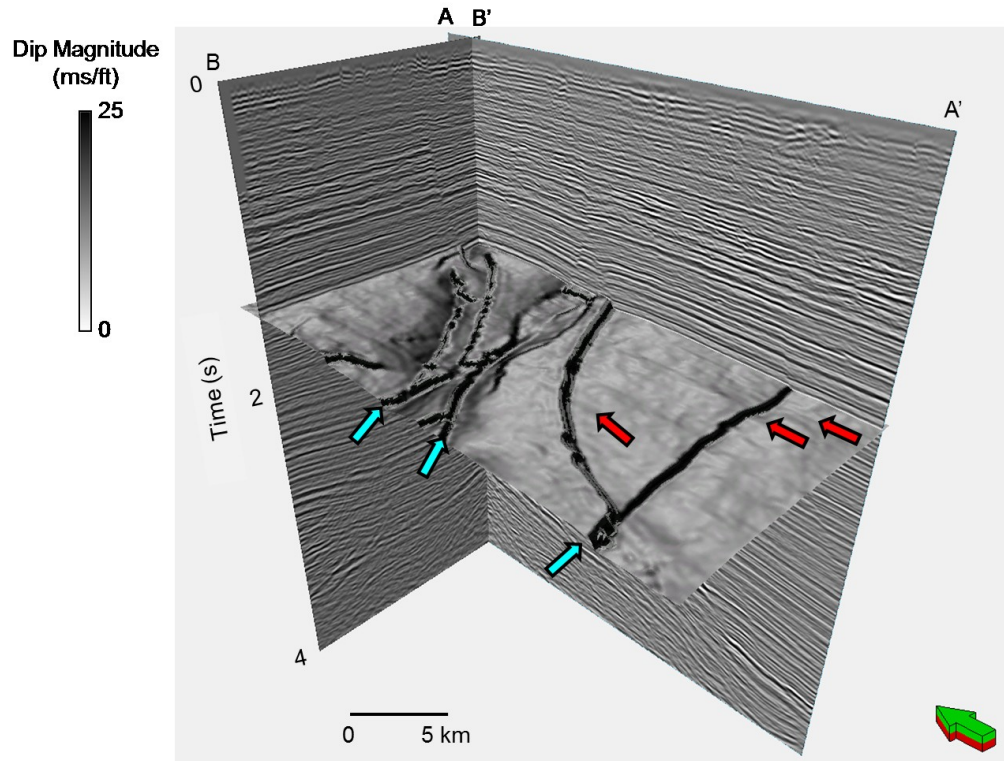


Figure 13: 3D view of the dip magnitude derived from the time-structure map shown in Figure 12. Red arrows indicate N-S artifacts in the dip magnitude map caused by the acquisition footprint.

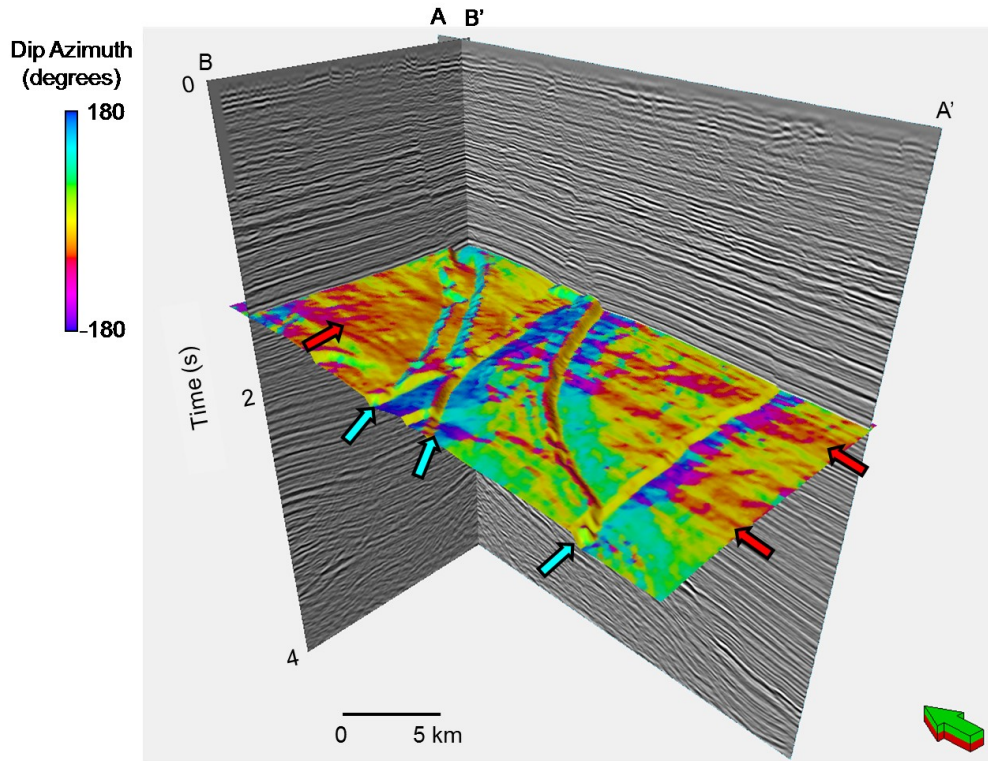


Figure 14: 3D view of dip azimuth derived from the time-structure map in shown Figure 12. Red arrows indicate zones where the footprint signature is strongest. The magenta-red color anomalies indicate dip azimuths of 90° corresponding to the N-S footprint.

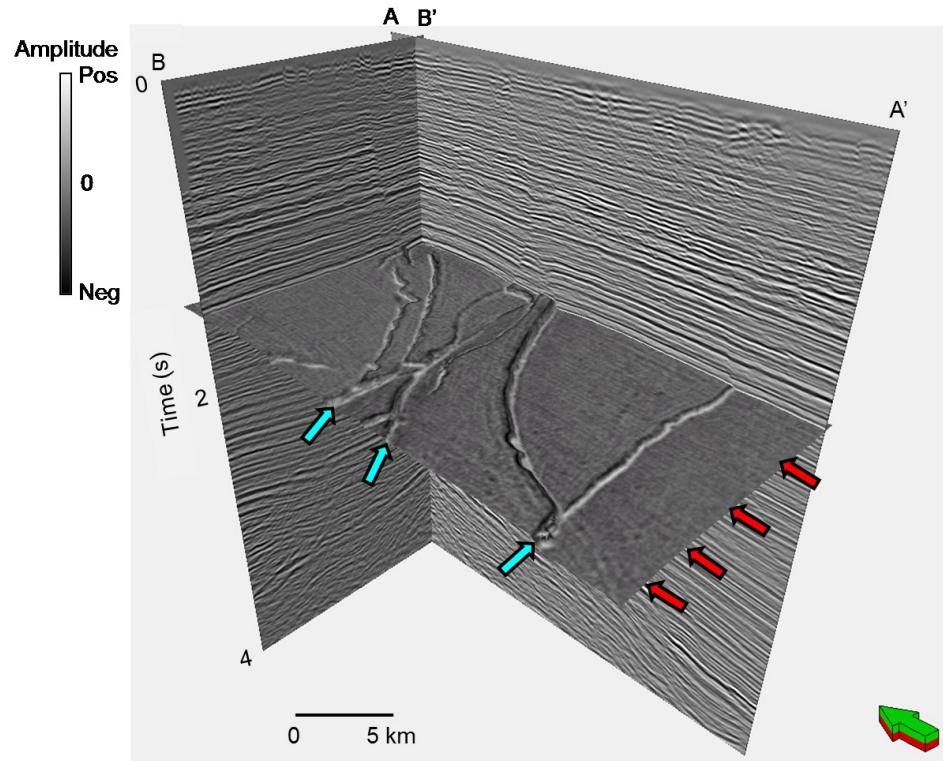


Figure 15: 3D view of seismic amplitude extracted along the time-structure map shown in Figure 12. Red arrows indicate zones where the footprint signature is strongest.

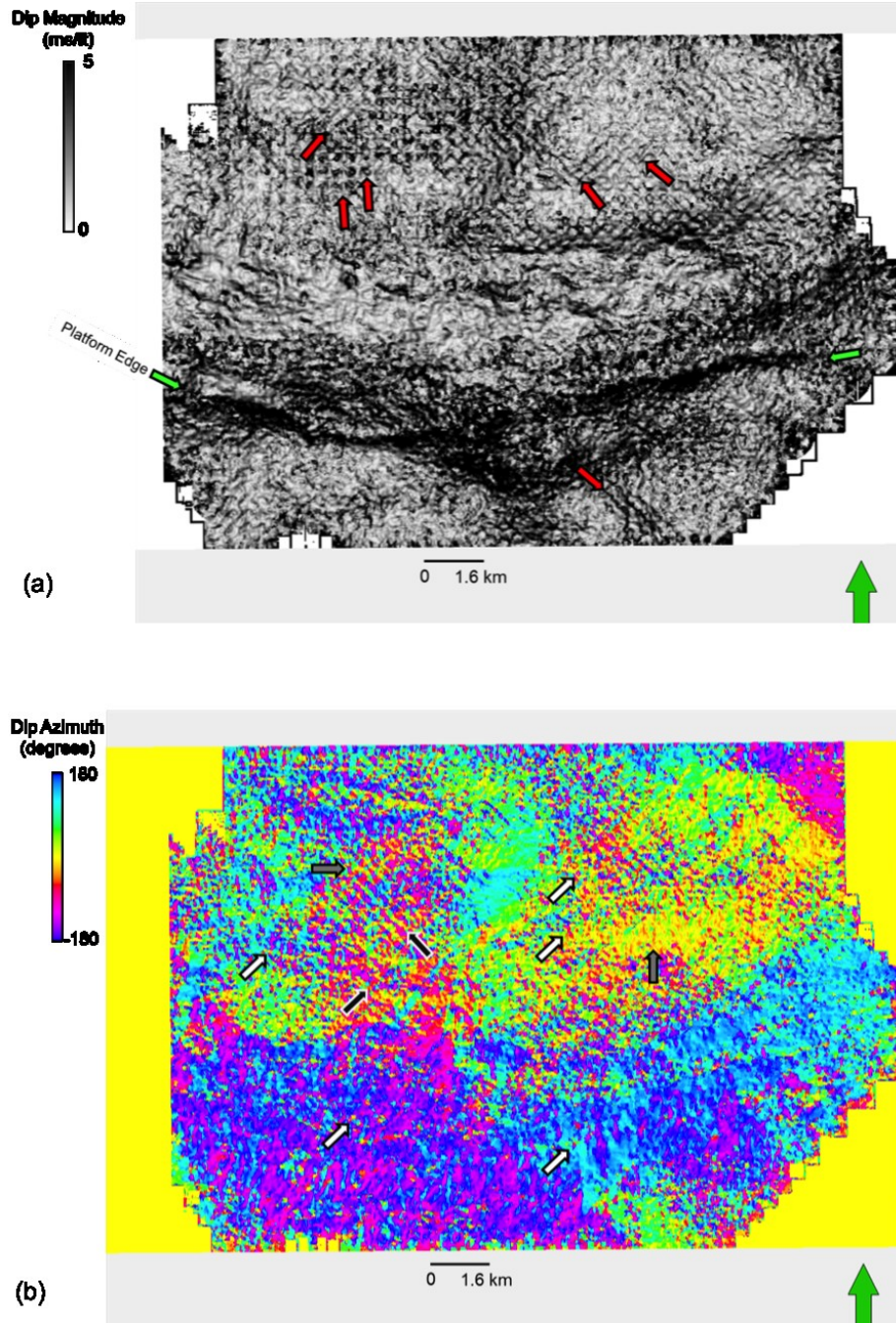


Figure 16: Time slice at $t=0.8$ s through the (a) dip magnitude and (b) dip azimuth data volumes computed from the data shown in Figure 6. Dip magnitude and azimuth were calculated using a semblance-based search within a three trace by three trace by 0.020 s analysis window. Red arrows indicate the acquisition footprint artifacts on the volumetric dip magnitude; green arrows indicate the platform edge. The footprint sometimes appears as circles (white arrows) and sometimes as a grid of NE, NW-trending (black arrows) and N-S trending (gray arrows) lineaments.

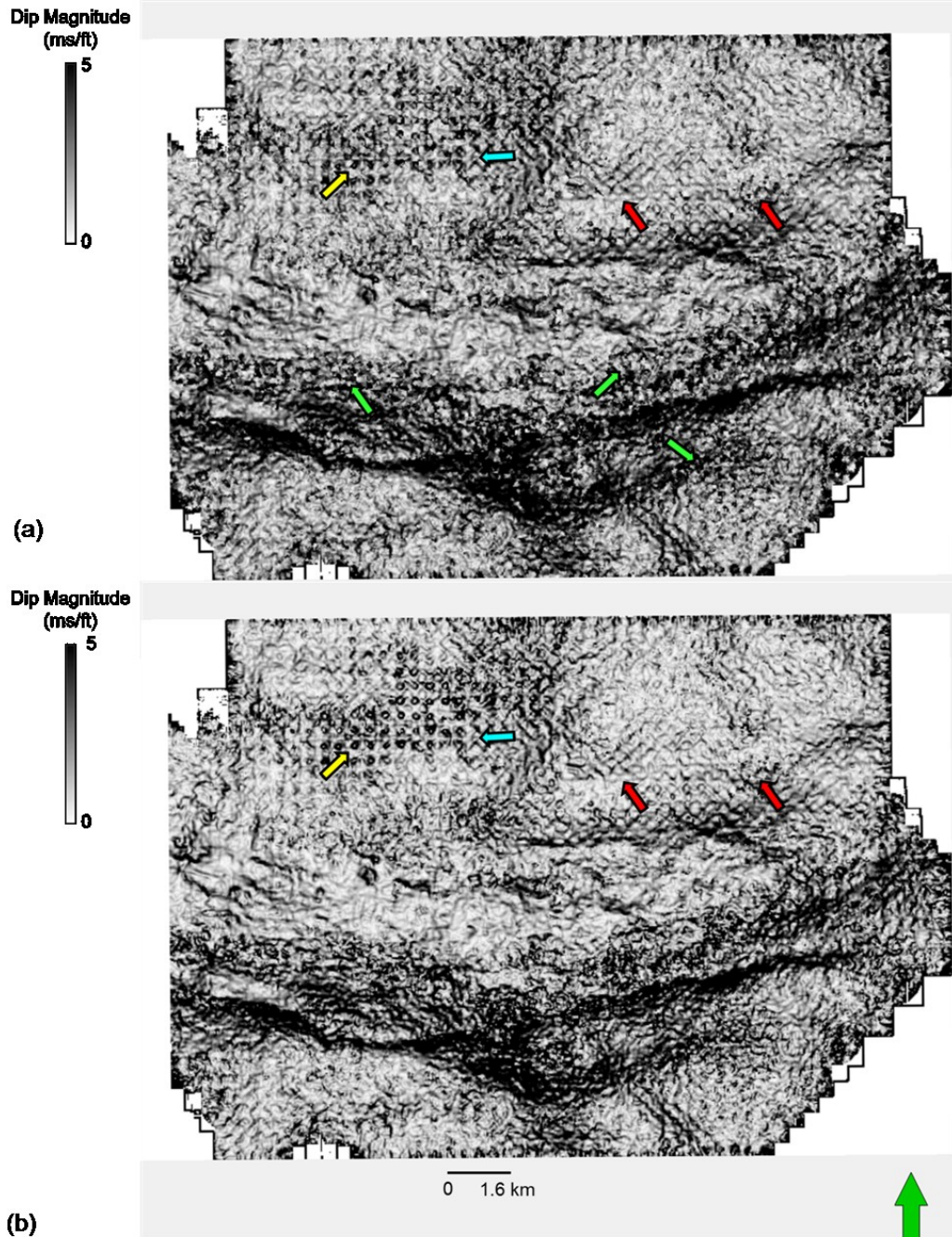


Figure 17: Time slice at $t=0.8$ s through the dip magnitude volume computed from the data shown in Figure 6. Dip was calculated using a three trace by three trace by 0.020 s analysis window with (a) nine overlapping Kuwahara windows at the analysis point and (b) a single analysis window centered about the analysis point. Yellow and cyan arrows indicate lineaments exacerbated by using nine overlapping windows method in the dip magnitude calculation. Green arrows indicate lineaments that are smoothed by using a nine overlapping windows in the dip magnitude calculation. Red arrows indicate footprint noise that remains unchanged using either method.

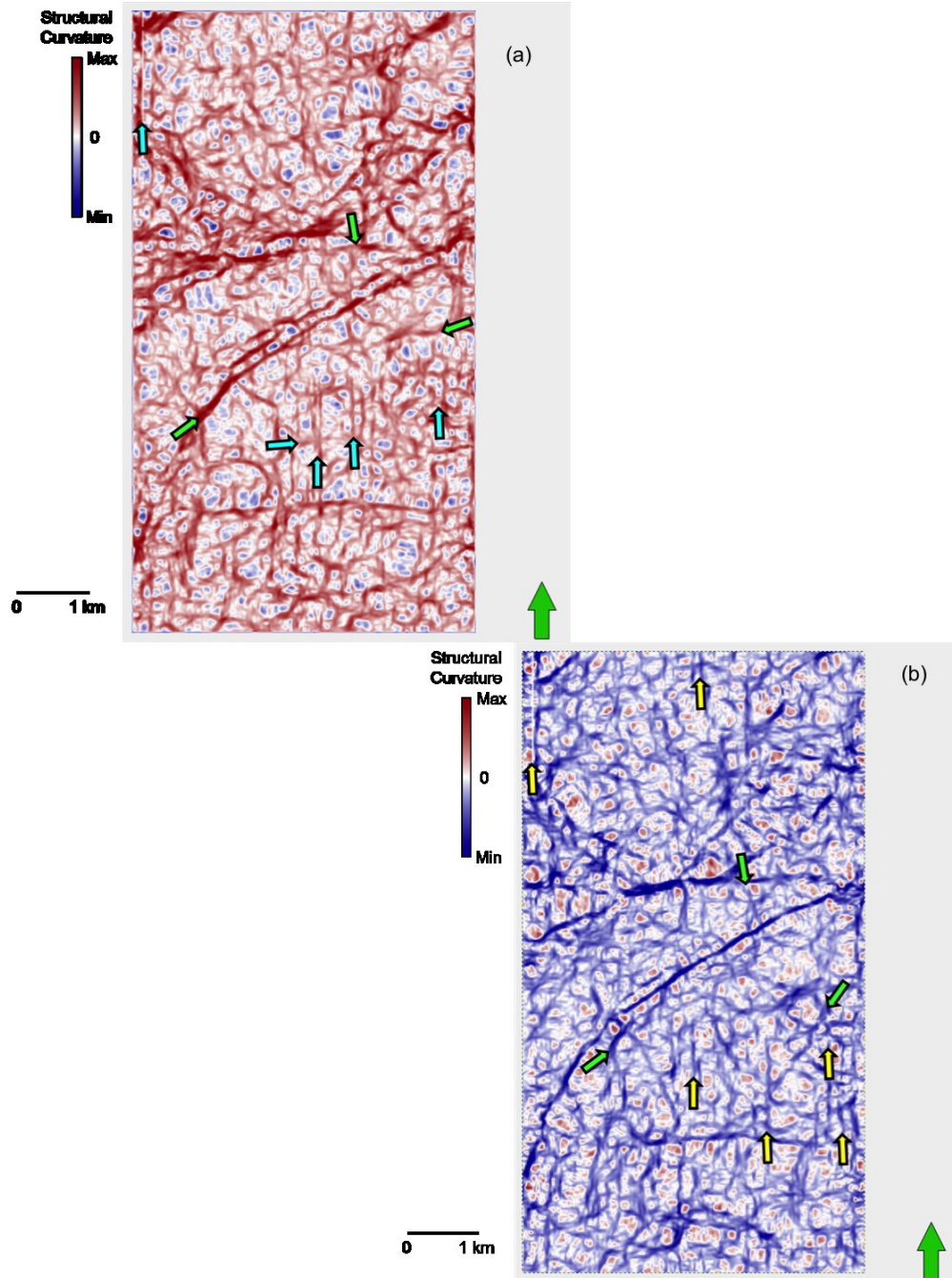


Figure 18: Time slice at $t=1.3$ s through the (a) most positive principal structural curvature and (b) most negative principal structural curvature data volumes computed from the data shown in Figure 12. (a) Green arrows indicate features that correlate to folds and faults seen on vertical slices through the seismic amplitude volume that are enhanced by the curvature attribute. Cyan and yellow arrows indicate lineaments attributed to the acquisition footprint. Most negative structural curvature seems to be more sensitive to the acquisition footprint than the most positive structural curvature for this particular data set.

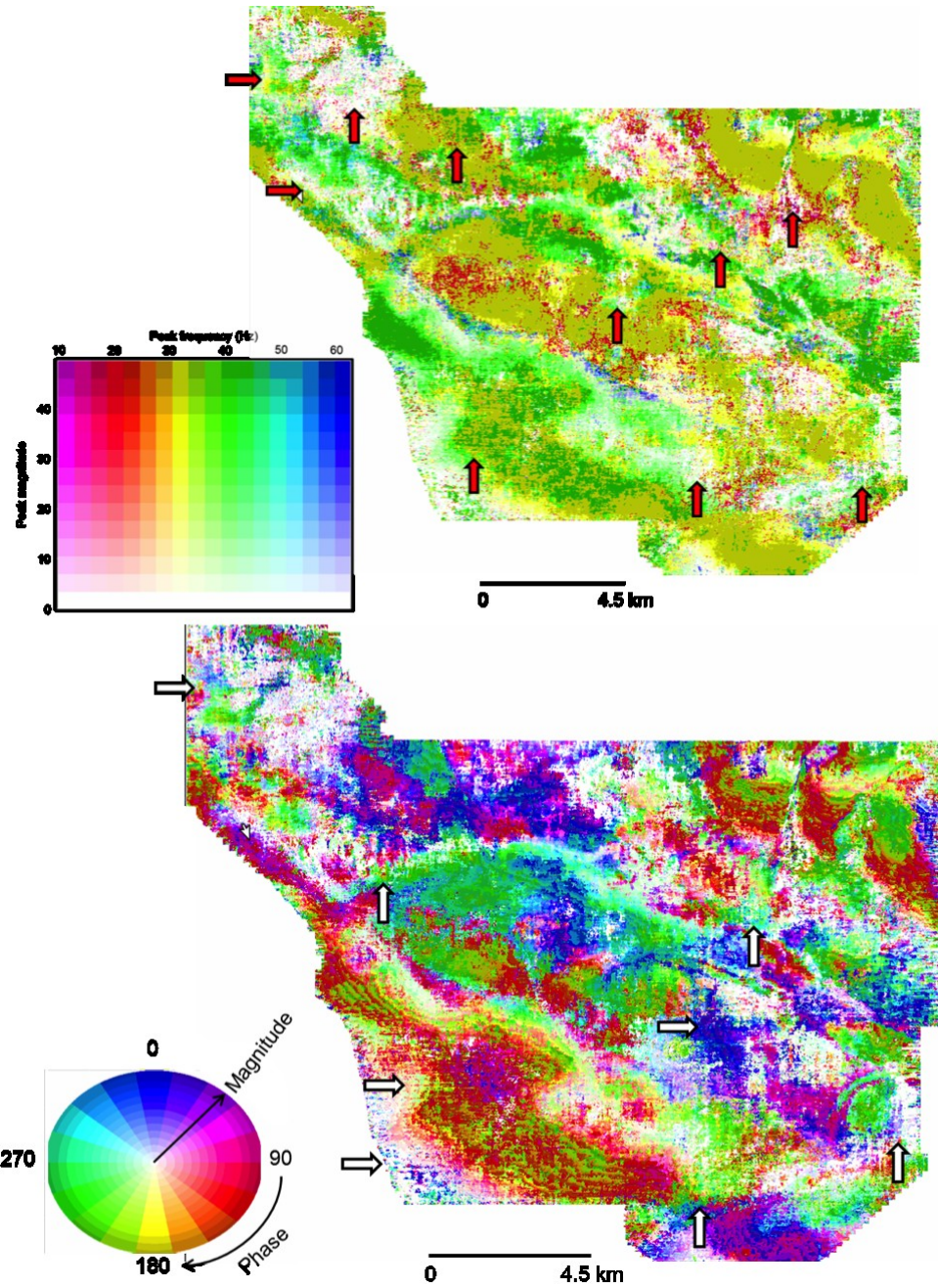


Figure 19: Phantom horizon slice 0.066 s below Skinner horizon trough (a) peak frequency modulated by peak magnitude and (b) peak wavelet phase modulated by peak magnitude using a 2D color map (Guo et al., 2008) data volumes computed from seismic amplitude volume acquired over the Anadarko Basin, OK (Figure 9). (a) Red arrows indicate acquisition footprint artifacts with a predominant frequency of 30 Hz. (b) White arrows indicate acquisition footprint artifacts seen on phase.

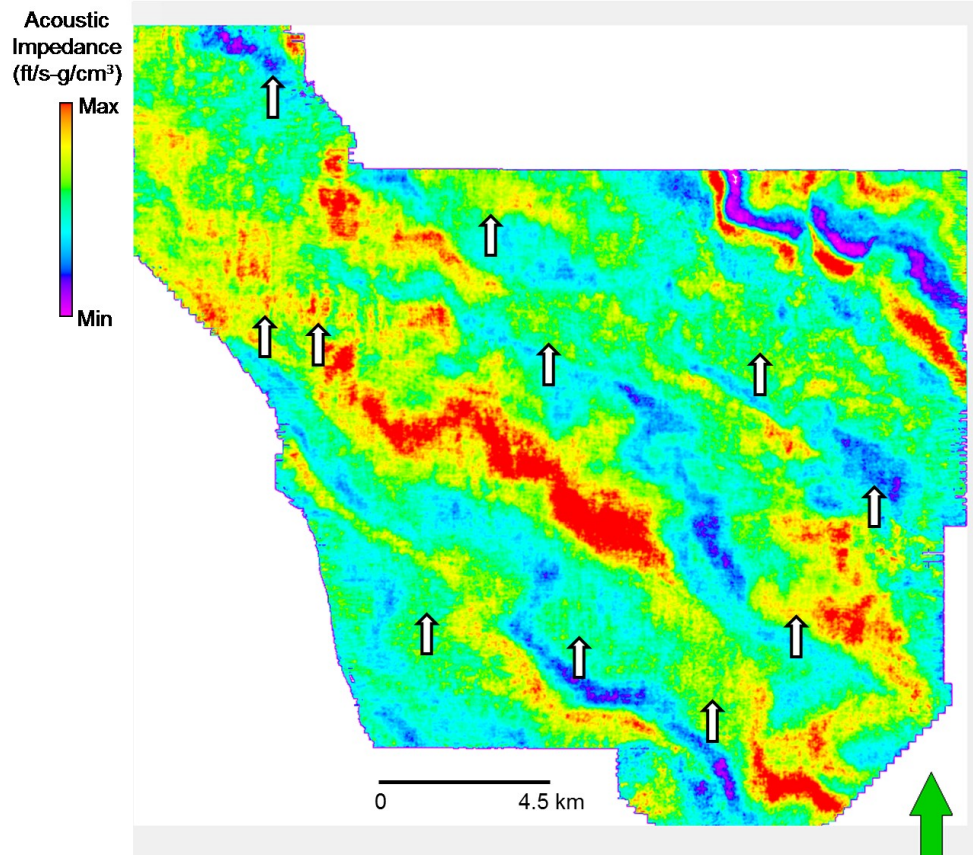


Figure 20: Time slice at $t=1.68$ s through the model based acoustic impedance data volume computed from the data shown in Figure 9. White arrows indicate acquisition footprint artifacts. Artifacts appear as N-S trending impedance anomalies that mask impedance in the reservoir interval.

CHAPTER III

Theory

In this section I review the most popular post-migration footprint suppression algorithms in order to better understand their applicability and effectiveness. I begin by discussing 2D filters applied to maps, time slices or local patches of data along a reflection.

Mean Filtering

The mean filter is the best known and simplest random noise suppression filter. It forms the basis of almost all seismic stacking algorithms. For maps and post-stack data the mean filter acts as a running-window low-pass filter that outputs the arithmetic average of all the samples that fall inside a centered analysis window. Usually the window size is an odd number for ease of implementation. Defining the analysis window along a map, a time slice, or local horizon as a suite of samples centered about a location (x_0, y_0) , the mean data filter is:

$$- \quad (1)$$

where x_j and y_j are the inline and crossline coordinates (Figure 21).

Median Filter

The median filter is also commonly implemented as a running-window filter, replacing each sample with the median of all the samples that fall within the analysis window. The median filter has the advantage over the mean filter of rejecting outliers and preserving edges. The simplest way to calculate the median for an odd number of samples is to order the samples in the window from the smallest value to the greatest value and extracting the middle one. For seismic data, the window size is typically and

odd number of $J=2K+1$ samples. If the samples are ordered from 0 to $2K$, the median value index of the sorted data is always at the k^{th} location. The order vector u_j is then

$$(2)$$

such the median is given:

$$(3)$$

α -Trimmed Mean Filter

The α -trimmed mean filter forms a continuum of filters whose end members are the median ($\alpha=0.5$) and mean ($\alpha=0.0$) filters. The data are ordered and a fraction α is rejected from both the high and low ends of the ordered data vectors before averaging, thereby eliminating potential outliers, but preserving much of the statistical power of the mean filter. If the samples are ordered following equation 2, the α -trimmed mean is given by:

$$\text{—————} (4)$$

Where the value of α varies from 0 to 0.5. Figure 22 show the effect and differences of the median, mean and α -trimmed mean filters on a test dataset.

k_x - k_y Filter

k_x - k_y filters are routinely used in the image processing industry to remove structured noise, either periodic or aperiodic, that contaminates pictures or maps. k_x - k_y filters are routinely used in filtering potential field data and are implicitly or explicitly used in upward continuation of gravity and magnetic data. Following the previous arguments we consider data volumes along a horizon slice, time slice, or local horizon slice but restrict ourselves to an S by R sample rectangular analysis window. Filters can be designed as a function of the wavenumber to remove coherent, periodic or aperiodic noise (Buttkus, 2000). The two-dimensional Fourier transform is given by:

(5)

where \hat{X} and \hat{Y} . After the transformation filtering is carried out by muting or tapering unwanted wavenumber components, after which the data are transformed back to obtain the filtered data.

Principal Component Filter

The sines and cosines that form the basis of the Fourier transform are appropriate because footprint is often periodic. However, the Fourier transform is one of many possible orthogonal data transforms we can use. We can also design basis functions from the data itself. In order to identify a pattern, we need to sample it several times. Let's examine a 21x21 inline by crossline patch of seismic amplitude extracted along horizon 1 shown in Figure 23. Such a patch forms a 441 long "sample vectors" of the seismic amplitude data (Kirlin and Dome, 1999). In order to see the pattern we need to examine more than one sample vector. In satellite imagery, we might take multiple snapshots of a fixed patch of the earth over several days. The "amplitude" of the snapshot will change due to different illumination at 9 AM, 12 noon and 5PM. Likewise, the ground surface itself may be partially obscured by clouds, the location of which may appear to be random at each satellite pass over our patch of earth. The underlying spatial pattern – rivers, roads, forest and prairie will remain fixed. In principle each snapshot should be correlated to all the others.

Let's examine 11 "sample snapshots" or "sample vectors" of our seismic patch. Clearly, we could reacquire our survey 11 times with different acquisition parameters to randomize our noise. More simply, we can assume that our seismic wavelet within the ± 5 sample window is sampling the same reflectivity. Changes in the wavelet (peak, trough,

zero-crossings) are not unlike the satellite images at different times of the day. Figure 24a shows these 11 images. If $K=5$ cross-correlation from $K=-5$ to $K=5$ of the n^{th} trace with the m^{th} trace forms the mn^{th} element of the 441 by 441 covariance matrix, \mathbf{C} :

$$(6)$$

By definition, the first principal component, also called the first eigenvector, represents the variability of the data, and for moderate amplitude noise, best represents our consistent reflectivity pattern (Kirlin and Done, 1998) as shown in Figure 24b.

For better or worse, principal component analysis has entered the seismic processing world from many directions, rendering the additional names of eigenstructure, eigenvalue-eigenvector, singular value decomposition (SVD), and Karhunen-Loeve transform analysis, causing unnecessary confusion. The eigenvectors \mathbf{v}^m of the covariance matrix \mathbf{C} are by construction unit length and orthogonal, such that they can form a basis function as we did with the k_x-k_y transform. The m^{th} component of our principal mapped data $u(x,y)$ is simply

$$(7)$$

as shown in Figure 25.

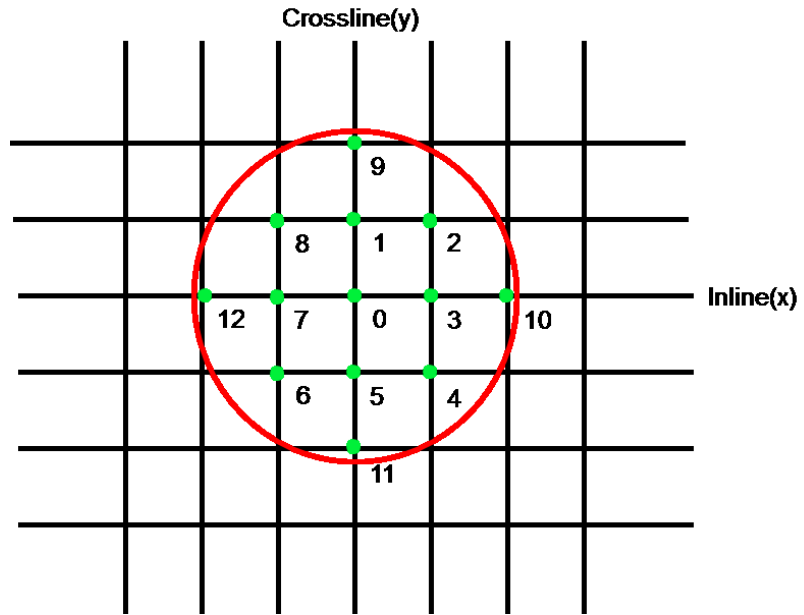


Figure 21: Example of a 13-sample analysis window centered about an analysis point at (). This analysis window is applied to every sample in the 3D volume, typically aligned along the local reflector dip. The numbering is arbitrary (in this example clockwise, reading from the center).

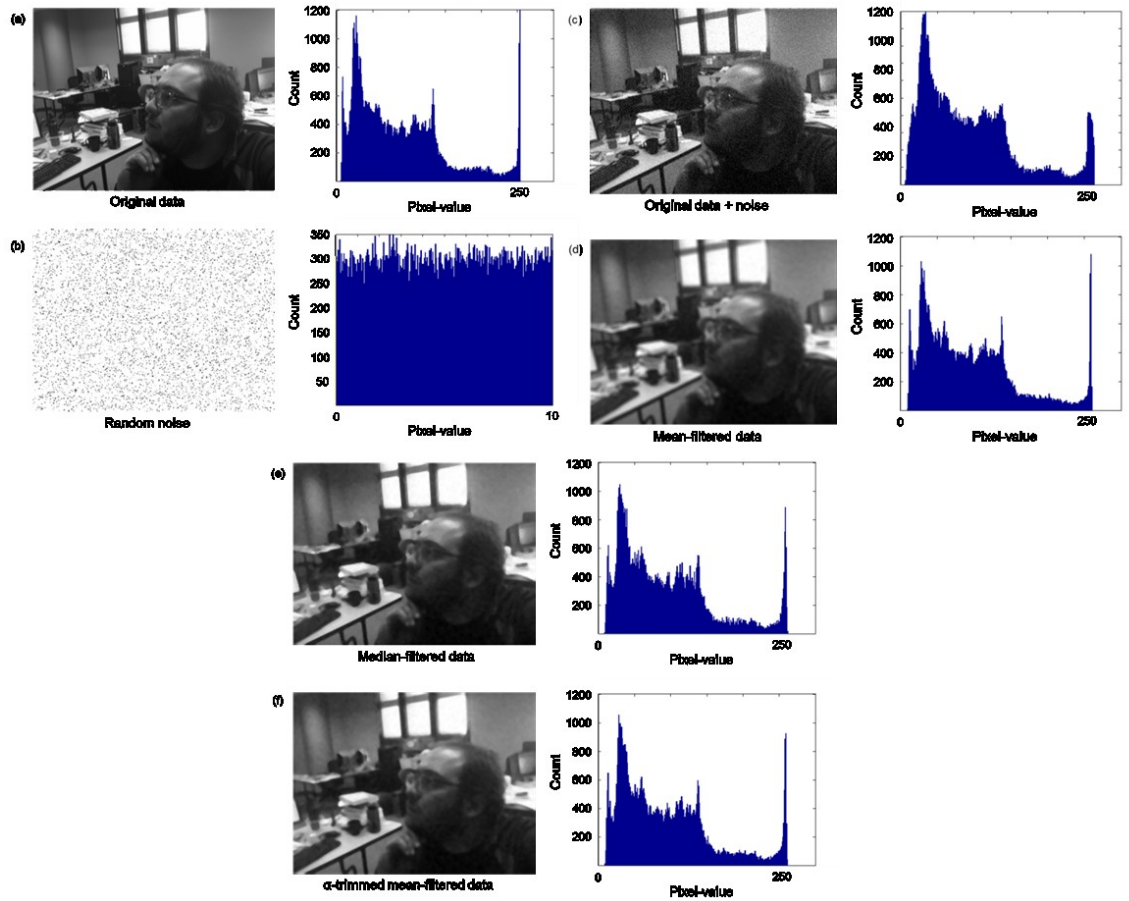


Figure 22: Effect of the mean, median, and α -trimmed mean filter on a test dataset. (a) Original data and its histogram. (b) Random noise with uniform distribution (c) Original data with added noise. (d) Mean filtered data; histogram has the same character as the original data but edges and subtle details are not preserved. (e) Median filtered data; edges are better preserved but still some subtle details are removed. (f) 20 % α -trimmed mean filtered data; edges as well as subtle detail are well preserved by this filter being a hybrid between the mean and the median filter.

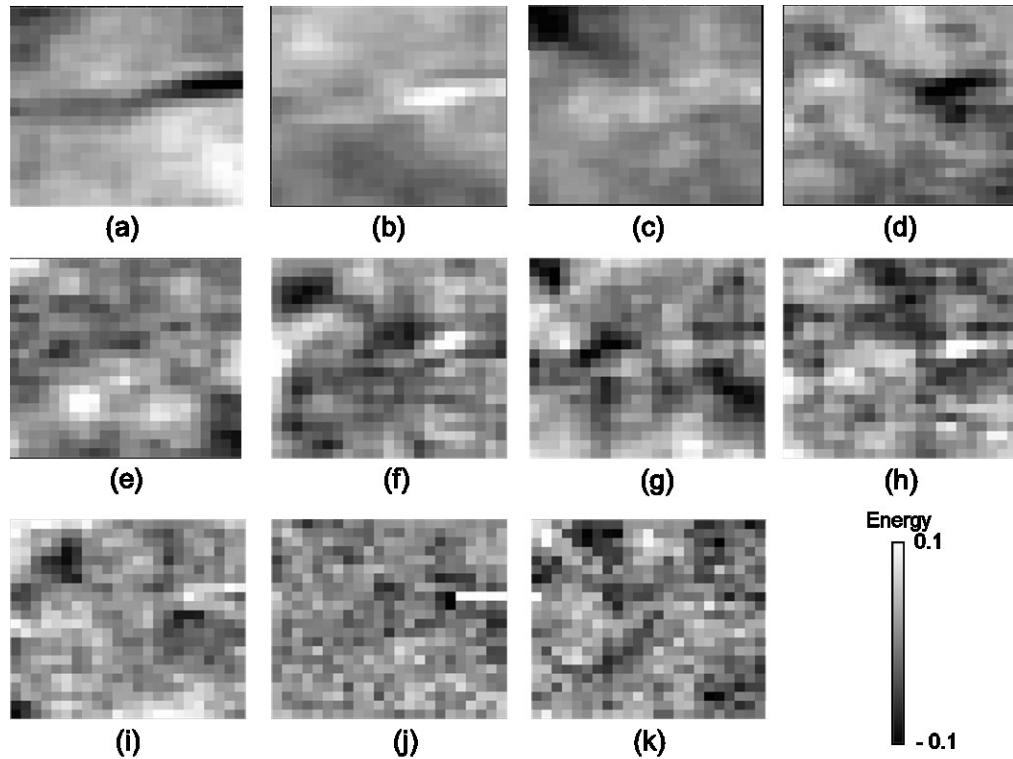


Figure 23: The first 11 of 441 eigenmaps computed from a covariance matrix generated by cross-correlating a suite of eleven 21 by 21 trace horizon slices extracted along horizon 1 shown in Figure 12. By construction, the first eigenmap (a) best represents the data variability in the eleven-sample window; the second eigenmap (b) best represents the remainder and so on. This result indicates that the coherent part of the signal will be well represented by the first four eigenmaps and the noise, either random or not, will remain on the later eigenmaps.

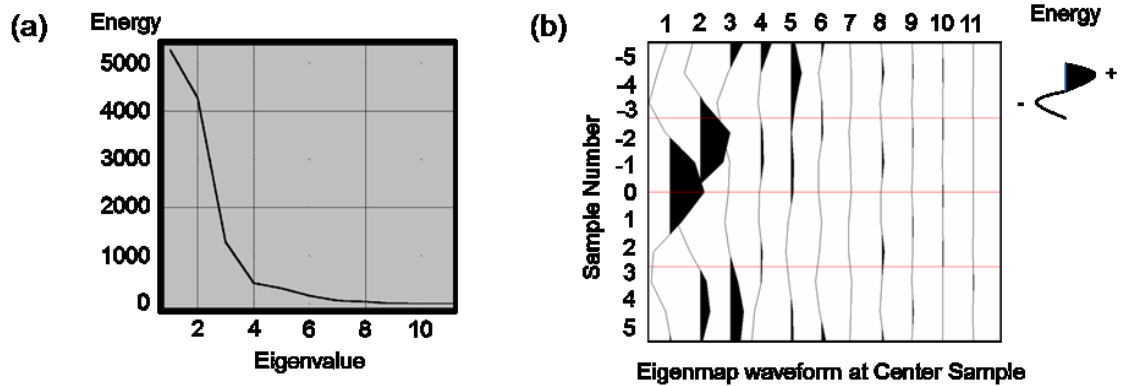


Figure 24: (a) Principal component eigenvalues corresponding to the eigenmaps shown in Figure 23 note that 19.95% of the energy is represented by the first four eigenmaps. and (b) vertical waveform centered along the horizon slice (sample $k=0$) resulting by cross-correlating the first eleven eigenmaps with eleven 21 by 21 trace phantom horizon slices centered about the picked horizon at sample 0. When cross-correlated with the data the first waveform represents the seismic traces better than the other waveform in the 21x21 trace analysis window.

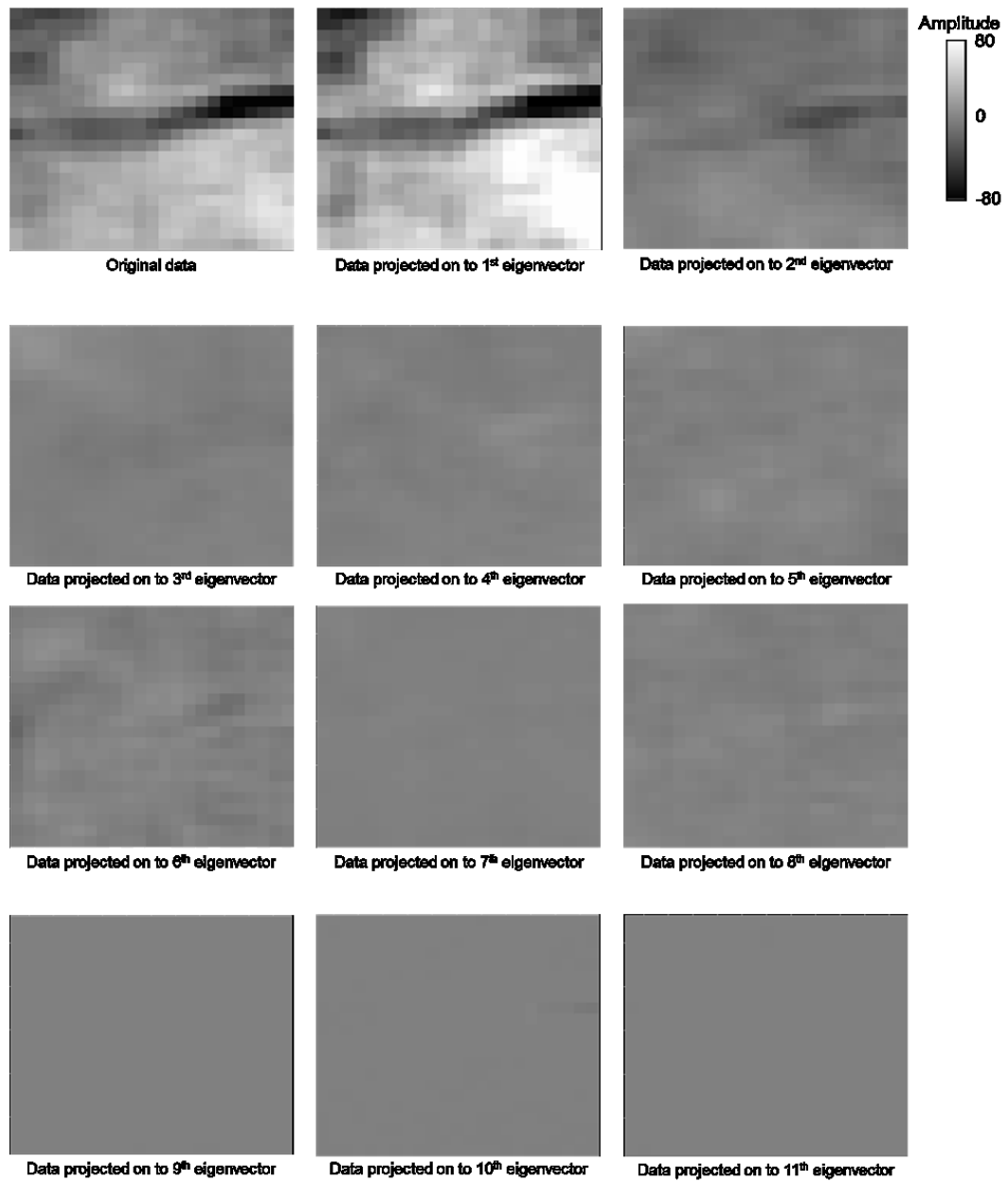


Figure 25: 21x21 inline by crossline patch of seismic amplitude extracted along horizon 1 shown in Figure 9 and its reconstruction to from the first eleven principal components. As shown in Figure 23 and Figure 24 the signal is well represented by the first four eigenmaps. The first principal component reconstruction best approximates the original data and even enhancing certain features in it.

CHAPTER IV

Evaluation of alternative filtering workflows

Filtering along horizon slices

Slowly time variant and spatially periodic noise, such as acquisition footprint, often allows seismic data filtering along constant time slices. If structure is present a best practice is to flatten the data about the target area if possible. Flattening removes the coherent short wavelength component of the signal in the spatial domain thereby allowing us to attack periodic short wavelength footprint components.

k_x - k_y filtering can often suppress periodic noise seen on time horizon slices. Figure 26 shows a generalized k_x - k_y filtering workflow following Falconer and Marfurt (2006). Since I am addressing legacy post-stack data volumes, no source or receiver geometry information is retained in the headers the first step is to generate footprint-contaminated attributes from seismic data. To estimate the noise, the footprint is enhanced and stratigraphic signal suppressed by applying a vertical median filter that removes the stratigraphic features. Along with rescaling the attribute amplitudes, a constant bias may need to be added to the attribute data to force noise free (e.g. high coherence, $c=1$) values to be the same as null values in mute and dead trace zones. Once the footprint is enhanced it is transformed to k_x - k_y space and smooth pedestal filters are generated that best represent the acquisition footprint in the seismic attribute volume.

Parallel to the footprint characterization steps described above, the seismic amplitude volume is transformed to k_x - k_y space and masked with the pedestal filters generated from the attribute data. Figure 27 summarizes the steps of the k_x - k_y footprint suppression workflow applied to the seismic data acquired over the Anadarko Basin, OK. The reverse

transform of the masked amplitude data yields modeled noise time or horizons slices that are then adaptively subtracted from the original data to produce filtered seismic data (Figure 28). Footprint sensitive attributes are computed from the filtered data to QC the filtering process and decide whether the data need more filtering or is ready for interpretation.

Although filtering in k_x - k_y space effectively removes spatially periodic and coherent noise it could be harmful to geologic features that express similar spectral components. Figure 29 shows phantom horizon slices 80 ms below the Skinner horizon in Figure 9. Most of the footprint along this phantom horizon slice has been successfully removed; however, some steeply dipping signal was also removed (red arrows). Figure 30 shows the computed frequency spectrum for the k_x - k_y filtered data and the removed noise.

Like k_x - k_y filtering, principal component analysis and filtering is most safely applied along horizons. Kirlin and Done (1998) use principal component filters in seismic processing to estimate and remove ground roll from the data. Spitz (1999) models multiple events from interpreted multiple generator primaries on 3D data volumes. This pattern is defined as a spatial eigenmap that contains the phase shift and lateral amplitude variation from trace to trace but excludes the waveform of the event.

In our case we will use principal components to determine piecewise planar events that have a fixed waveform that best fit the data along reflector dip and azimuth, to model the “coherent” part of the signal (Figure 31). The n^{th} principal component is given by:

$$(8)$$

where $\mathbf{v}^n(t)$ is the n^{th} eigenmap calculated from the covariance matrix \mathbf{C} . Marfurt (2006) describes a covariance matrix aligned with reflector dip components (p,q) measured in s/m, in a $(-K, +K)$ vertical window centered about $(x_0=0, y_0=0)$:

$$\bar{v}^n(t) = \frac{1}{2K} \int_{-K}^{+K} v^n(t) dt \quad (9)$$

where the superscript H denotes the Hilbert transform of the data and the bar denotes the mean values in the $(-K, +K)$ sample window.

Since principal component analysis implicitly computes a fixed waveform for each event (Figure 24b), principal component analysis is best applied along dip and azimuth. Such flattening ensures correlation in constructing the covariance matrix of events from the same reflector. Al-Bannagi et al., (2005) applied principal components (or SVD) filtering to suppress footprint in a 2D by 2D implementation. Figure 32 shows a 3D implementation applied to seismic data acquired over the Anadarko Basin, OK using the first, second and third principal components.

Structure Oriented Filtering (SOF)

Filtering along horizon slices reduces a 3D problem to series of 2D problems. Although proven effective for slowly time variant and spatially-periodic noise, 2D transformations are not as robust when the data are contaminated with time-and-space variant noise. In such situations, a 3D implementation of filters will better estimate the noise and separate it from the signal. Footprint will change with depth if there are lateral velocity changes in the overburden. Filter parameters include lateral and vertical window size, edge preservation techniques and smoothing criteria used.

Edge preservation techniques

Fehmers and Höecker (2003) introduced the concept of Structure Oriented Filter (SOF) as a stepwise removal of noise (Figure 33). Smoothing is applied parallel to reflector dip and azimuth so long as a significant discontinuity does not exist. Figure 34 shows my workflow to estimate the degree of smoothing using a similarity attribute implemented in my modification of a SOF algorithm. Figure 35 shows the effect of using Sobel filter similarity as a degree of smoothing factor is tested on the offshore Louisiana data.

Marfurt (2006) built on Luo et al., (2002) Kuwahara algorithm to implement a robust volumetric dip and azimuth calculation that avoided smearing of faults, fractures and other discontinuities using an overlapping window method (Figure 36 and Figure 37). This technique along with the seismic data input can be used to implement volumetric filters based on mean, median, α -trimmed mean or principal component algorithms (Figure 37). Rather than using a centered analysis window, the algorithm uses the most coherent window containing each analysis point, hence enhancing the lateral resolution and reducing both random and coherent noise (Marfurt, 2006). Figure 38 shows the results of this overlapping window filtering technique applied to the offshore Louisiana data. Figure 39 and Figure 40 show a comparison of each technique impact on the offshore Louisiana data.

Sensitivity to smoothing algorithm

As with the edge preservation techniques, filtered data will be sensitive to our algorithm selection. Mean, median and α -trimmed mean filters will work best in areas where the data has random incoherent noise but might misestimate the amplitude. Median and α -trimmed mean filters are relatively insensitive to spikes in the data. Principal

component filters will diminish random noise and better preserve lateral variations in signal amplitude (Figure 41). Figure 42-Figure 45 show filtered data from offshore Louisiana (Figure 12) using mean, median, α -trimmed mean and principal component algorithms respectively and their differences with respect the original data.

Special care has to be taken when using principal component filters as to how many eigenvectors are going to be used for filtering the data. In some cases subtle geologic features such as small faults and channels may be represented by second and the third eigenmaps. If only the first eigenmap is used, subtle geologic features may be also removed (Figure 46).

Sensitivity to horizontal window size

Horizontal window parameter modulates the degree of smoothing in the horizontal direction having a direct impact upon the filtered seismic data. For the mean, median and α -trimmed mean filter the influence of the horizontal window size will enhance the results by adding more sample points to the statistics of the analysis window. Figure 47 shows the impact of varying the horizontal analysis window size to the filtered data for the offshore Louisiana data set.

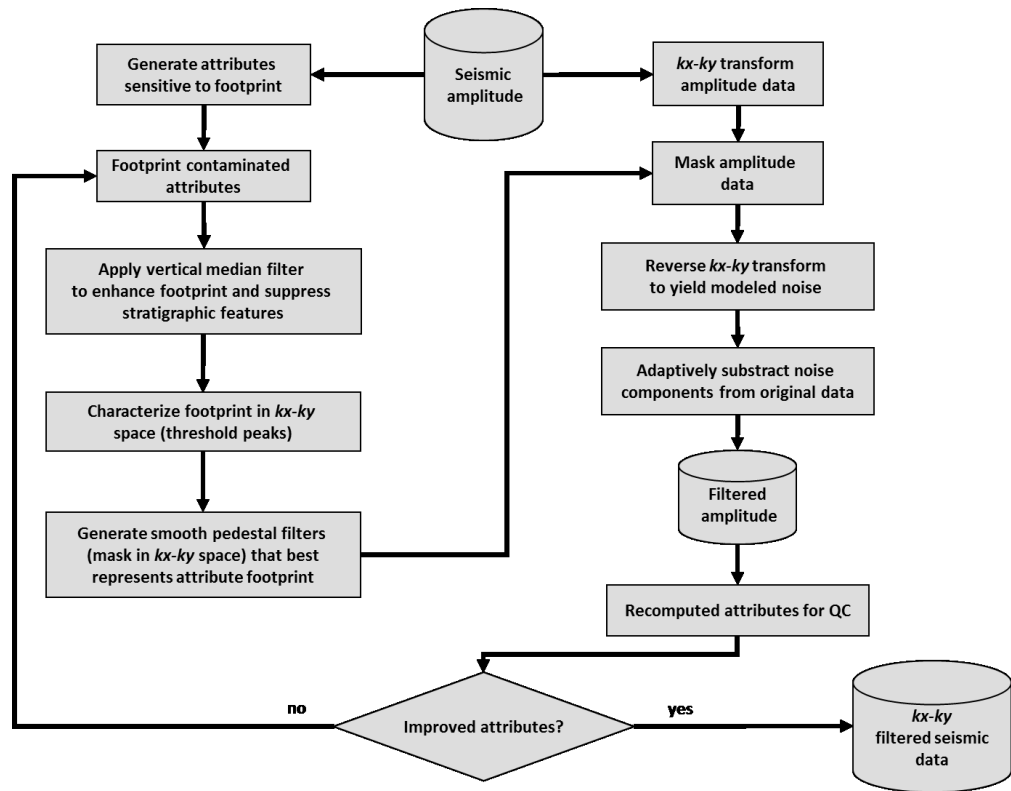


Figure 26: k_x - k_y filtering workflow for seismic amplitude data using seismic attribute pattern recognition described by Falconer and Marfurt, 2006.

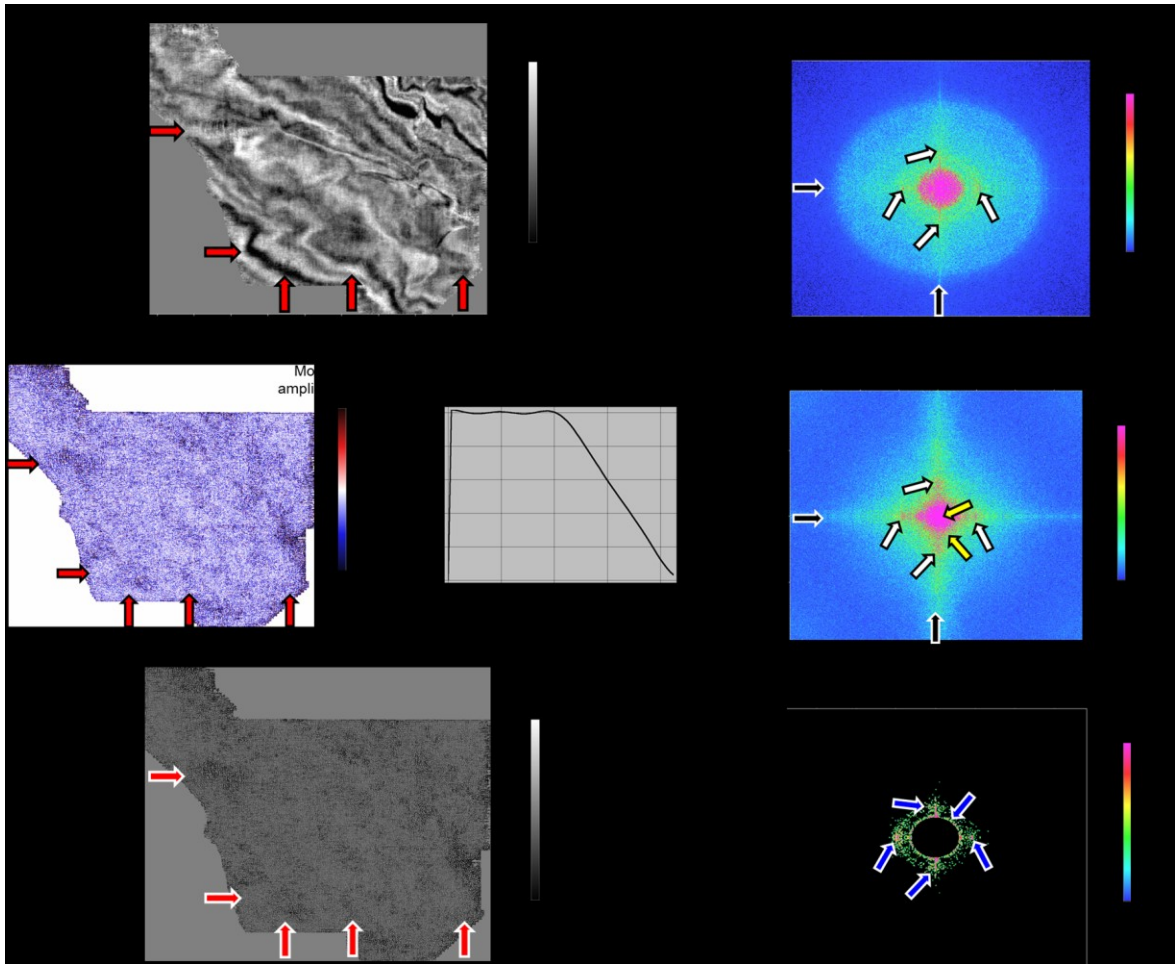


Figure 27: Application of footprint suppression workflow shown in Figure 26 to the seismic amplitude volume acquired over the Anadarko Basin, OK. (a) Time slice through seismic amplitude at $t=1.6$ s horizon shown in Figure 9. Red arrows indicate footprint anomalies on the data. (b) Corresponding time slice through most negative amplitude short wavelength curvature exacerbating short wavelength footprint anomalies and its derivative spectrum. (c) Time slice through smoothed most negative amplitude curvature at $t=1.6$ s after median filter to suppress any remaining signal of the geologic features and enhance vertical footprint features. (d) Time slice through most negative amplitude curvature at $t=1.6$ s in the k_x-k_y domain. White arrows indicate peak amplitude anomalies due to the footprint signal in the attribute. Black arrows indicate N-S and E-W anomalies that correlated to the survey edges as well as footprint. (e) Time slice through seismic amplitude at $t=1.6$ s in the k_x-k_y domain. Most of the smooth, relatively flat signal will cluster near the origin (yellow arrows) whereas lineaments such as faults and channels will be scattered at larger values of k_x-k_y . White arrows indicate zones where noise clusters are present. Black arrows indicate anomalies due to the survey edges. (f) Notch filter pedestals. Counter intuitively in this step the signal is removed from the data in order to model the noise components. Noise (blue arrows) will then be adaptively subtracted from the data for a noise reduced seismic amplitude volume.

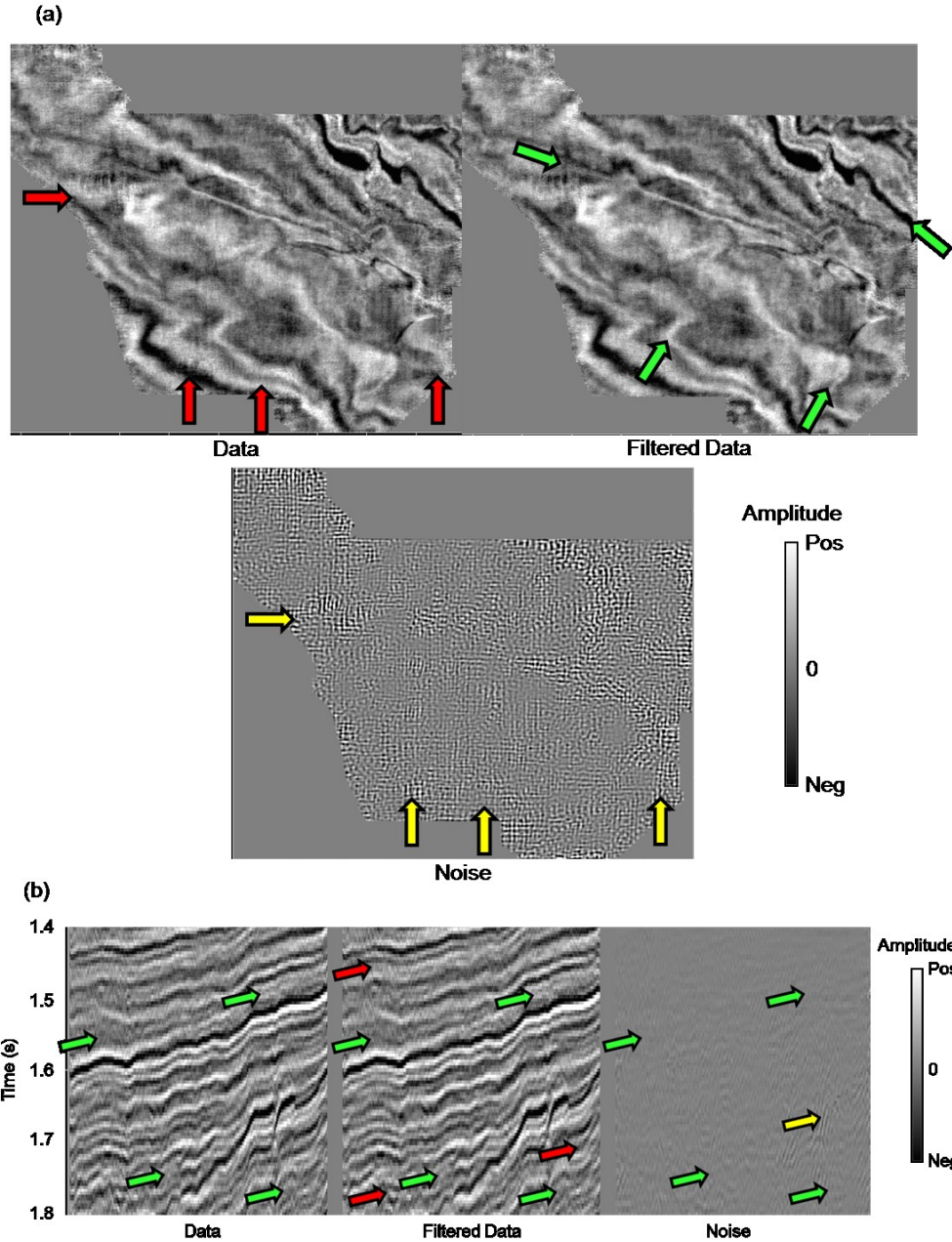


Figure 28: (a) Time slices at $t=1.6$ s through: original seismic amplitude data, k_x-k_y , filtered seismic amplitude data and noise pattern for the dataset acquired in the Anadarko Basin, OK. Notice that most of the N-S and E-W lineaments present due to the footprint in the original data have been removed. Green arrows indicate geologic features that have been enhanced after the filtering. Yellow arrows indicate footprint pattern characterized by the k_x-k_y filter and removed from data. (b) Representative vertical section through the original seismic amplitude data, filtered seismic amplitude data and noise pattern for the dataset acquired in the Anadarko Basin, OK. Green arrows indicate areas where the signal-to-noise ratio has increased compared to the original data. Red arrows indicate areas where noise was removed but it is still present. Yellow arrow indicates geologic features removed by the filtering process represented by a k_x-k_y “noise” component.

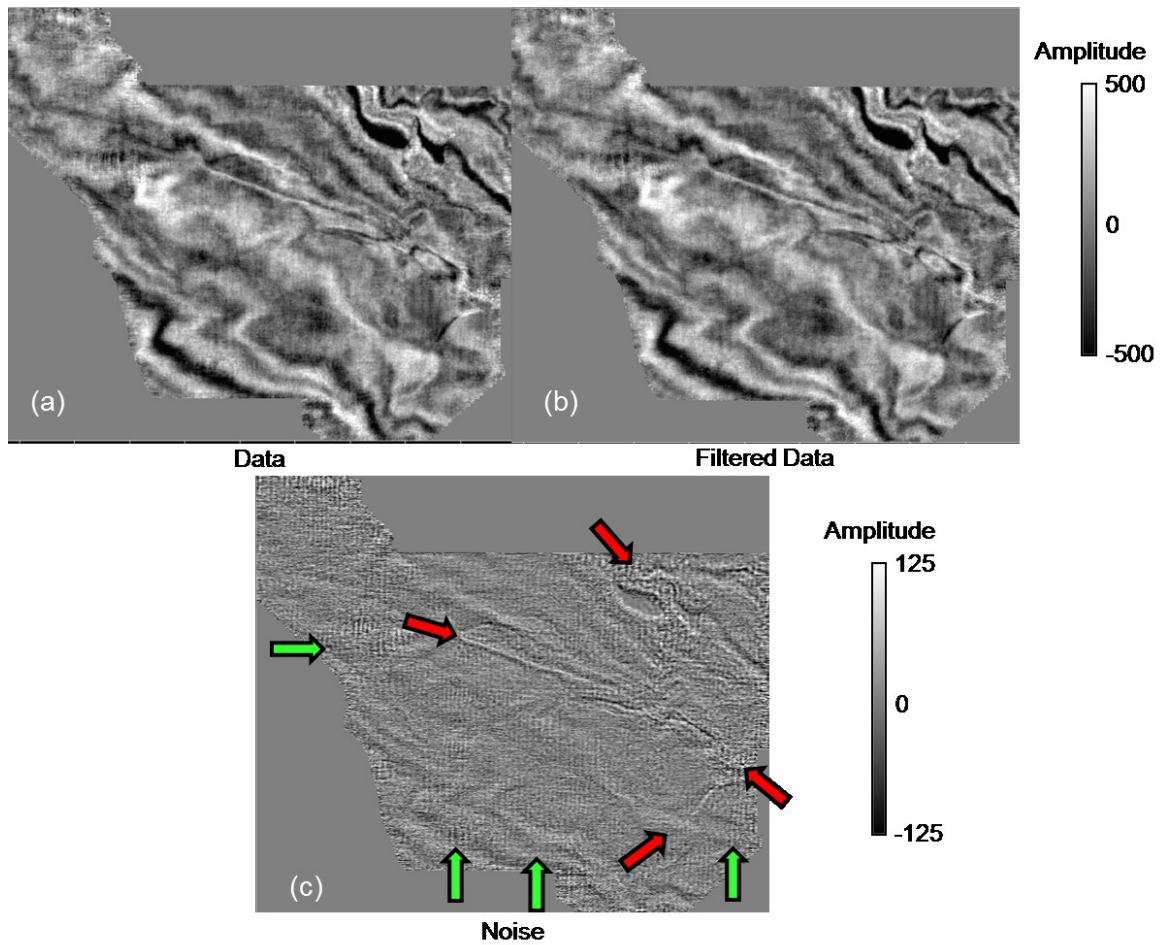


Figure 29: Time slice at $t=1.6$ s through (a) original seismic amplitude data, (b) k_x - k_y filtered seismic amplitude data and (c) removed noise for the dataset acquired in the Anadarko Basin, OK. Distinctive geologic features can be observed in both the original and filtered data. Filtered data displays sharper and better defined channels and features than the original data. Unfortunately part of the signal present in the data was also removed, dimming certain features indicated by red arrows. Green arrows indicate footprint removed. Note the difference in amplitude scales.

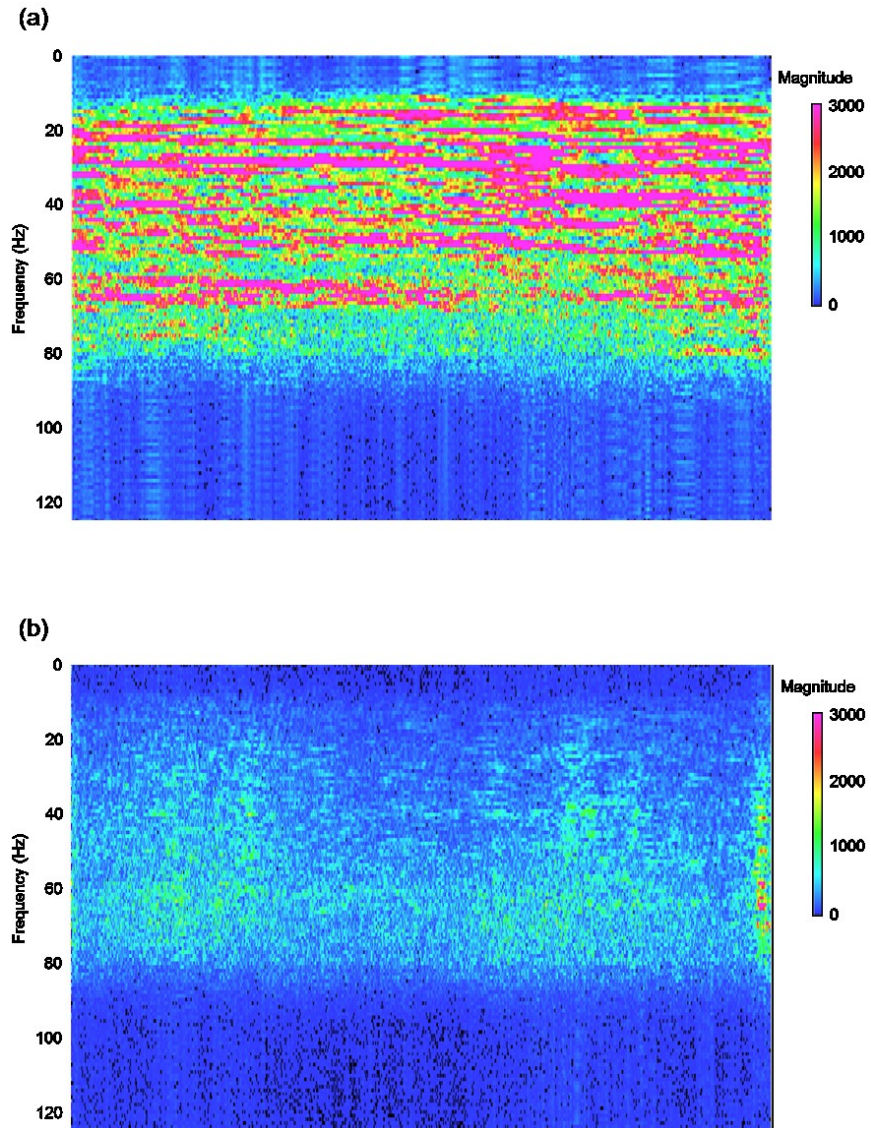


Figure 30: Representative section through frequency spectrum calculated for (a) k_x - k_y filtered seismic amplitude data and (b) noise pattern for the dataset acquired in the Anadarko Basin, OK. Most of the signal in the filtered data is in the 20 to 70 Hz band. Magnitude trough the vertical section shows a regular character. The noise spectrum appear to be contained in the 60 to 80 Hz with “bursts” in the lower frequencies.

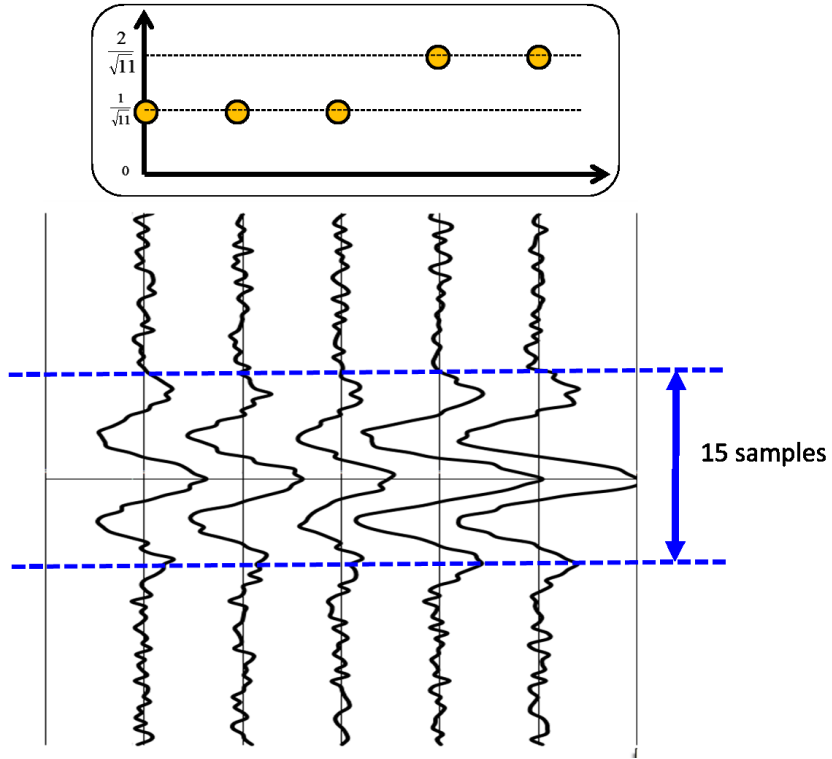


Figure 31: A window of five noise-contaminated traces having the same underlying waveform, but with different amplitudes (1, 1, 1, 2, 2). The first eigenvector or principal component, are amplitudes that best represent this lateral variation within the vertical analysis window. By convention, the eigenvector is normalized here by $\frac{1}{\sqrt{11}}$ to have length 1.0, giving rise to the eigenvector $\mathbf{v}^T = \frac{1}{\sqrt{11}} [1, 1, 1, 2, 2]$.

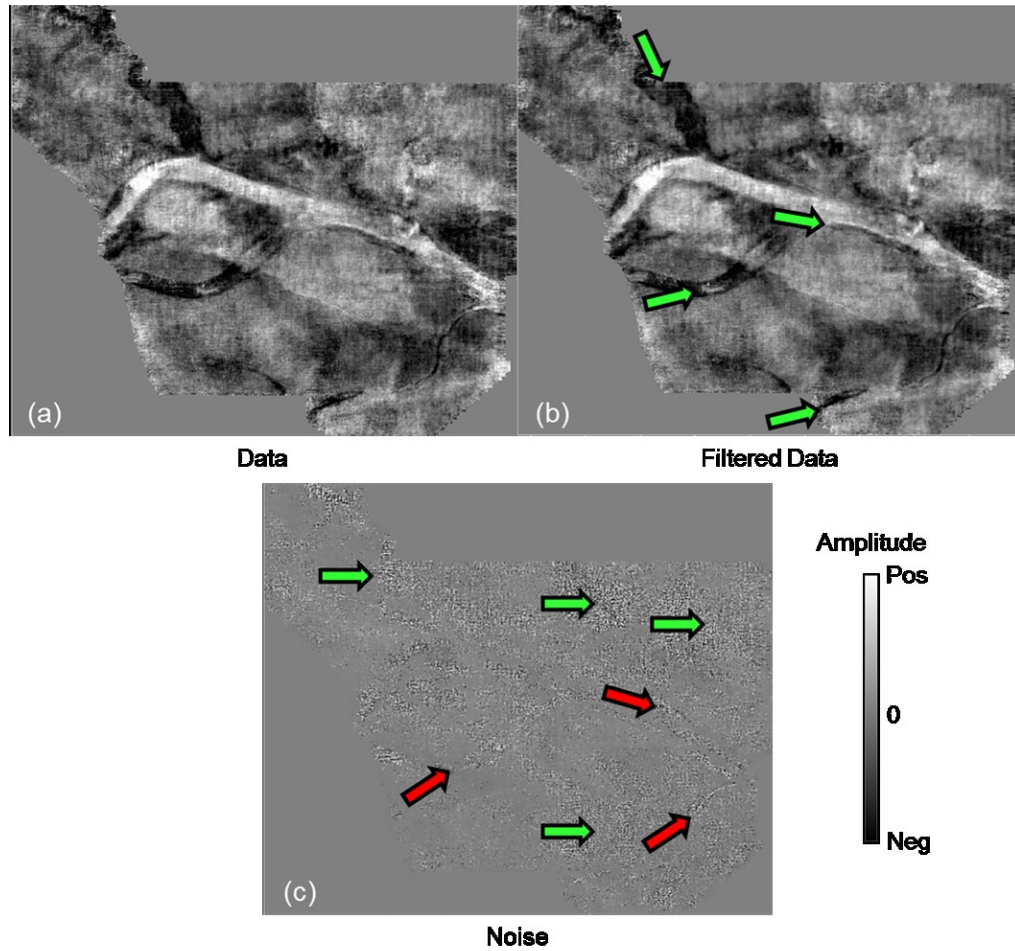


Figure 32: Phantom horizon slice 0.066 s below the Skinner horizon (Figure 9) through (a) original seismic amplitude data, (b) horizon based principal component filtered seismic amplitude data and (c) removed noise for the dataset acquired in the Anadarko Basin, OK. The filter was designed using the first three principal components of the data in a 21-trace by 21-trace running analysis window. Footprint is attenuated in the filtered data (green arrows) but still present. The lack of footprint removal from the principal component filter is due to the consistent character of its waveform through the data. Note on the noise slice that random patterns of footprint are removed but also an equal amount of signal (red arrows).

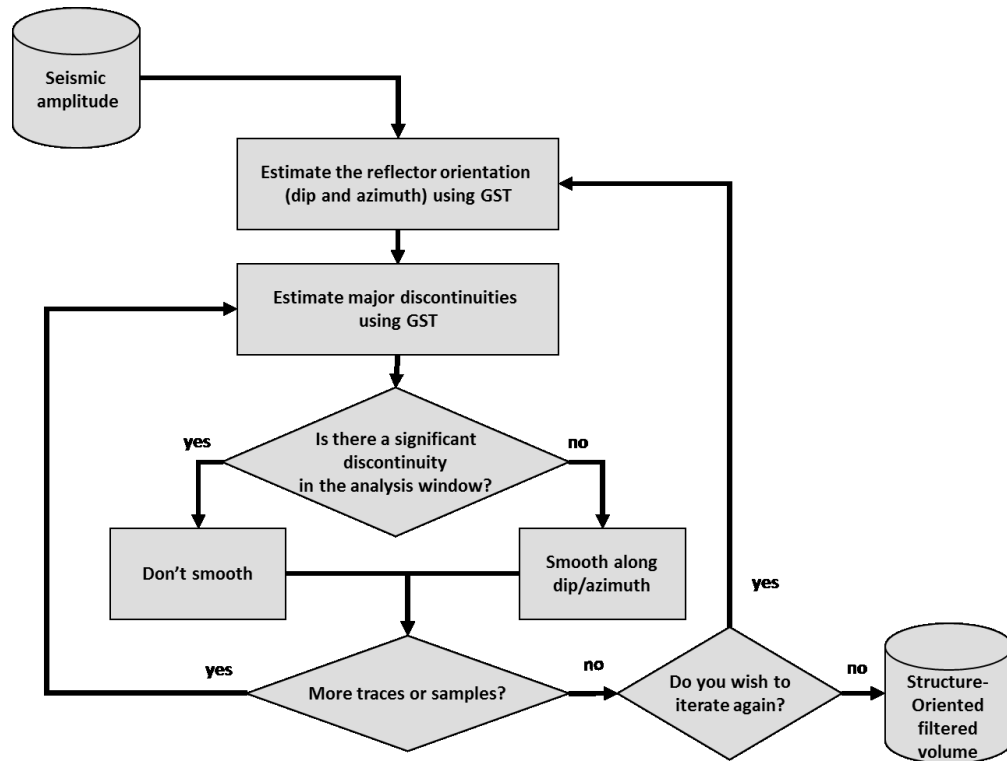


Figure 33: Fehmers and Höecker’s (2003) structure-oriented filtering workflow where the degree of smoothing is a function of the strength of the measured discontinuities. Their original algorithm computed d_i , azimuth, and discontinuities using a gradient structure tensor (GST). In the actual implementation there is a gradational blending between “smooth” and “don’t smooth”.

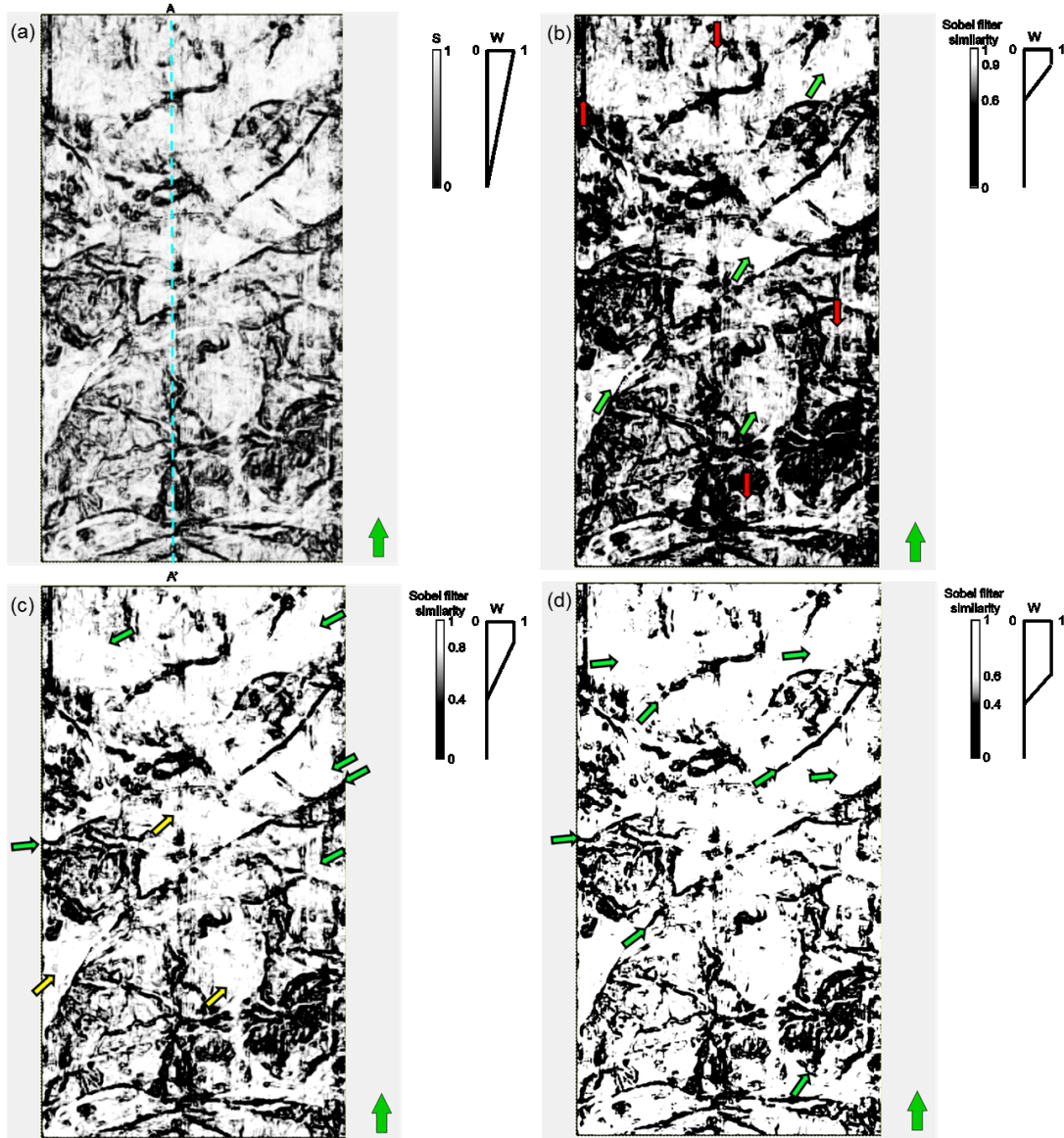


Figure 34: Suite of images illustrating the interactive workflow used to define smoothing weights in structure-oriented filtering for a time slice at $t=0.76$ s through the Sobel filter similarity data volume computed from the offshore Louisiana data set (Figure 12). (a) Similarity values, S , and corresponding weights, W . By modifying the threshold values for S we increase or decrease the smoothing weights thereby changing the aggressiveness of the filter. (b) Note the enhancement of the footprint noise (red arrows). Green arrows indicate white areas where the filter will be more aggressive and remove incoherent noise. (c) Yellow arrows indicate geologic features that will be partially or totally smoothed due to their similarity values S and corresponding weights W compared to (a). Green arrows indicate features that will be preserved or areas where footprint will be removed. (d) This case is the optimal setting for the degree of smoothing. Green arrows indicate key areas where (d) shows an improvement over (c) both in preserving lineaments and removing footprint.

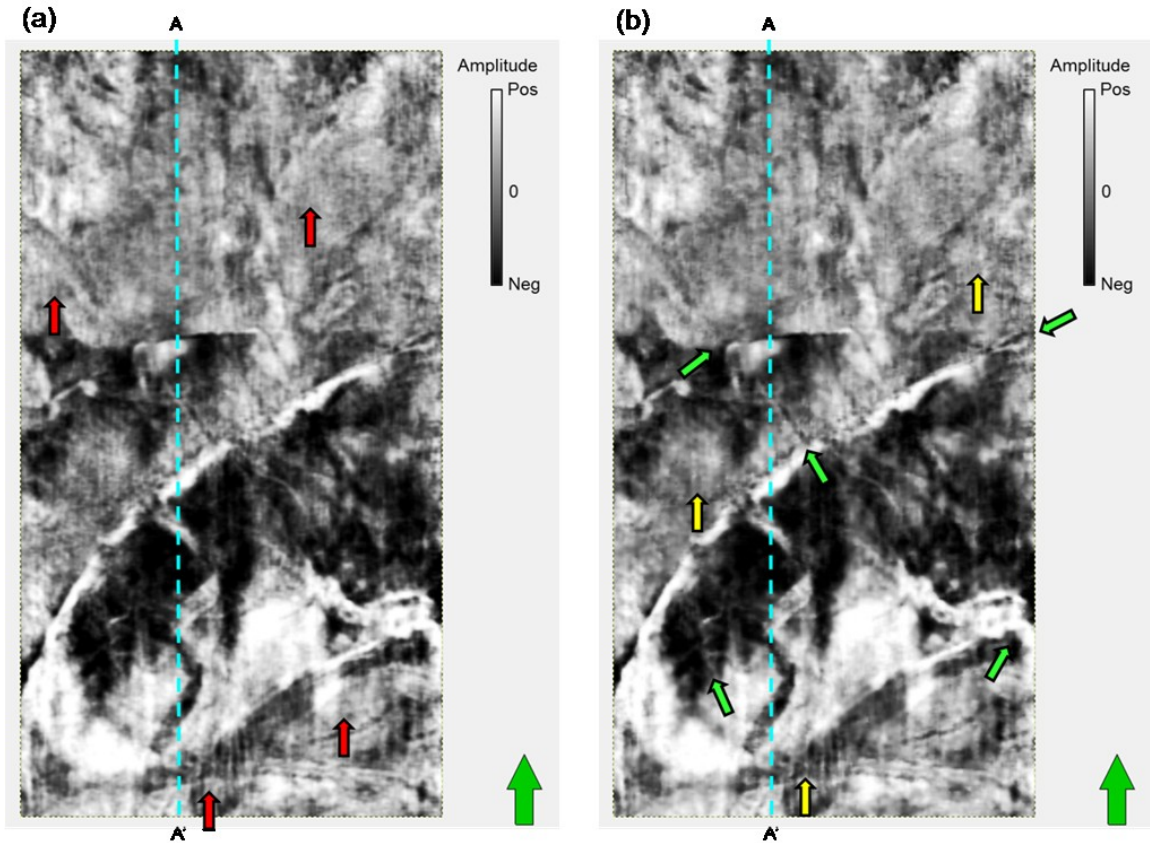


Figure 35: Time slice at $t=0.76$ s though (a) seismic amplitude and (b) output from a variation of Fehmers and Höecker's structure-oriented principal component algorithm for the offshore Louisiana data set. (a) Red arrows indicate footprint contamination. (b) The amplitude of the footprint was diminished by the filter but there are still remnants visible after first iteration (yellow arrows). Green arrows indicate areas where edges of geologic features are sharper.

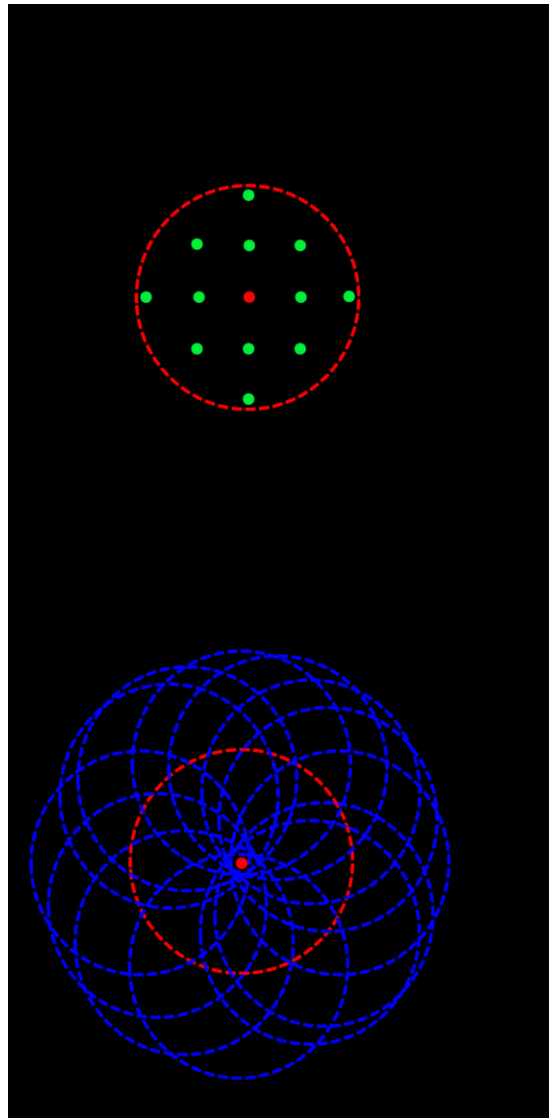


Figure 36: (a) An analysis window centered about an analysis point indicated by the red solid dot containing a total of 13 traces (red and green dots). (b) A suite of 13 overlapping windows centered about the green dots in (a), each of which also contains 13 traces, including the analysis point indicated by the red dot. The coherence along dip and azimuth is computed in each window and used in the flow described in Figure 37. Use of such laterally shifted windows helps avoid smoothing across faults, angular unconformities and other features of geologic interest when compared to (a).

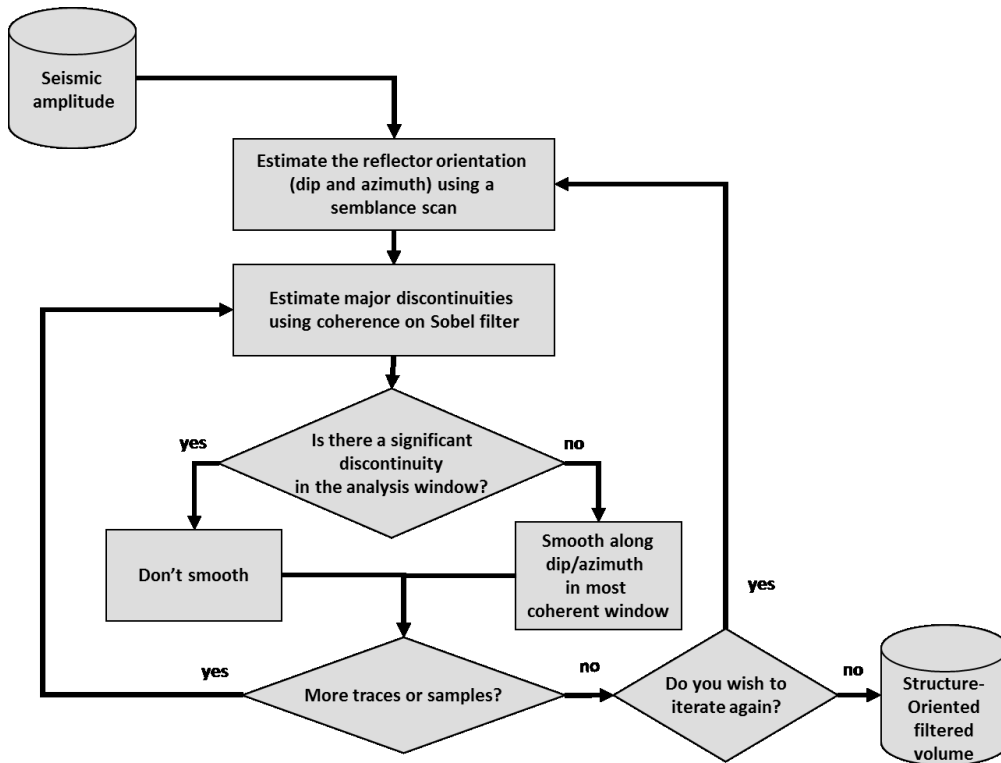


Figure 37: Structure oriented filtering workflow using a modification of the Kuwahara algorithm for dip estimates after Marfurt (2006).

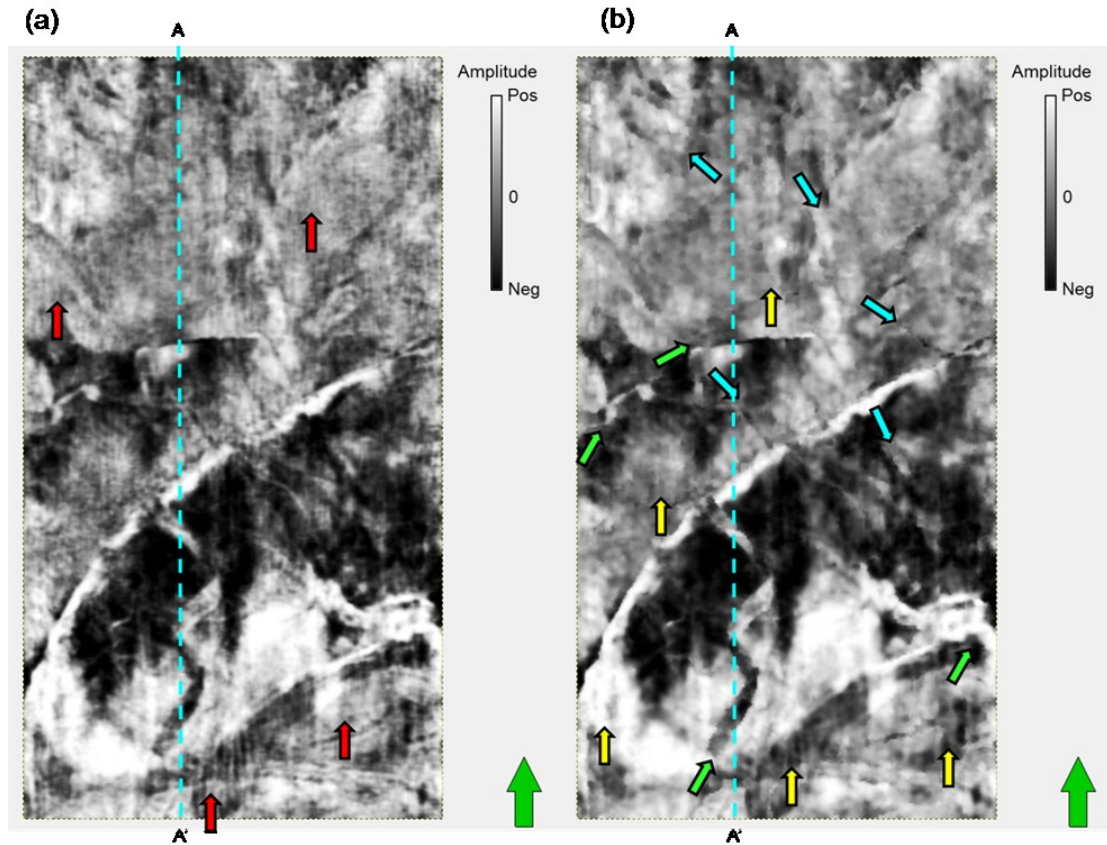


Figure 38: Time slice at $t=0.76$ s through (a) seismic amplitude and (b) principal component filtered seismic amplitude following the workflow in Figure 37 for the offshore Louisiana data set. (a) Red arrows indicate footprint contamination. The amplitude of the footprint was diminished and smeared by the filter but there are still remnants visible in (b) (yellow arrows). Green arrows indicate areas where edges of geologic features are sharper. Cyan arrows indicate features that became distinguishable after the filtering. Line AA' is shown in Figure 39.

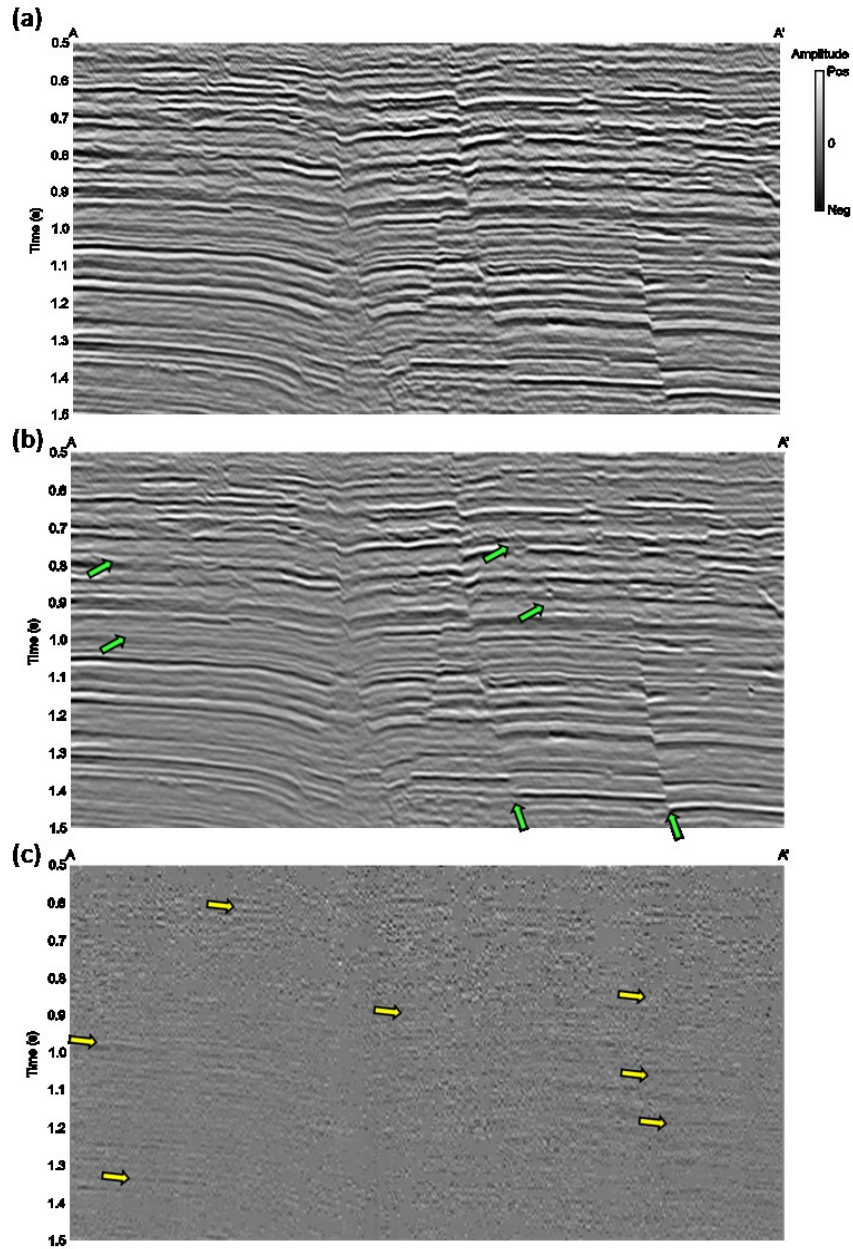


Figure 39: Vertical section through line AA' shown in Figure 38 for the offshore Louisiana dataset showing (a) original data, (b) filtered data and (c) noise respectively. The data was filtered using modified Fehmers and Höecker's workflow (Figure 33) using a single analysis window containing 13 traces. Fehmers and Höecker's technique shows effective for removing footprint modulation through the entire section (green arrows) but removes also a fair amount of signal (yellow arrows).

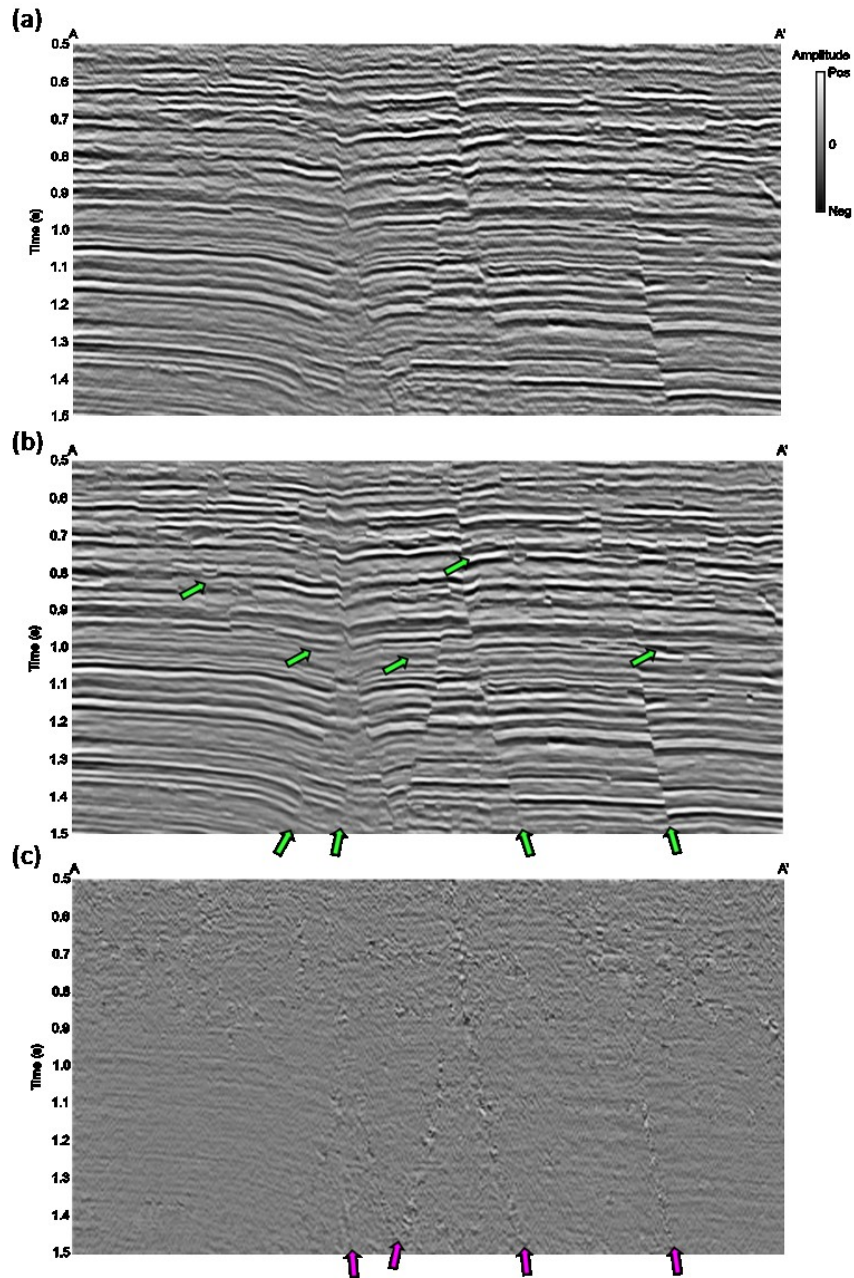
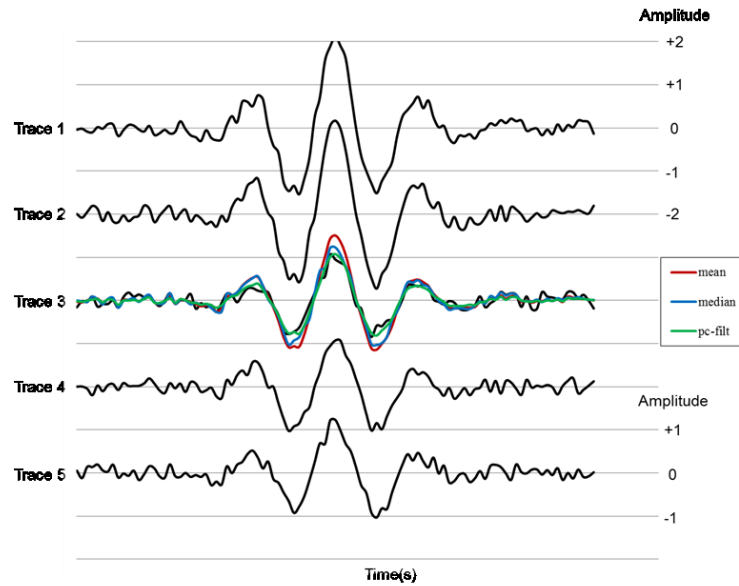


Figure 40: Vertical section through line AA' shown in Figure 38 for the offshore Louisiana dataset showing (a) original data, (b) filtered data and (c) noise respectively. The data was filtered using modified Kuwahara window workflow (Figure 37) using a suite of 13 overlapping windows each of which contains 13 traces. The Kuwahara technique also does a good job in removing the footprint modulation through the entire section (green arrows) and also removes fault plane reflections (magenta arrows). An improvement in the reflector coherence due to Kuwahara's overlapping window technique is observed. Examples in Figure 39 and Figure 40 used only one iteration and the same edge-preservation criteria and weights (Figure 34c)

(a)



(b)

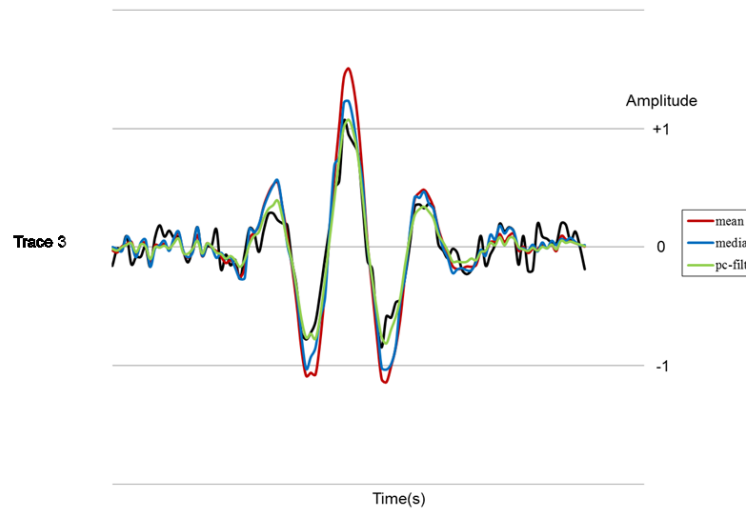


Figure 41: (a) Five noise contaminated traces. Note traces 1 and 2 have a peak amplitude of about 2.0 while traces 3-5 have a peak amplitude of about 1.0. (b) Detail of center trace 3 showing the results of mean, median, and principal component filtering. The mean and median filters both overestimate the amplitude, while the PC-filter both diminishes random noise and approximates the underlying true signal amplitude. The PC filter does this by using 55 data values (5 traces by 11 time samples) in the filter design, while the mean and median filters are based only 5 data values (5 traces at a single time sample).

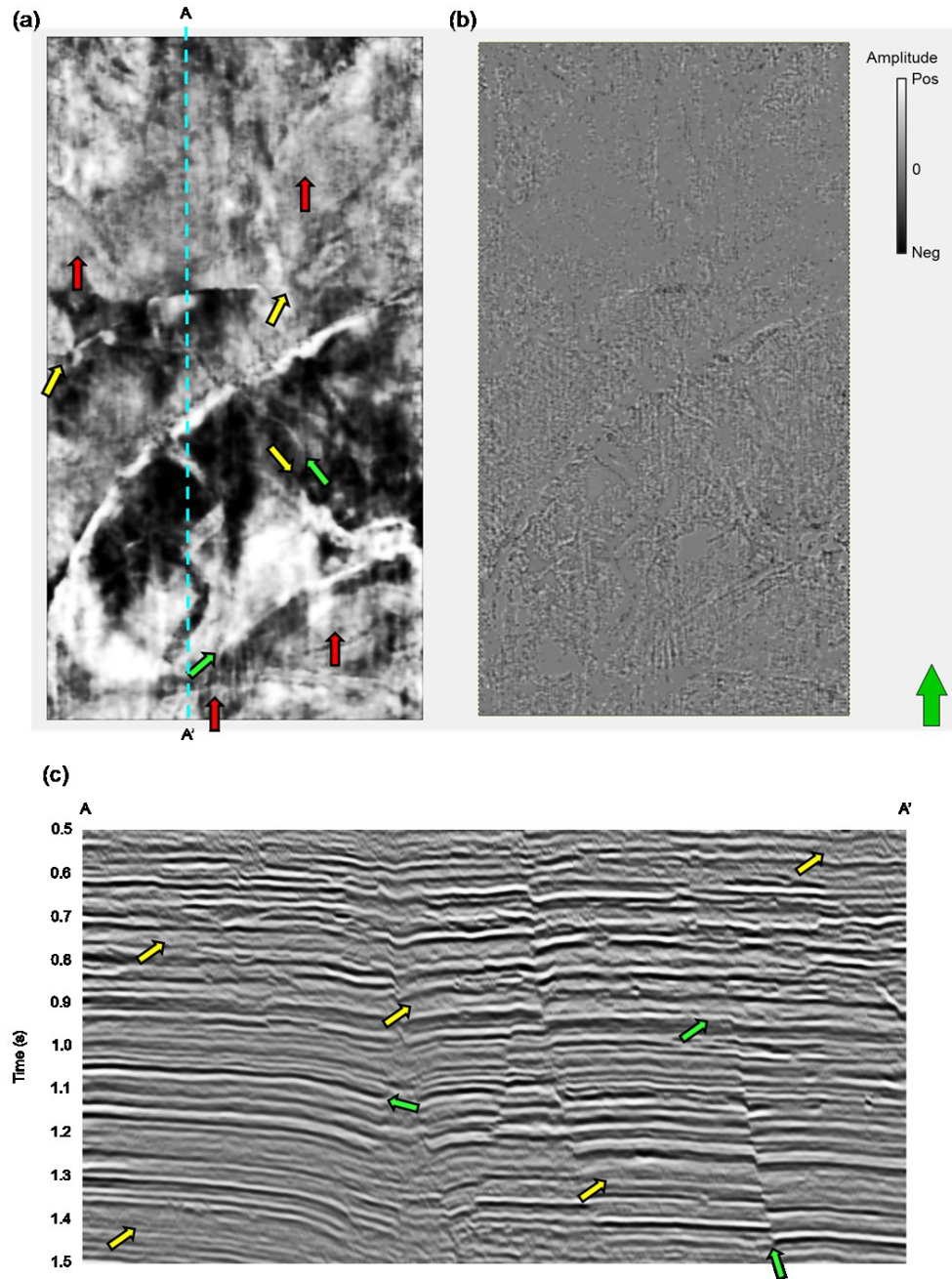


Figure 42: (a) Time slice at $t=0.76$ s though mean-filtered seismic amplitude using the workflow shown in Figure 37. (b) Difference between original data (Figure 35a) and (a). (c) Vertical section through mean filtered seismic amplitude for line A-A' shown in (a). Red arrows indicate footprint contamination, yellow arrows indicate features that have enhancement after filtering but are still damaged by the footprint. Green arrows indicate features that have been improved after filtering. (b) Most of the removed amplitudes correspond to footprint modulation. Note that some signal has been removed also by the filtering process. (c) Green arrows indicate areas where filtering has improved reflector continuity. Yellow arrows indicate areas that are still damaged by the footprint.

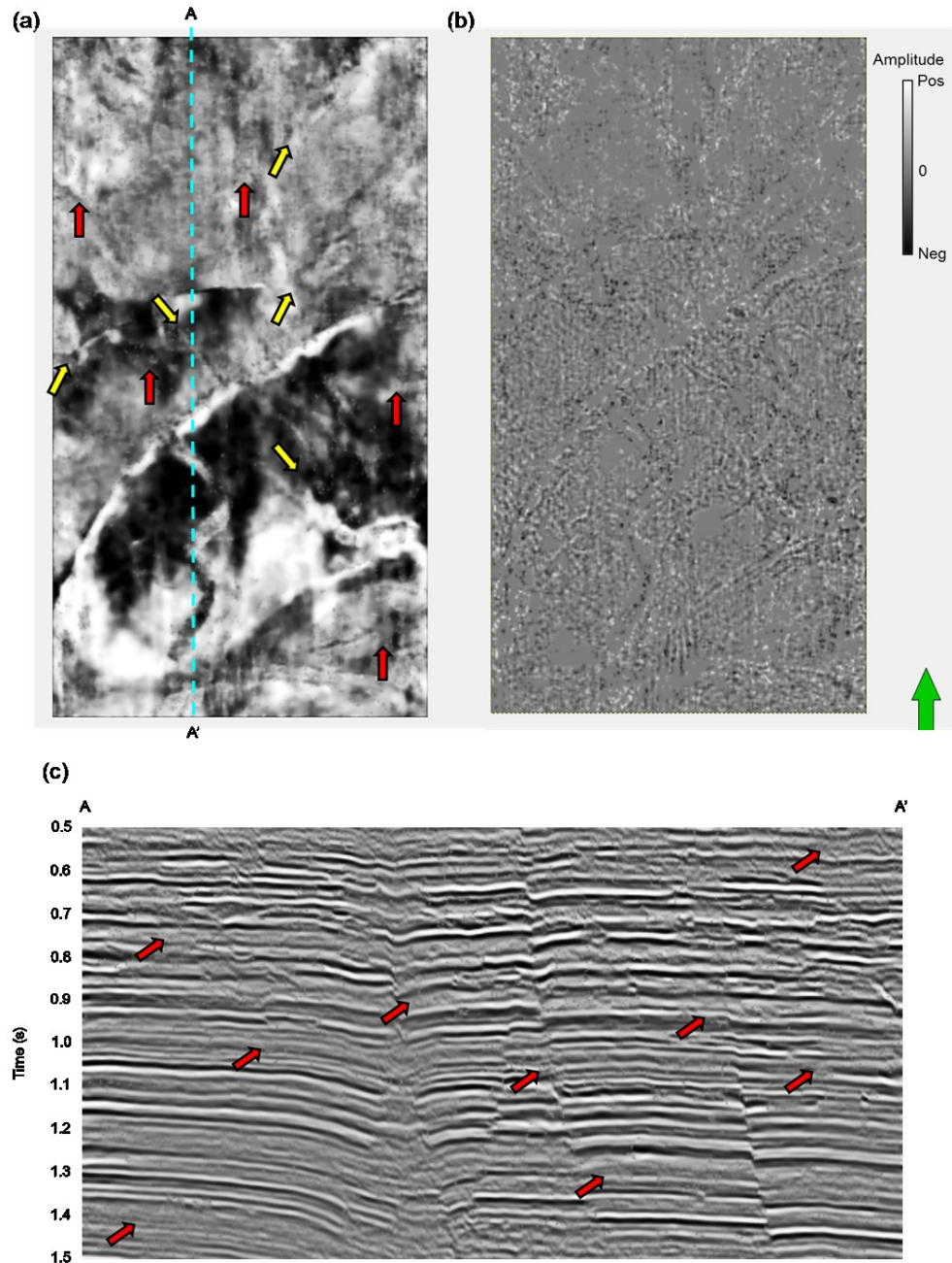


Figure 43: (a) Time slice at $t=0.76$ s through median-filtered seismic amplitude using workflow shown in Figure 37. (b) Difference between original data (Figure 35a) and (a). (c) Vertical section through median-filtered seismic amplitude for line A-A' shown in (a). (a) Red arrows indicate footprint contamination, yellow arrows indicate features that have enhancement after filtering but still damaged by the footprint. (b) Most of the removed amplitudes correspond to footprint modulation. Note that more signal has been removed when compared to Figure 42b. (c) Median filter is not as effective as the mean filter in removing the footprint. Red arrows indicate areas where a strong footprint contamination is observed.

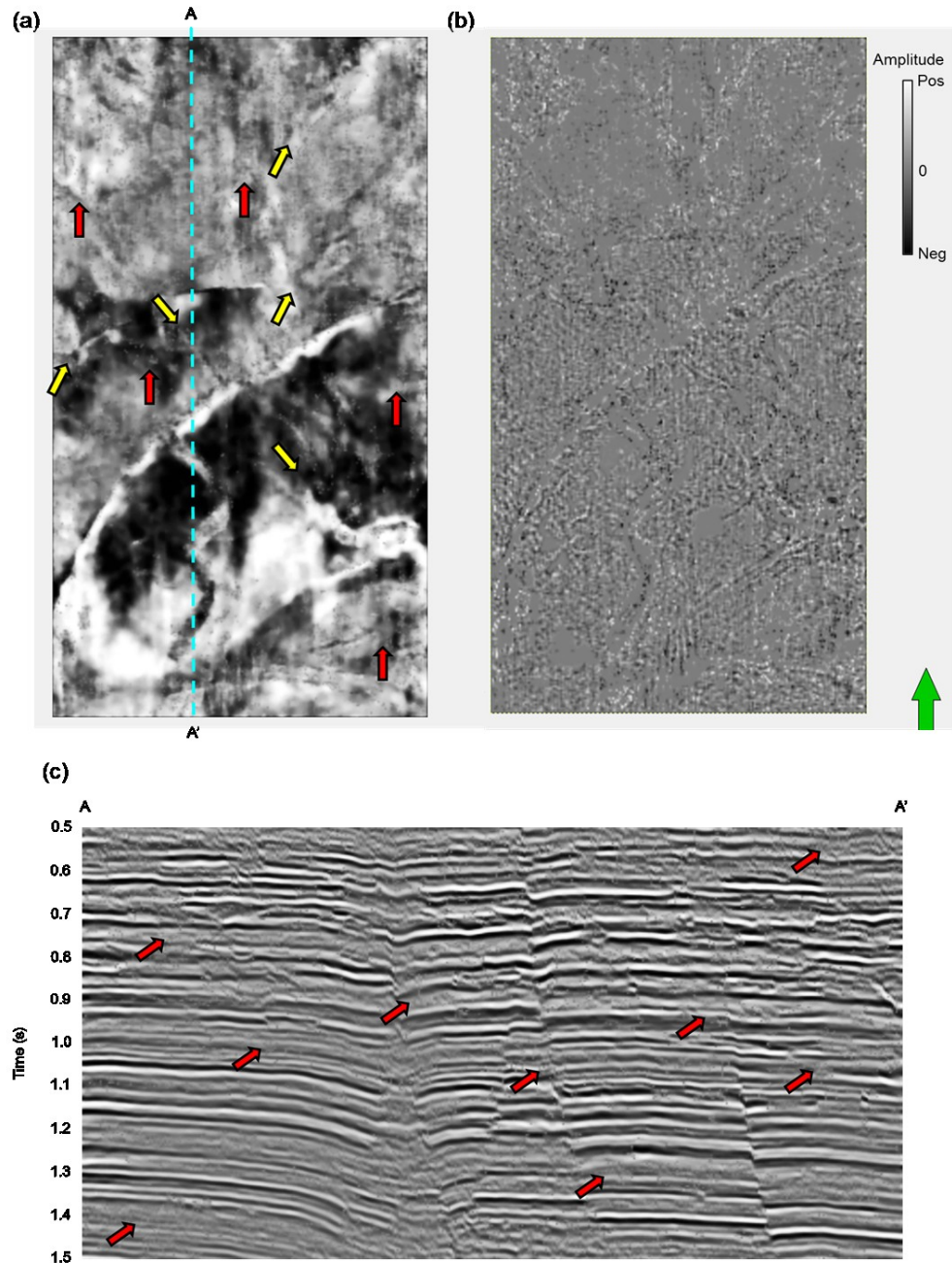


Figure 44: (a) Time slice at $t=0.76$ s through 20% α -trimmed mean filtered seismic amplitude using workflow shown in Figure 37. (b) Difference between original data (Figure 35a) and (a). (c) Vertical section through α -trimmed mean filtered seismic amplitude for line A-A' shown in (a). For this particular case the results of the α -trimmed mean filtered data are very similar to the median filter.

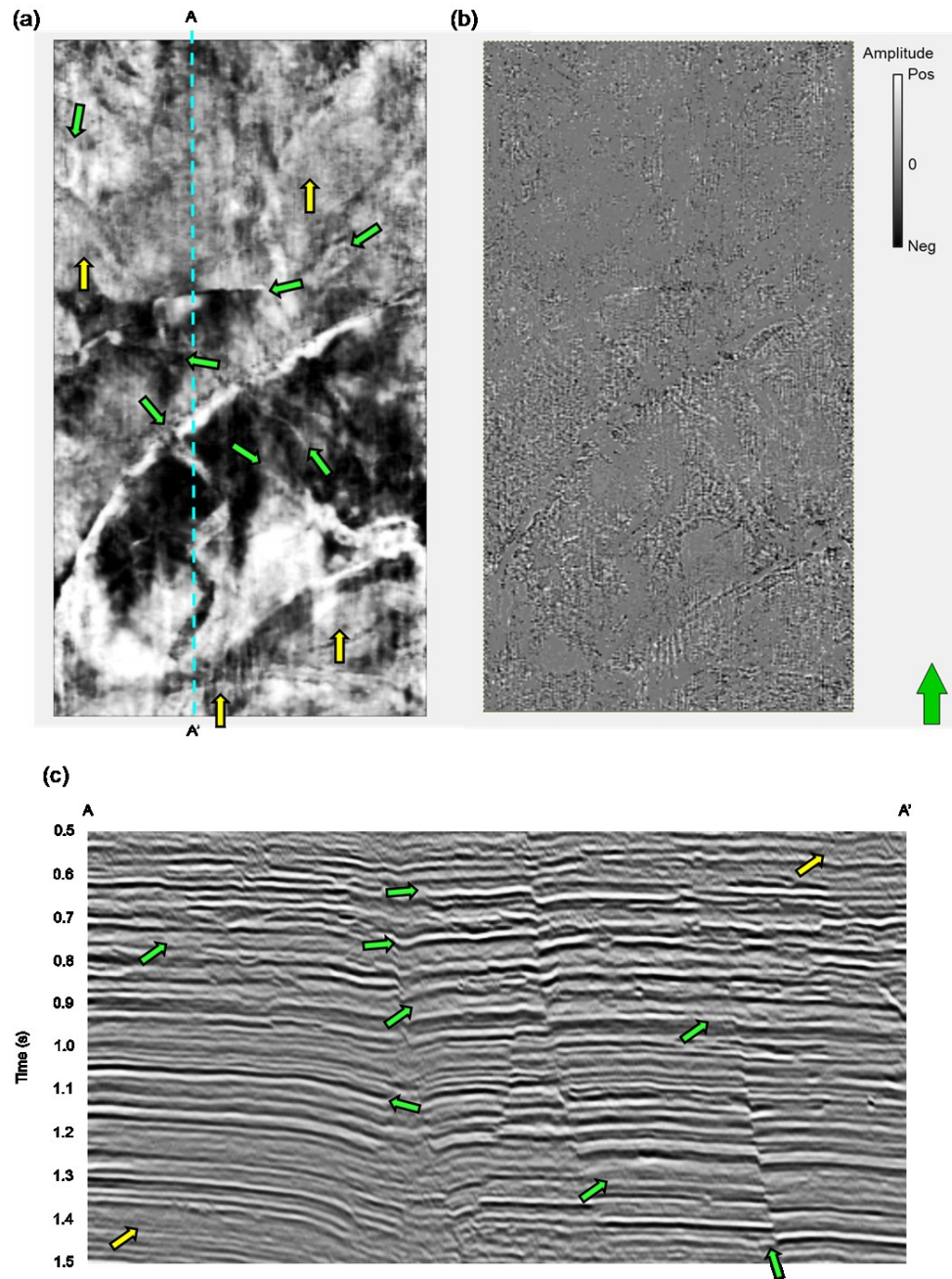


Figure 45: (a) Time slice at $t=0.76$ s through principal component filtered seismic amplitude using workflow shown in Figure 37. (b) Difference between original data (Figure 35a) and (a). (c) Vertical section through principal component filtered seismic amplitude for line A-A' shown in (a). (a) Yellow arrows indicate areas that where the footprint has not been removed completely. Green arrows indicate features that have been enhanced by filtering. (b) Compared to Figure 42 and Figure 43 principal component filtered better removes footprint modulation. Note that almost no signal was removed from the original data. (c) Green arrows indicate areas where reflector continuity has been greatly enhanced by filtering. Yellow arrows indicate areas where footprint still present.

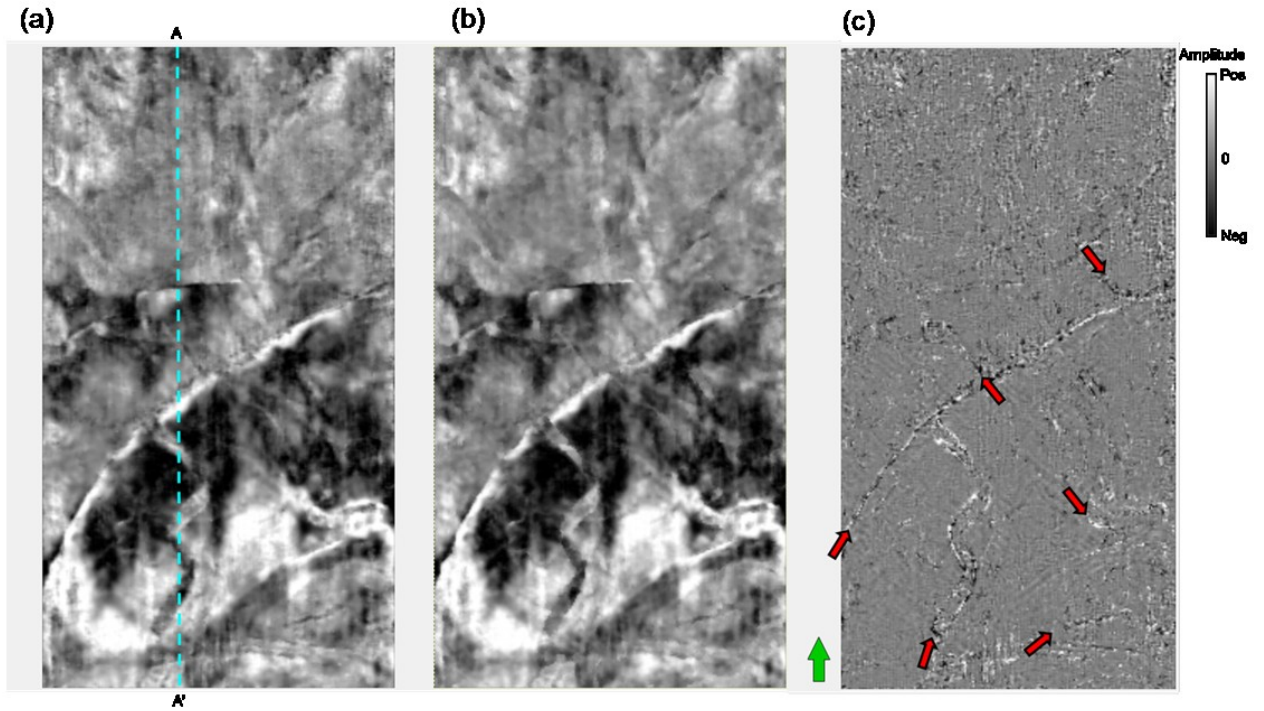


Figure 46: Time slice at $t=0.76$ s through (a) principal component filtered seismic amplitude (Figure 37) using the first eigenmap, (b) principal component filtered seismic amplitude (Figure 37) using the second eigenmap and (c) difference between (a) and (b). Lineaments edges are sharper and better defined in (b) with respect to (a). (c) Red arrows indicate subtle features and edges present in (b) that are removed in (a) by the filtering process.

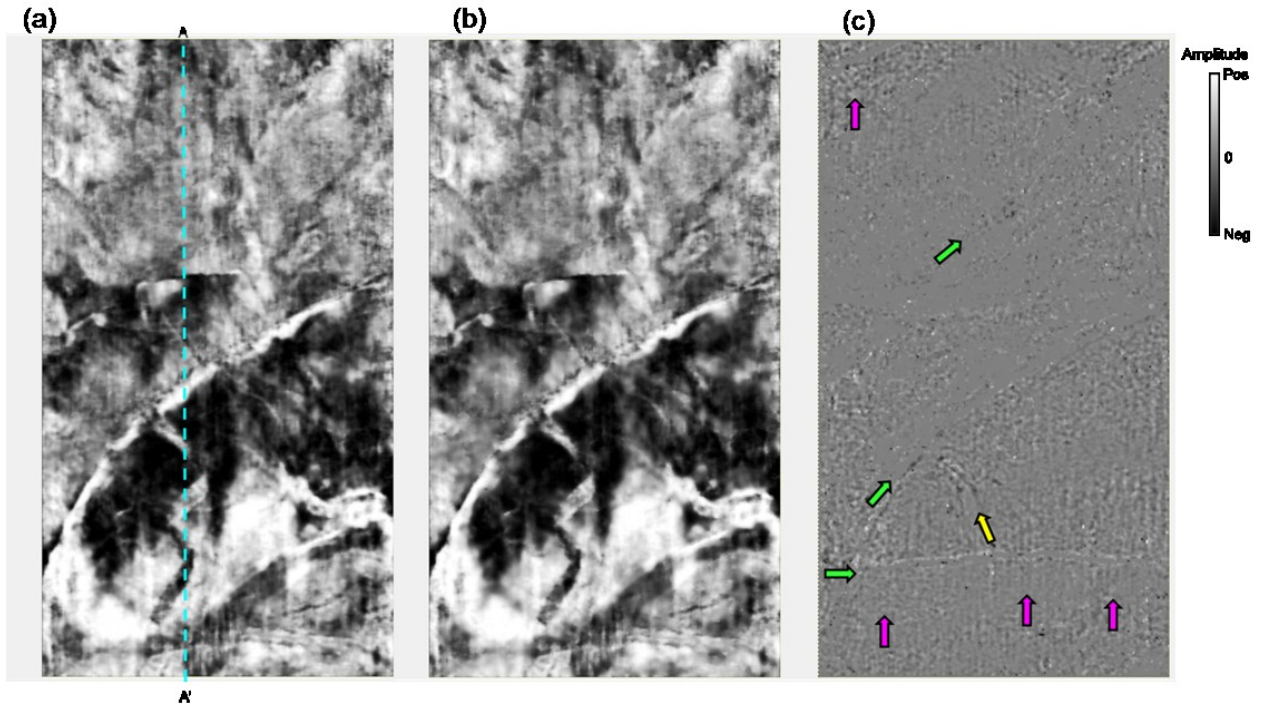


Figure 47: Time slice at $t=0.76$ s though (a) principal component filtered seismic amplitude (Figure 37) using a horizontal analysis window radius of 25 m containing 5 traces, (b) principal component filtered seismic amplitude (Figure 37) using a horizontal analysis window radius of 50 m containing 13 traces and (c) difference between (a) and (b). (c) For this case principal component filtering with a larger horizontal window shows more effective in removing footprint noise (magenta arrows). Notice that large discontinuity features are not harmed by a larger window (green arrows) although small geologic features could be harmed when using a larger horizontal analysis window (yellow arrow)

CHAPTER V

Alternative workflow examples

Although interpreters would wish for a single filter that would remove all the noise in the data in a single pass, this is rarely the case. A single perfect filter does not exist but the combination of different filters often serves as a very good approximation to a “perfect” filter. I have designed data dependent workflows combining structural oriented filters and horizon based k_x - k_y filters depending on the acquisition footprint response on attributes.

Figure 48 shows the cascaded filtering workflow for removing acquisition footprint characterized with structural curvature attributes. Figure 49 and Figure 50 show results of seismic amplitude and most positive principal structural curvature for the data acquired over the Delaware Basin, NM filtered using the workflow shown in Figure 48.

Figure 51 shows the cascaded filtering workflow for removing acquisition footprint affecting frequency and wavelet phase attributes. Figure 52 and Figure 53 show the improvements of peak frequency modulated by peak magnitude attribute and peak wavelet phase modulated by peak magnitude attribute for the seismic data acquired over the Anadarko Basin, OK. Figure 54 shows the impact of filtering for relative acoustic impedance calculation for the same data set.

Figure 55 shows the cascaded filtering workflow for removing acquisition footprint affecting similarity attributes. Figure 56 and Figure 57 show the improvements of Sobel filter similarity attribute for seismic data acquired over Central Basin Platform, TX.

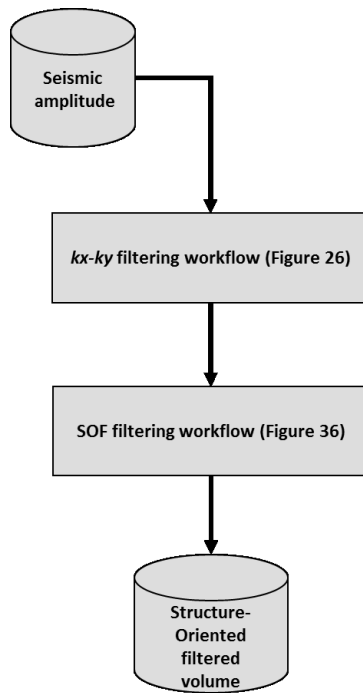


Figure 48: Workflow implemented for removing footprint contamination of structural curvature attributes

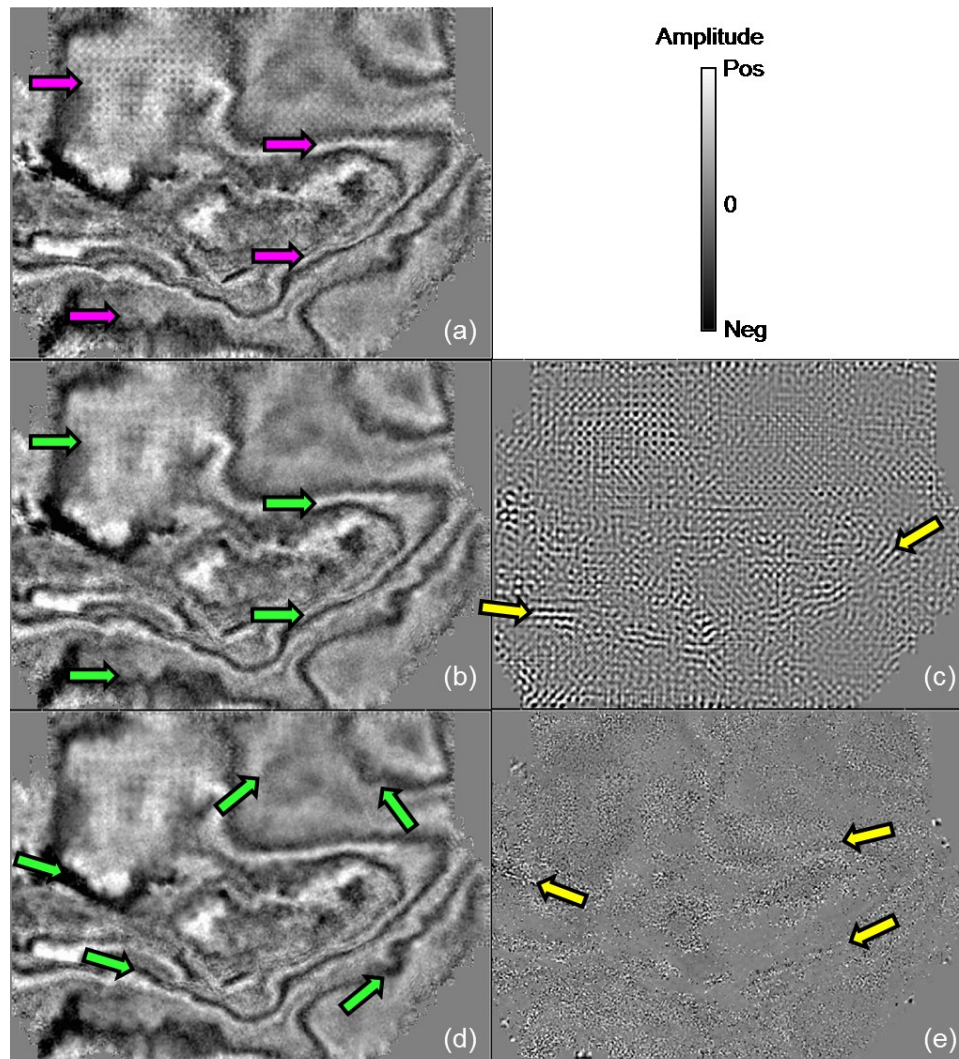


Figure 49: Time slice at $t=0.8$ s through the (a) original seismic amplitude data, (b) k_x - k_y filtered seismic amplitude data, (c) difference between (a) and (b), (d) principal component filtered data from (b) and (e) difference between (b) and (d) for the dataset acquired in the Delaware Basin, NM using the workflow shown in Figure 48. (a) Magenta arrows indicate areas where the footprint contamination is strongest. (b) k_x - k_y filter was implemented using most positive structural curvature following the workflow in Figure 26. Green arrows indicate areas where the footprint was successfully removed after k_x - k_y filtering. (c) Some steeply dipping reflectors were attenuated by k_x - k_y filtering (yellow arrows). (d) Principal component filter was implemented using a 220 ft horizontal window containing 13 traces, a 0.01 s vertical window containing 5 samples and the first three principal components following the workflow in Figure 37. Green arrows indicate areas of improvement compared to the k_x - k_y filtered data. (d) Yellow arrows indicate subtle geologic features removed by the principal component filtering process.

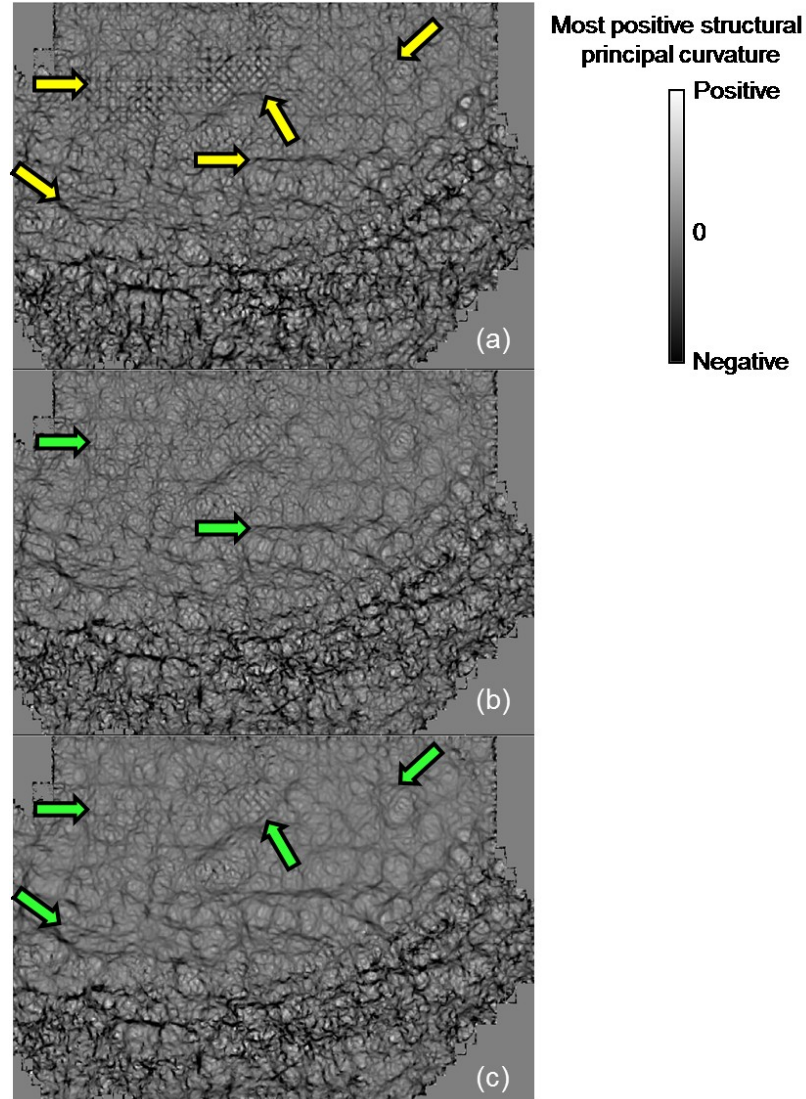


Figure 50: Time slice at $t=0.8$ s through the (a) most positive structural principal curvature calculated from original seismic data, (b) most positive structural principal curvature calculated from k_x - k_y filtered seismic amplitude data, (c) and most positive structural principal curvature calculated from principal component filtered for the dataset acquired in the Delaware Basin. (a) Yellow arrows indicate areas where the footprint contamination is strongest. (b) Green arrows indicate areas where curvature attribute has improved after k_x - k_y filtering. (c) Green arrows indicate areas where the combination of k_x - k_y filtering and principal component structure-oriented filtering has improved subtle geologic features.

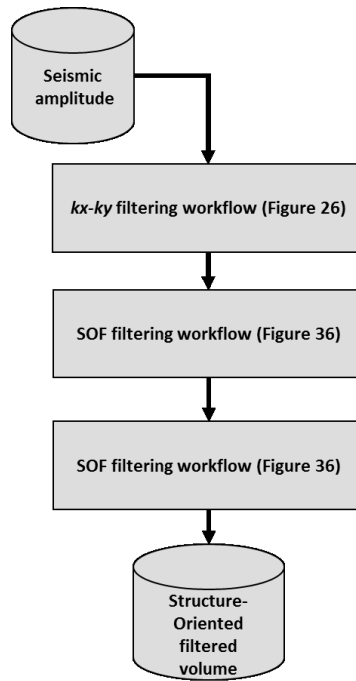


Figure 51: Workflow implemented for removing footprint contamination of frequency, phase and impedance inversion. Note there are two iterations of SOF following k_x - k_y filtering.

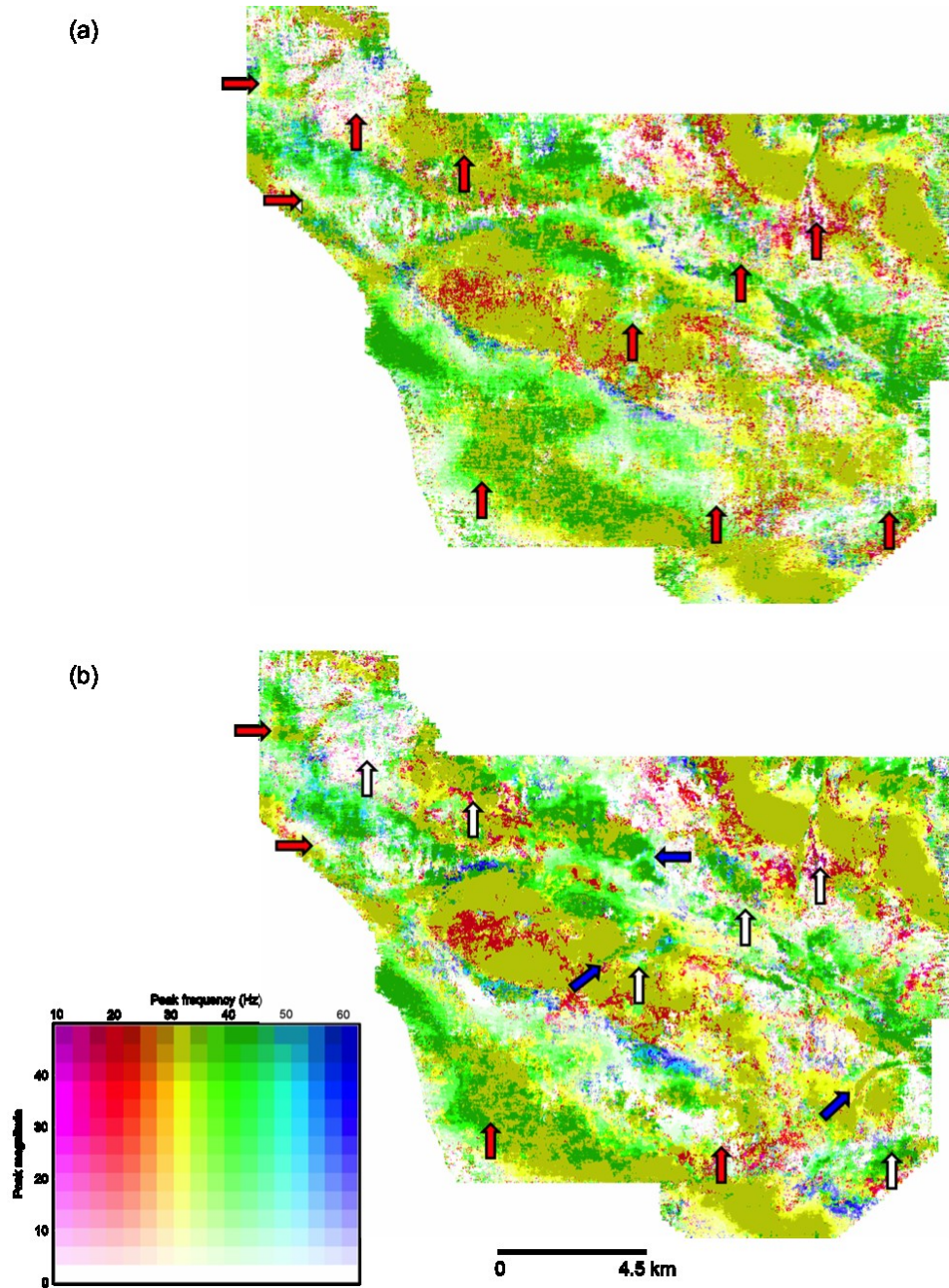


Figure 52: Phantom horizon slice 0.066 s below the Skinner horizon through (a) peak frequency modulated by peak magnitude using a 2D color map (Guou et al, 2008) computed from seismic amplitude volume acquired over the Anadarko Basin, OK. (b) Peak frequency modulated by peak amplitude using a 2D color map (Guo et al, 2008) computed from filtered seismic amplitude volume following workflow in Figure 51. Red arrows indicate acquisition footprint artifacts with a predominant frequency of 30 Hz. White arrows indicate enhanced features after the filtering process. Blue arrows indicate features that have become visible after filtering. Red arrows indicate areas still affected by acquisition footprint.

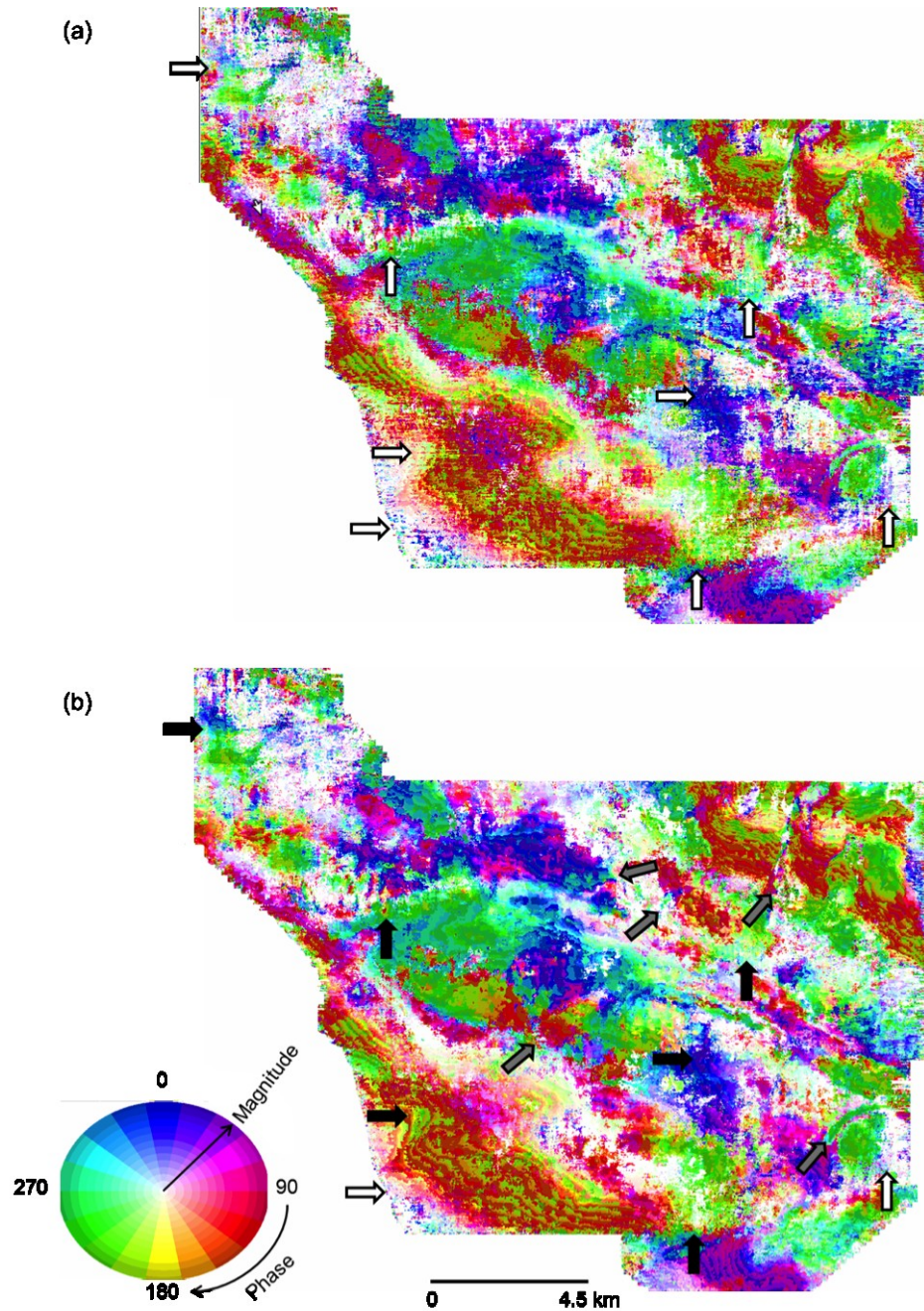


Figure 53: Phantom horizon slice 0.066 s below Skinner horizon trough (a) peak phase modulated by peak magnitude using a 2D color map (Guo et al, 2008) computed from seismic amplitude volume acquired over the Anadarko Basin, OK. (b) Peak frequency modulated by peak amplitude using a 2D color map (Guo et al, 2008) computed from filtered seismic amplitude volume following workflow in Figure 51. (a) White arrows indicate acquisition footprint artifacts. Black arrows indicate enhanced features after the filtering process. Grey arrows indicate features that have become visible after filtering.

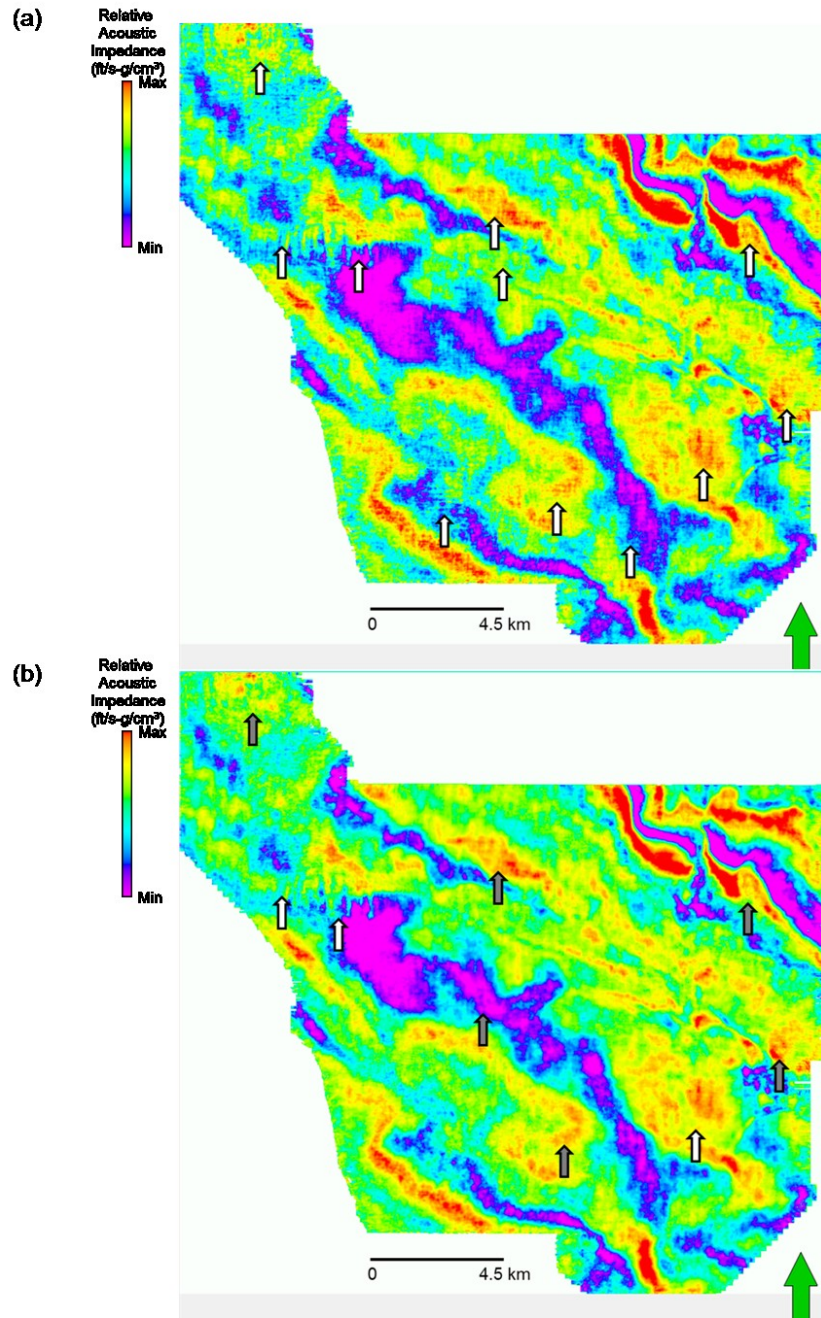


Figure 54: Time slice at $t=1.68$ s trough (a) relative acoustic impedance computed from seismic amplitude volume acquired over the Anadarko Basin, OK and (b) relative acoustic impedance data volume computed from filtered seismic amplitude volume using workflow in Figure 51. (a) White arrows indicate acquisition footprint artifacts. Artifacts appear as N-S trending impedance anomalies that mask impedance in the reservoir interval. (b) Grey arrows indicate areas where filtering has improved the resolution of the relative acoustic impedance. White arrows indicate areas still affected by footprint.

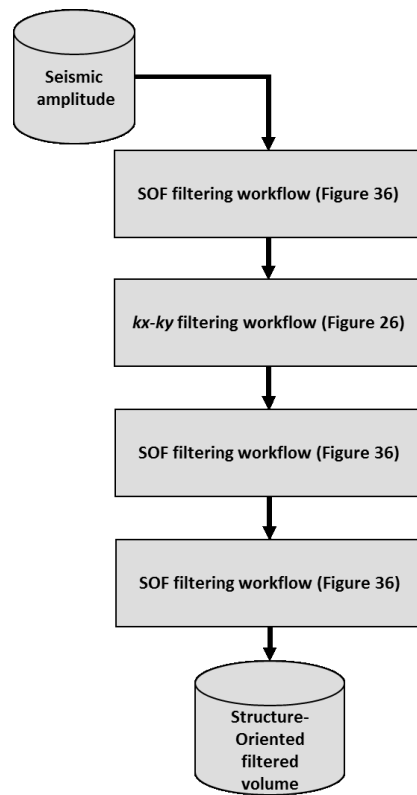


Figure 55: Workflow implemented for removing footprint contamination of similarity attributes. Note the k_x - k_y following the SOF filtering and the two iterations of SOF following k_x - k_y filtering.

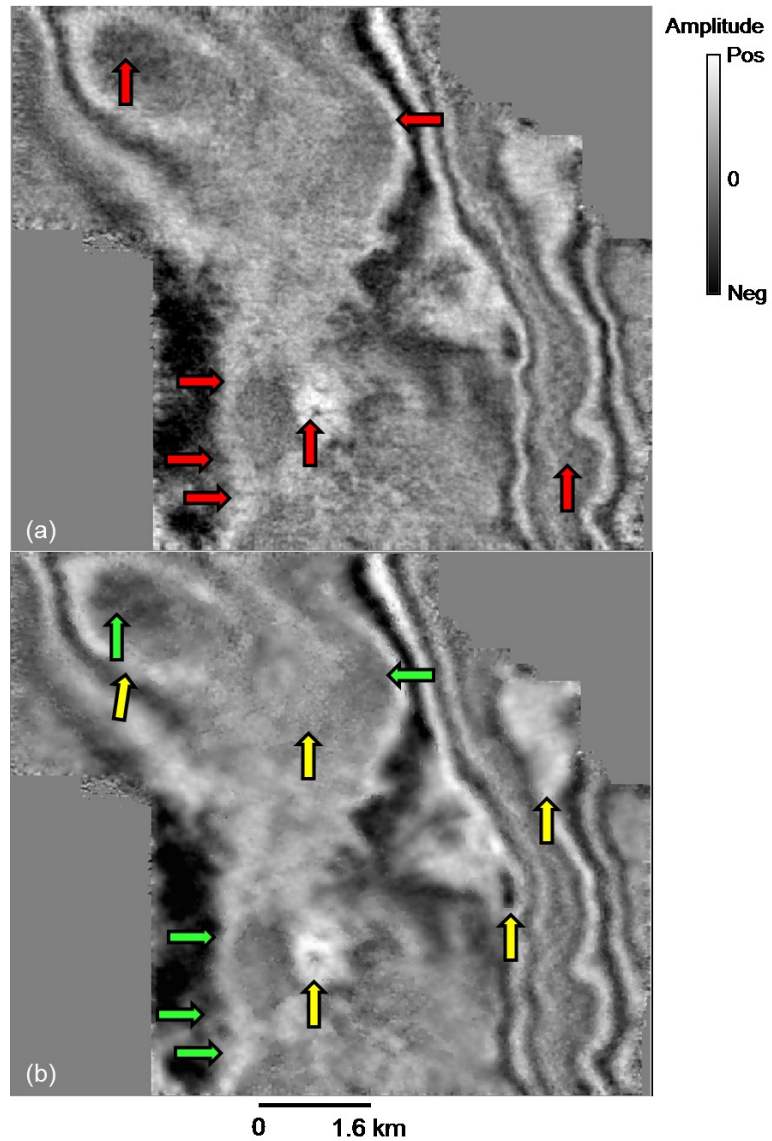


Figure 56: Time slice at $t=0.6$ s trough (a) original seismic amplitude and (b) filtered seismic amplitude following workflow shown in Figure 55 for seismic data acquired over Central Basin Platform, TX. Red arrows indicate footprint contamination. Green arrows indicate zones where filtering has enhanced the amplitude of geologic features. Yellow arrows indicate features that have been harmed as a consequence of filtering.

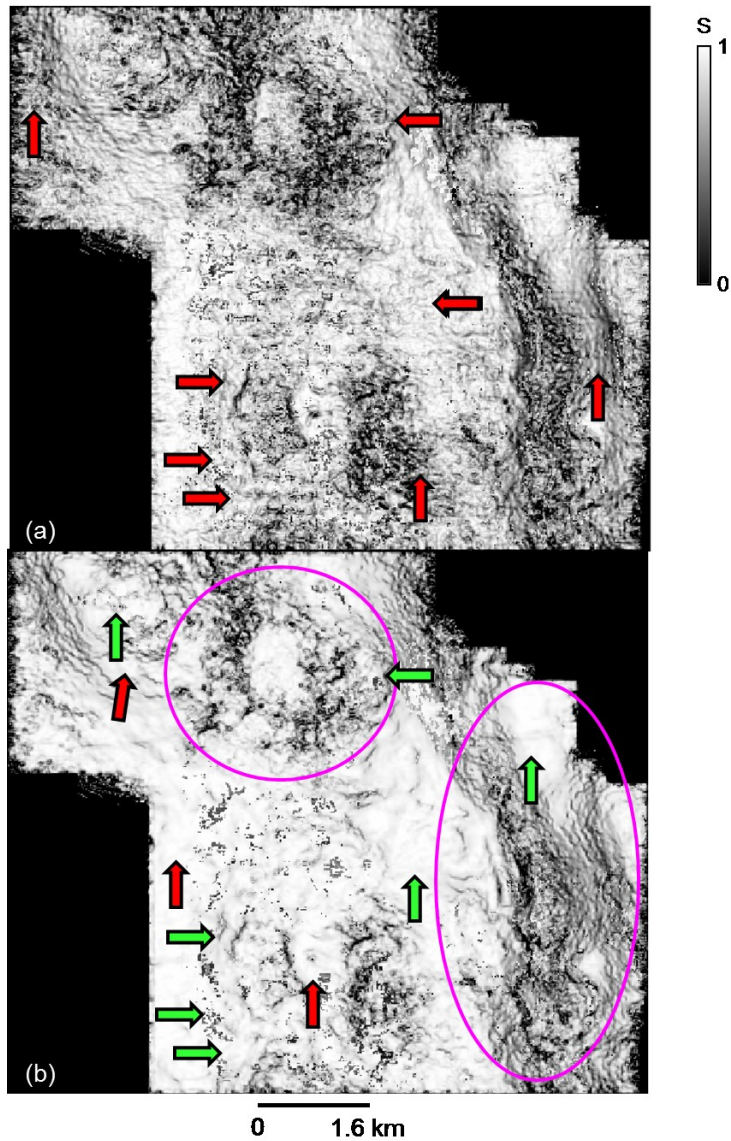


Figure 57: Time slice at $t=0.6$ s trough Sobel filter similarity computed from (a) original seismic amplitude and (b) filtered seismic amplitude following workflow shown in Figure 55 for seismic data acquired over Central Basin Platform, TX. (a) Red arrows indicate footprint contamination. (b) Green arrows indicate zones where filtering has enhanced the amplitude of geologic features. Red arrows indicate features that have been harmed as a consequence of filtering. Circled areas are subject to karsting at the San Andres level.

CONCLUSIONS

Acquisition footprint is present in all types of seismic data, and is most commonly due to the inadequate sampling of the seismic wave fields, inaccurate velocities and improperly muting the seismic data. Seismic attributes derived from footprint-contaminated data will enhance the acquisition footprint and appear as coherent spatially periodic artifacts overprint and often mask the geologic features of interest. Several authors have proposed alternative solution techniques for removing acquisition footprint. In this work we have approximated their implementations in order to evaluate their effectiveness on diverse data volumes as well as to provide additional clarification on their implementation.

For the migrated volumes evaluated, horizon-based filtering techniques produce better result overall for acquisition footprint suppression since they rely on the interpreter's ability to recognize the footprint pattern and enhance it with attributes. On the other hand horizon-based techniques can also remove subtle features such as channel edges and faults if filter implementation is too aggressive.

Structure-oriented filters, SOF, are more local, can be effective in removing footprint anomalies and avoid the need to pick horizons. Cascaded SOF are best implemented by recomputing and imaging processing the dip before each iteration. In all cases the rejected "noise" should be inspected for signal components that were removed by the filter.

Although several solutions have been proposed to remove acquisition footprint from legacy data 3D data volumes, there is not a unique solution. However, the implementation of workflows that cascade structure-oriented with horizon based filters

has proven to be the most effective method to remove acquisition footprint from legacy data volumes (Table 1).

Table 1: Summary matrix of observed acquisition footprint examples and solution techniques.

Diagnostic	Problem	Proceeding	Results QC
Acquisition footprint contamination on structural curvature attributes	Acquisition footprint pattern overlaps seismic amplitudes masking subtle depositional features	Cascaded kx-ky-SOF filtering workflows recomputing similarity attributes in each step	Compare structural curvature and filtered seismic amplitudes attributes at each stage of the cascaded workflows with originals. Compute difference between original and filtered seismic
Acquisition footprint contamination of frequency, phase and impedance inversion attributes	Acquisition footprint changes in phase and amplitude affect frequency, phase and amplitude response of subtle geologic features	Cascaded kx-ky-SOF-SOF filtering workflows recomputing similarity attributes in each step	Compare amplitude curvature attributes at each stage of the cascaded workflows with originals. Compute difference between original and filtered seismic attributes at each step
Acquisition footprint contamination on Sobel filter discontinuity attributes	Acquisition footprint pattern has a similar response as Karst features	Cascaded SOF-kx-ky-SOF-SOF filtering workflows recomputing similarity attributes in each step	Compare similarity attributes at each stage of the cascaded workflows with originals. Compute difference between original and filtered seismic data at each step

REFERENCES

- Al-Bannagi, M., K. Fang, P. G. Kelamis, and G. S. Douglass, 2005, Acquisition footprint suppression via the truncated SVD technique: Case studies from Saudi Arabia: *The Leading Edge*, **24**, 832-834.
- Cabrales-Vargas, A., Suppression of aliasing artifacts on 3d land data via constrained least-squares migration: M.Sc. thesis, University of Oklahoma.
- Chopra, S. and K.J. Marfurt, 2008, Seismic Attributes for Prospect Identification and Reservoir Characterization, Geophysical Developments No.11, Society of Exploration Geophysicists.
- Drummond, J. M, J. L. A. Budd, and J. W. Ryan, 2000, Adapting to noisy 3D data—Attenuating the acquisition footprint: 70th Annual International Meeting, SEG, Expanded Abstracts, 9–12.
- Falconer, S., and K. J. Marfurt, 2006, Attribute-driven footprint suppression: SEG Expanded Abstracts, **27**, 2667-2671.
- Fehmers, G., F. W. Höecker, Fast structural interpretation with structure-oriented filtering: *Geophysics*, **68**, no. 4, 1286-1293.
- Finn, C. J., 1986, Estimation of three dimensional dip and curvature from reflection seismic data: M.Sc. thesis, University of Texas at Austin.
- Gülünay, N., 2000, 3D acquisition footprint removal: 62nd Annual International Conference and Exhibition: EAGE, Extended Abstracts, L0017.
- Guo, H., S. Lewis, and K. J. Marfurt, 2008, Mapping multiple attributes to three- and four-component color models - A tutorial: *Geophysics*, **73**, no. 3, W7–W19
- Hill, S., M. Shultz, and J. Brewer, 1999, Acquisition footprint and fold of stack plots: *The Leading Edge*, **18**, 686-695.
- Kirlin, R. L., W. J. Done, 1999, Covariance Analysis for Seismic Signal Processing, Geophysical Developments No.8, Society of Exploration Geophysicists.
- Kuwahara, M., K. Hachimura, S. Eiho, and M. Kinoshita, 1976, Digital processing of biomedical images: Plenum Press, 187–203.
- Luo, Y., S. al-Dossary, and M. Marhoon, 2002, Edge-preserving smoothing and applications: *The Leading Edge*, **21**, 136–158.
- Marfurt, K. J., 2006, Robust estimates of reflector dip and azimuth: *Geophysics*, **71**, 29–40.
- Spitz, S, 1999, Pattern recognition, spatial predictability, and subtraction of multiple events: *The Leading Edge*, **18**, 55-58.

APPENDIX

APPENDIX 1. REVIEW OF REFLECTOR DIP AND AZIMUTH ESTIMATOR

Dip and azimuth are commonly defined in reflection seismology to avoid mathematical ambiguities that arise by defining dip and strike in the geological sense. The reflector dip (θ) is identical to the geologic dip, and the reflector azimuth (ϕ) is defined as the direction of maximum downward dip (perpendicular to the geologic strike) measured from north. The reflector dip vector \mathbf{a} is defined by the apparent reflector dips θ_x and θ_y along the survey axes and the dip azimuth (Figure A1), where:

$$(A1)$$

$$(A2)$$

$$(A3)$$

When an accurate velocity model is not known, it is more convenient to measure the apparent dips in two-way time, where p is the inline apparent dip in s/m and q is the apparent crossline dip in s/m. By approximating the earth by a constant velocity model the apparent inline dip (p) and apparent crossline dip (q) can be defined as (Figure A1):

$$\text{—————} \quad (A4)$$

$$\text{—————} \quad (A5)$$

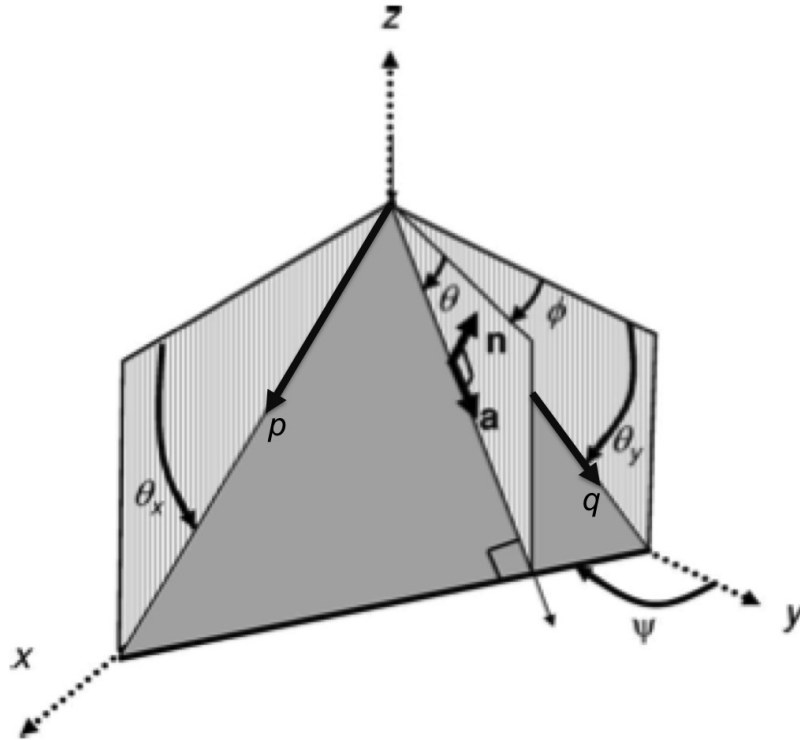


Figure A1: Mathematical, geological, and seismic nomenclature used in defining reflector dip: n is unit vector normal to the reflector, a is unit vector dip along the reflector, θ is dip magnitude, ϕ is dip azimuth, ψ is strike, θ_x is apparent dip in the xz plane, and θ_y is apparent dip in the yz plane. The apparent time dip in the xz plane is defined as vector p and the apparent time dip in the yz plane is vector q (Modified after Marfurt, 2006)

Marfurt et al. (1998) generalized Finn's (1986) method for semblance computation and analysis based on a 3D scanning analysis, to obtain more robust estimates of dip and azimuth. Using the data, u , and its Hilbert transform, u^H , minimizes artifacts encountered about zero crossings:

$$\frac{\sum_{j=1}^J \frac{u_j^H}{u_j} - \sum_{j=1}^J \frac{u_j}{u_j^H}}{\sum_{j=1}^J \frac{u_j^H}{u_j} + \sum_{j=1}^J \frac{u_j}{u_j^H}} \quad (\text{A6})$$

where p and q are defined by equation A2, x_j and y_j are the local coordinates for the j th trace measured from the origin to the analysis point; J denotes the total number of

traces in the analysis window and K_s and K_e denoted the first and last time sample in the analysis window (Figure A2).

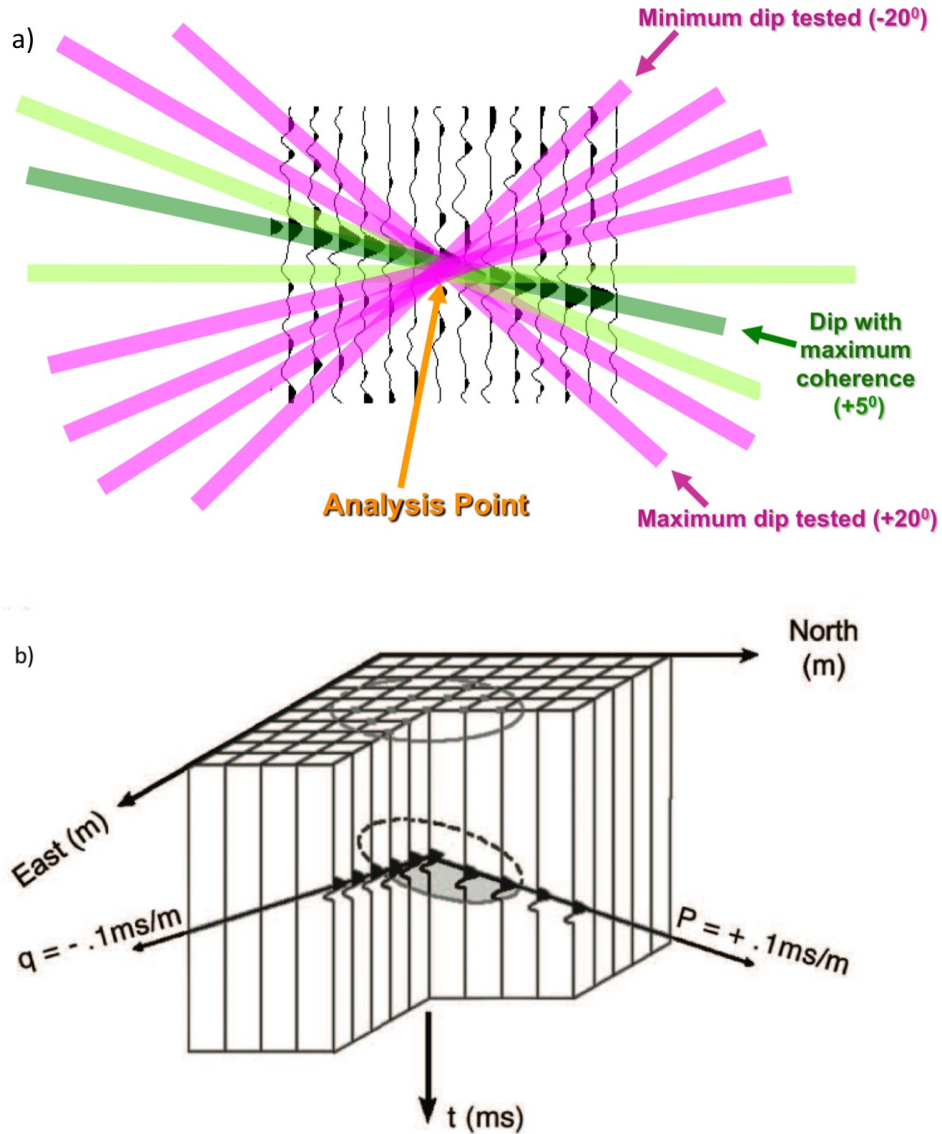


Figure A2: (a) Schematic showing the 2D dip coherence estimation. The first step is to calculate the coherence using some statistical measure (eg. Semblance or principal component), along several discrete dip candidates (shown in colored lines). The maximum coherence is shown in dark green. Next, the algorithm passes an interpolation curve through the coherence measures estimated by the peak value and two or more neighboring dips (here, shown in light green). The peak value of this curve gives an estimate of coherence, whereas the dip value of this peak gives an estimate of instantaneous dip. (b) A schematic diagram showing a 3D search-based estimate of coherence, in which p indicates the inline and q the

crossline components of vector time dip. The technique is analogous to that shown in (a). After Marfurt et al. (1998).

A better estimate of the reflector dip and azimuth is obtained by fitting a 2D paraboloid through the nine discretely sampled point neighboring the point having the maximum semblance:

$$(A7)$$

Solving for the α_j coefficients using a least-squares approximation, an improved estimation of the reflector dip can be calculated by solving for (θ, ϕ) :

$$\text{—————} \quad (A8)$$

$$\text{—————} \quad (A9)$$

Where (θ, ϕ) is the apparent dip pair corresponding to the maximum of the interpolated semblance surface.

Marfurt (2006) obtained a better estimate of vector dip using a multi-analysis window construct developed by Kuwahara et al. (1976), and adapted edge preserving amplitude filtering by Luo et al. (2002). The algorithm scans a suite of non-centered overlapping analysis windows in addition to the centered window, all of them containing the point of interest (Figure A3). Since amplitudes are expected to change along a discontinuity, semblance estimation is used to choose dip and window with the maximum coherence.

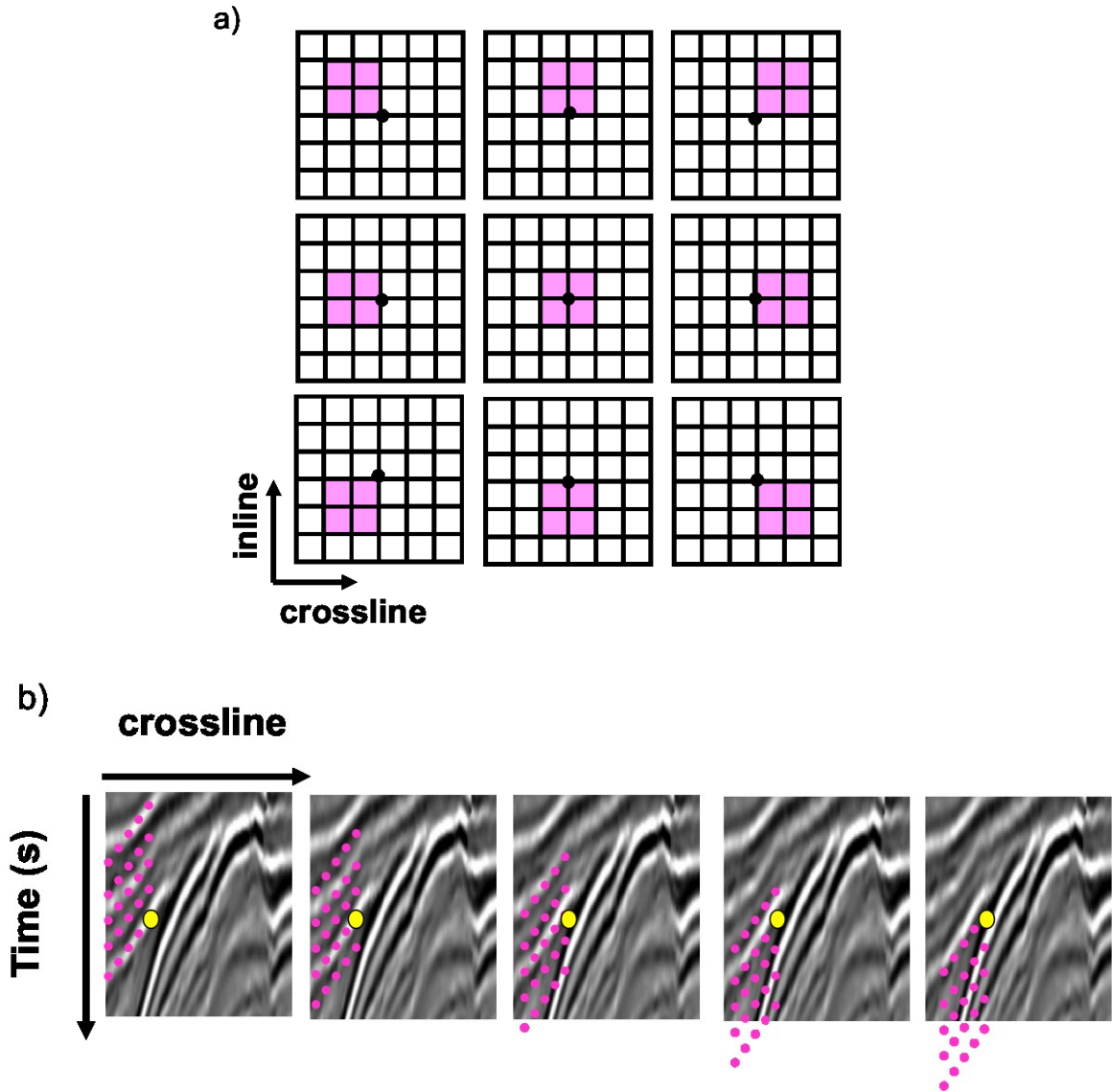


Figure A3: (a) A plan view of a nine-trace, nine-lateral-window search for dip and azimuth. Solid circles indicate the analysis point, and shaded rectangles indicate alternative analysis windows. We begin by calculating and then interpolating for the coherence and dip and azimuth within each window as described in Figure 6. This process is repeated for all $9 \times 5 = 45$ overlapping analysis windows, each containing the desired analysis point. The dip and azimuth at the analysis point are defined to be the dip and azimuth of the window that encompasses the analysis point having the maximum coherence. Use of such temporally and laterally shifted analysis windows helps preserve angular unconformities and other features of geologic interest. (b) A vertical view of the first (northwest) window shown in Figure 3.9a illustrating the search over five vertical windows containing the analysis point indicated by the yellow dot (only the three crossline traces are displayed). After Marfurt (2006).